

OPTIMIZATION AND TENSOR NETWORK METHODS
FOR QUANTUM OPTICS AND QUANTUM CIRCUIT ANALYSIS

A DISSERTATION
SUBMITTED TO THE DEPARTMENT OF ELECTRICAL
ENGINEERING
AND THE COMMITTEE ON GRADUATE STUDIES
OF STANFORD UNIVERSITY
IN PARTIAL FULFILLMENT OF THE REQUIREMENTS
FOR THE DEGREE OF
DOCTOR OF PHILOSOPHY

Sattwik Deb Mishra

June 2024

© 2024 by Sattwik Deb Mishra. All Rights Reserved.

Re-distributed by Stanford University under license with the author.



This work is licensed under a Creative Commons Attribution-Noncommercial 3.0 United States License.

<http://creativecommons.org/licenses/by-nc/3.0/us/>

This dissertation is online at: <https://purl.stanford.edu/wd089pk0418>

I certify that I have read this dissertation and that, in my opinion, it is fully adequate in scope and quality as a dissertation for the degree of Doctor of Philosophy.

Jelena Vuckovic, Primary Adviser

I certify that I have read this dissertation and that, in my opinion, it is fully adequate in scope and quality as a dissertation for the degree of Doctor of Philosophy.

David Miller

I certify that I have read this dissertation and that, in my opinion, it is fully adequate in scope and quality as a dissertation for the degree of Doctor of Philosophy.

Amir Safavi-Naeini

Approved for the Stanford University Committee on Graduate Studies.

Stacey F. Bent, Vice Provost for Graduate Education

This signature page was generated electronically upon submission of this dissertation in electronic format.

Abstract

In recent years, there has been rapid progress in the development of highly controllable quantum systems, opening up applications in quantum computing and quantum communication. With the ultimate goal of creating a fault-tolerant quantum computing platform, noisy intermediate scale quantum devices have been shown to be able to carry out non-trivial computational tasks. Thus, it has become important to understand and alleviate the issues affecting the operation of current noisy quantum computers and communication between them, and to develop numerical simulation tools to aid this understanding.

In this thesis, I will describe theoretical and computational approaches, based on tools from numerical optimization theory and tensor network simulation methods, to tackle some of these issues. First, I will present a numerical optimization strategy to improve the efficiency of quantum transducers, that are crucial for quantum communication over optical fiber links. Second, I will describe an optimization-based numerical method utilizing tensor network simulations, for efficiently computing performance bounds on noisy quantum circuits to answer if they can outperform classical computers. Finally, I will present a theoretical proposal for a Hamiltonian to model an arbitrary linear optical device, and use it to implement tensor network simulations of a time-delayed feedback system. Such feedback systems could possibly provide a platform for generation of highly entangled states for quantum computation.

Acknowledgements

First and foremost, I would like to thank my advisor Prof. Jelena Vučković for giving me the opportunity to be her student, to do research in her amazing group, and for her incessant support throughout. Even in her busy schedule, she makes sure to meet with all of her students every week, and is always available for individual meetings. She also gives her students great freedom in their research pursuits, and is very optimistic and excited about new science, something that I deeply appreciate. Besides academic advising, Jelena has also been incredibly supportive during the myriad struggles, mental and emotional, during my PhD. She always has her students' best interests at heart and I will always be indebted and grateful to her.

I would like to thank Prof. Amir Safavi-Naeini and Prof. David Miller for being on my qualification and reading committees. Being the teaching assistant for Prof. Miller's course was my first experience of teaching, and it was greatly formative and enjoyable. I deeply appreciate all of our conversations about quantum mechanics during the duration of the course. Collaborating with Prof. Safavi-Naeini on the quantum transduction project and answering his insightful questions was an incredible learning experience.

I would also like to thank Prof. Jonathan Fan, Prof. Vedika Khemani, and Prof. Joonhee Choi for being part of my defense committee. Though I did not have the chance to work with Prof. Fan during my PhD, I learnt a lot from answering his perceptive questions during my defense. Prof. Khemani's condensed matter physics course was very helpful to me in my research. I am very grateful to Prof. Choi for giving me the opportunity to T.A. his course — it was very fun to work with him throughout, and I deeply appreciate all of our conversations about science and life and all of his help.

I would like to thank Prof. Rahul Trivedi, mentor extraordinaire. Almost everyone that knows Rahul says he's one of the smartest people they know, and it's true! At the same time, Rahul is a caring mentor and friend who has been incredibly supportive throughout my PhD. I've learnt how to approach theory problems through working with him on most of my research projects. He has been a constant presence through all the trials and tribulations, research and otherwise, of my PhD career and his advice and help has been invaluable. Thanks for always being there, and being in my corner — I will always be grateful.

During my PhD, I had the opportunity to collaborate with the incredible researchers at the Max-Planck-Institute for Quantum Optics. I want to thank Prof. Ignacio Cirac for giving me the opportunity to collaborate with the group. I am deeply grateful to Dr. Mari Carmen Bañuls, Dr. Asli Çakan, and Miguel Frias for their collaboration. They are amazing scientists and deeply considerate people from whom I have learnt a lot, and collaborating with them was a highlight of my research career.

When I started my PhD journey, I started off as an experimentalist before making a switch to theory down the line. During the initial stages of my PhD, I worked with many amazing researchers — I would like to thank Dr. Constantin Dory, Dr. Alison Rugar, Prof. Shuo Sun, Dr. Shahriar Aghaeimeibodi, Dr. Linda Zhang, Dr. Daniil Lukin, and Dr. Melissa Guidry for their collaboration. My special thanks to Alison and Constantin for being great friends — I will always cherish all our time spent hanging out together (fishing trips!). I also want to thank our awesome post-docs Prof. Chris Anderson, Dr. Giovanni Scuri and Dr. Eric Rosenthal for their help through the post-PhD job search process.

My journey would not have been possible without my dear friends. I want to thank Dr. Alex White, Katherine Guo, and Geun Ho Ahn for being great fun to hang out with, for persistently sticking with me, and for being there for me in the moments I needed it most, even when I am hard to reach. All the food we got together, the games and sports, and even just hanging out at Coupa are core memories for me. I feel incredibly lucky to have them as friends and look forward to spending more time with them in the future.

I would like to thank some other group members and friends who left an indelible

impression on me. Thank you to Dr. Logan Su for all the fun dinners, for being such a calm and helpful existence, for playing the piano together with me, and for the awesome poems he writes for everyone. Thank you to Dr. Jinhie Skarda for playing badminton with me, for letting me hang out with Atticus and for being a great friend in general. Thank you also to the younger group members Hope Lee and Yakub Grzesik for being very fun to hang out and chat with!

I also want to thank my roommate from undergrad, Dr. Arka Sadhu, for being a steadfast friend and always checking up on me. Visiting him in LA and going to AX together is another core memory for me, and I deeply appreciate all of our conversations and his friendship. Thanks to Dr. Pulkit Tandon and Dr. Sneha Goenka also for being there for me all the time, and for all their support, both practical and emotional, during the job-search process. Thanks also to Yashvi Singh, Dr. Shivam Garg, Dr. Sumith Kulal, Praveen Sriram, Ayan Mandal and Sakshi Namdeo for being my friends!

For better or for worse, the PhD journey is oft challenging and demands a lot emotionally, and it was the case for me. My deepest thanks to Stanford CAPS, and specifically Hae-Ok Miller. Hae-Ok's excellent, empathetic, considerate and friendly counselling helped me beyond words towards the end of the PhD. Thank you so much!

List of publications

S. D. Mishra, R. Trivedi, A. H. Safavi-Naeini, and J. Vučković, Control Design for Inhomogeneous-Broadening Compensation in Single-Photon Transducers, *Phys. Rev. Applied* 16, 044025 (2021).

S. D. Mishra, M. Frías-Pérez, and R. Trivedi, Classically Computing Performance Bounds on Depolarized Quantum Circuits, *PRX Quantum* 5, 020317 (2024).

R. Trivedi, K. Fischer, **S. D. Mishra**, and J. Vučković, Point-Coupling Hamiltonian for Frequency-Independent Linear Optical Devices, *Phys. Rev. A* 100, 043827 (2019).

D. M. Lukin, M. A. Guidry, J. Yang, M. Ghezellou, **S. D. Mishra**, H. Abe, T. Ohshima, J. Ul-Hassan, and J. Vučković, Two-Emitter Multimode Cavity Quantum Electrodynamics in Thin-Film Silicon Carbide Photonics, *Phys. Rev. X* 13, 011005 (2023).

D. M. Lukin, C. Dory, M. A. Guidry, K. Y. Yang, S. D. Mishra, R. Trivedi, M. Radulaski, S. Sun, D. Vercauteren, G. A. Ahn, J. Vučković, 4H-Silicon-Carbide-on-Insulator for Integrated Quantum and Nonlinear Photonics, *Nat. Photonics* 14, 330 (2020).

A. E. Rugar, C. Dory, S. Aghaeimeibodi, H. Lu, S. Sun, **S. D. Mishra**, Z.-X. Shen, N. A. Melosh, and J. Vučković, Narrow-Linewidth Tin-Vacancy Centers in a Diamond Waveguide, *ACS Photonics* 7, 2356 (2020).

Contents

Abstract	iv
Acknowledgements	v
List of publications	viii
1 Introduction	1
2 Control design for single-photon quantum transducers	4
2.1 Model	6
2.1.1 Input-output equations	7
2.1.2 Control design as an optimization problem	10
2.2 Gradient-based optimization of drives	11
2.2.1 Adjoint variable method	11
2.2.2 Results	15
2.3 Optimality of drive design	21
2.3.1 Lagrangian duals	23
2.3.2 Results	26
2.4 Conclusion	27
3 Classically computing performance bounds on noisy quantum circuits	28
3.1 Notation	29
3.2 Duality based bounds	30

3.2.1	Single-qubit example	30
3.2.2	General formulation	33
3.3	Trace purity-based lower bound	39
3.3.1	Formulation	39
3.3.2	Numerical studies	44
3.4	Using duality with information content	49
3.5	Conclusion	53
4	Point-coupling Hamiltonian for frequency-independent linear optical devices	54
4.1	Point-coupling Hamiltonian	55
4.1.1	Dynamics in the Heisenberg picture	55
4.1.2	Quantum scattering matrix of the point-coupling Hamiltonian	61
4.1.3	Normal modes of the point-coupling Hamiltonian	64
4.2	Matrix-product-state based simulations of time-delayed feedback systems	66
4.3	Conclusion	72
5	Conclusions and outlook	74
A	Maximising transduction efficiency through a homogeneous ensemble	76
B	Hybridization of eigenstates of a homogeneous ensemble with the introduction of inhomogeneity	78
C	Free fermion formulation	80
C.0.1	Model	80
C.0.2	Calculation of the noisy circuit output	81
C.0.3	Calculation of the dual function	82
D	Existence of quantum circuit and Hamiltonian where dual bound scales super-exponentially with circuit depth	86

E Solving Heisenberg equations of motion for point coupling Hamiltonian	89
F Calculating normal modes of the point coupling Hamiltonian	91
G Convergence of matrix-product-state simulations	93
Bibliography	96

List of Figures

2.1	(a) Schematic of a three-level system ensemble-based transducer device. (b) Scaling of transduction efficiency with increasing number (N) of three-level systems in a homogeneous ensemble for different cooperativities C (we keep γ fixed and vary Γ to vary cooperativity). (c) Decrease in the transduction efficiency through randomly inhomogeneously broadened ensembles of $N = 10$ emitters with increasing inhomogeneous broadening Δ for different cooperativities C . For each value of the inhomogeneous broadening Δ , 100 randomly broadened ensembles are created by sampling the emitter detunings $\delta_\mu^{(i)}, \delta_{\text{opt}}^{(i)}$ from a Gaussian distribution with standard deviation equal to Δ . Each plot point corresponds to the mean over the 100 ensembles with inhomogeneous broadening equal to the corresponding value of Δ and the shaded regions represent the standard deviation. (d) Transduction spectra of ensembles ($N = 10, C = 0.1$) with varying inhomogeneous broadening Δ	6
2.2	(a) Fourier transform of the input microwave field (Gaussian waveform). Dashed lines are representative of the individual emitter frequencies in a random ensemble ($N = 10, \Delta = 200\gamma$). (b) Amplitudes of the harmonic components of the optimized $\Omega(t)$ designed for the same ensemble. (c) Comparison of the transduction spectrum of the same ensemble with and without optimized drives applied — the transduction spectrum with the optimized drive is computed using a Floquet scattering theory approach.	15

2.3 Optimized drives countering inhomogeneous broadening. (a) Transduction efficiency and (b) improvement in the transduction efficiency through randomly inhomogeneously broadened ensembles of $N = 10$ emitters with increasing inhomogeneous broadening for different cooperativities C when the optimized drives are applied. For each Δ , optimized drives are designed for each of the same 100 randomly generated ensembles with inhomogeneous broadening equal to Δ as used in Fig. 2.1c. Before running the optimizations, for each ensemble, the input photon is frequency-shifted to match the highest peak of the unoptimized transduction spectrum. Also, the initial condition for the optimization is $\Omega(t) = (N\gamma + \Gamma)/2$, which is a constant drive that maximises the transduction efficiency through a homogeneous ensemble with the same decay rates (see Appendix A). Improvement is defined as the ratio of the efficiencies with and without the optimized drive applied. Each plot point corresponds to the mean over the 100 ensembles with inhomogeneous broadening equal to the corresponding value of Δ and the shaded regions represent the standard deviation. .

16

2.4 (a) Comparison of the superradiance metric for ensembles with inhomogeneous broadening $\Delta = 200\gamma$ with and without optimized drives applied (data for optimized and unoptimized cases are dodged in the plot for visual clarity). After generating the optimized drives used in Fig. 2.3, we compute the metric for all eigenstates of each of the 100 random ensembles with inhomogeneous broadening $\Delta = 200\gamma$ by numerically diagonalising the propagator over one time period of the effective Hamiltonian. Each plot point and associated error bars correspond to the mean and standard deviation (over the collection of ensembles with $\Delta = 200\gamma$) of the maximum value of the superradiance measure $f[|\phi\rangle]$ over all Floquet eigenstates $|\phi\rangle$. The dashed line denotes the same for a homogeneous ensemble. As we increase Γ to decrease the cooperativity, the metric is larger on average in the unoptimized case. We attribute this to the simultaneous increase in the unoptimized drive $\Omega(t) = (N\gamma + \Gamma)/2$ overshadowing the constant inhomogeneous broadening $\Delta = 200\gamma$ (see Appendix B). (b, c, d) Density plots (obtained by kernel density estimation using Gaussian kernels) of the superradiance measure for eigenstates of the 100 ensembles with inhomogeneous broadening $\Delta = 200\gamma$, (b) $C = 0.01$, (c) $C = 0.1$, (d) $C = 1$

17

2.5 Transduction efficiency improvement with uncustomized optimization. (a) Amplitudes of the frequency components comprising the uncustomized drive. (b) Density plots of the transduction efficiency through 100 ensembles (test set) with $\Delta = 200\gamma$, $C = 0.1$ for three cases – (green) no optimised drive is applied and the input photon is fixed at the resonance of a homogeneous ensemble, (orange) no optimised drive is applied but the input photon is frequency-shifted to match the highest peak of the unoptimized transduction spectrum for each inhomogeneous ensemble, and (blue) the uncustomized optimized drive is applied and the input photon is fixed at the resonance of a homogeneous ensemble.

19

2.6	Temporal mode overlap-based design of drives. The amplitude $ a_{\text{opt}}(t) ^2$ of the output photon's temporal wave-packet after transduction by an ensemble of $N = 3$ emitters, with $C = 0.1$, $\Delta \approx 61.61\gamma$, and under the application of drives obtained by locally solving problem (2.45) for (a) $c_0 \approx 1.331, c_1 = 0$ (b) $c_0 \approx 1.331, c_1 \approx 247.02$. The improvement in transduction efficiencies are (a) $4.466\times$ and (b) $3.977\times$, respectively.	20
2.7	Heuristic and certifiable upper bounds and unoptimized and optimized transduction efficiencies calculated for ensembles with $N = 3$ emitters and cooperativities (a) $C = 0.01$, (b) $C = 0.1$, (c) $C = 1$. For each Δ , 100 random ensembles are generated with inhomogeneous broadening equal to Δ . For each such ensemble, optimized drives are designed to improve transduction efficiency by using a local optimizer to solve problem (2.16). Then, using the state obtained by solving the input-output equation with the aforementioned optimized drive as the reference state, heuristic and certifiable bounds are calculated. Each plot point corresponds to the mean over the 100 ensembles with inhomogeneous broadening equal to the corresponding value of Δ and the shaded regions represent the standard deviation.	26
3.1	Comparison of bounds, with and without accounting for circuit constraints, on the minimum energy corresponding to the Hamiltonian $H = \Delta Z$ attainable by the output of the single qubit circuit shown in the schematic. The circuit consists of a Y-axis rotation followed by depolarizing noise acting with probability p	31
3.2	Schematic depiction of the problem setting. The unitaries (colored boxes) implement a quantum algorithm to prepare an approximation of the ground state of a target Hamiltonian H in the absence of noise. Each layer of unitary is followed by single-qubit depolarizing noise (gray circles) on the qubits applied with a probability p	33

3.3 (a) Schematic of benchmark circuits considered for 1D spin systems: colored boxes indicate unitaries and grey circles depolarizing noise. Two-qubit unitaries are chosen to be $\exp(-i\theta X \otimes X)$ and single-qubit unitaries are independently Haar random. The Hamiltonian is chosen to be $H = -U_H(\sum_i Z_i)U_H^\dagger$, where U_H is the first layer of unitaries, making H a 4-local commuting Hamiltonian. The first layer of unitaries U_H thus transforms the initial state $|0\rangle^{\otimes N}$ into the ground state of H . The last $(d-1)/2$ layers are chosen to be the inverse of the previous $(d-1)/2$ layers — in the absence of noise, the output of the circuit is the ground state of H . (b) Plot shows trace purity-based dual bound ($h(\vec{\sigma}^{h,D})$ in Eq. 3.8) (solid lines, circular markers) and bound obtained by only considering the TEBD errors ($E_{\text{TEBD}} - \delta$ in Eq. 3.11) (dotted lines, diamond markers) for the ground state (G. S.) energy of the target Hamiltonian, as a function of circuit depth d for a system of $N = 40$ spins, with two-qubit gate parameter $\theta = 0.05$, depolarizing noise rate of $p = 3\%$ and varying MPO ansatz bond dimensions D . Grey dashed line indicates G.S. energy, grey shaded area indicates region of trivial bounds (less than G.S. energy), blue dashed line indicates energy of the completely mixed state $\mathbb{1}/2^N$. The y -axis is scaled by a constant multiplicative factor in the trivial region for visual clarity. The Hamiltonian is shifted and scaled such that its spectrum is in $[0, 1]$. 43

- 3.4 Comparison of the trace purity-based dual bound ($h(\vec{\sigma}^{h,D})$ in Eq. 3.8) and the bound based on just the information content of the output state ($\ell_{\lambda_c}^I$ in Eq. 3.13) for 1D many-body spin systems. Both bounds are lower bounds on the ground state (G. S.) energy of the same target Hamiltonian as considered for the results in Fig. 3.3. Plots show the bounds as a function of brick-wall quantum circuit depth d [Fig. 3.3(a)] for a system of $N = 40$ spins, varying MPO ansatz bond dimensions D , with depolarizing noise rates of (a) $p = 3\%$, (b) $p = 5\%$, (c) $p = 10\%$, and (d) $p = 20\%$. Two-qubit unitaries in the brick-wall circuit are chosen to be $\exp(-i\theta X \otimes X)$ with $\theta = 0.1$ and single-qubit unitaries are independently Haar random. Grey dashed line indicates G.S. energy, grey shaded area indicates region of trivial bounds (less than G.S. energy), blue dashed line indicates energy of the completely mixed state $\mathbb{1}/2^N$. The y -axis is scaled by a constant multiplicative factor in the trivial region for visual clarity. The Hamiltonian is shifted and scaled such that its spectrum is in $[0, 1]$ 45
- 3.5 Trace purity-based dual bounds ($h(\vec{\sigma}^{h,D})$ in Eq. 3.8) for a 1D system of $N = 32$ spins, the same target Hamiltonian as considered for the results in Fig. 3.3 (see description of Hamiltonian in caption of Fig. 3.3), and brick-wall quantum circuits [Fig. 3.3(a)] where two-qubit unitaries are chosen to be $\exp(-i\theta X \otimes X)$ and single-qubit unitaries are independently Haar random. Plots show dual bounds as a function of noise rate p and circuit parameter θ for circuit depth $d = 25$ and bond dimensions (a) $D = 32$ and (b) $D = 64$. The Hamiltonian is shifted and scaled such that its spectrum is in $[0, 1]$ 46

3.6	<p>(a) Schematic of quantum circuits considered for 2D spin systems on a square lattice: colored boxes indicate unitaries and grey circles depolarizing noise. Each unitary layer consists of two-qubit unitaries $\exp(-i\theta X \otimes X)$ (blue boxes) followed by independently Haar random single-qubit unitaries (green boxes). The first $d/2$ layers serve to increase the entanglement in the state. The remaining layers invert the action of the previous $d/2$ such that, in the absence of noise, the output of the circuit is the ground state of $H = -\sum_{\langle i,j \rangle} Z_i Z_j$ where Z_i is the Pauli-Z operator for the i^{th} spin and $\langle i,j \rangle$ indicates nearest-neighbors.</p> <p>(b) Circuits considered have a brick-wall structure: two-qubit unitary layers cycle between gates on odd horizontal edges (U_1), even horizontal edges (U_2), odd vertical edges (U_3), and even vertical edges (U_4). Single-qubit gates (U_s) are applied on every qubit after every two-qubit gate layer.</p> <p>(c) Structure of the MPO considered for 2D spin systems: yellow squares indicate tensors at each site in the 2D lattice and lines emerging from them indicate tensor indices. Horizontal lines indicate bond indices with dimension D and diagonal lines indicate physical indices.</p>	47
3.7	<p>Trace purity-based dual bounds ($h(\vec{\sigma}^{h,D})$ in Eq. 3.8) for the ground state energy of the target Hamiltonian H as a function of noise rate p and circuit parameter θ for a system of $N = 36$ spins arranged in a 6×6 lattice, circuit depth $d = 32$ and MPO bond dimensions (a) $D = 64$ and (b) $D = 362$. The Hamiltonian is shifted and scaled such that its spectrum is in $[0, 1]$.</p>	48
3.8	<p>Schematic of SSH model quadratic fermionic Hamiltonians with alternating hopping strengths in 1D and 2D.</p>	51

3.9	Comparison of information content-based dual bounds with and without circuit constraints, and the output energies of noisy Gaussian circuits for systems consisting of (a) $N = 48$ fermions arranged in a 1D lattice, (b) $N = 49$ fermions arranged in a 7×7 2D lattice. Dual bounds are shown for ansatzes with varying interaction range r . The horizontal axis represents the depth d of a Gaussian brick-wall circuit that outputs the ground state of the SSH model. Fermions are independently subject to depolarizing noise with probability $p = 5\%$ after every unitary layer. The Hamiltonians are shifted and scaled such that their spectrum is in $[0, 1]$	52
4.1	Schematic of a linear optical device acting on N optical modes. The frequency-domain and position-domain annihilation operator for the n^{th} optical mode are denoted by $a_n(\omega)$ and $a_n(x_n)$ respectively where x_n is the position of the point under consideration in the coordinate system attached to the n^{th} optical mode (note that we each optical mode to, in general, have its own independent coordinate system with the linear optical device being at $x_n = x_n^0$ in the coordinate system of the n^{th} optical mode.).	56
4.2	Schematic figures showing the action of (a) phase-shifter with imparted phase φ acting on a optical mode denoted by a , (b) beam-splitter with parameters (θ, φ) acting on optical modes denoted by a_1 and a_2 and (c) an optical circulator designed acting on optical modes a_1 , a_2 and a_3 . The relationship between the input and output signals of the linear-optical device are also shown in the diagrams.	59

4.3	Schematic figure of the time-delayed feedback system. A two-level system with de-excitation operator σ couples to a waveguide which supports both forward propagating and backward propagating waveguide modes with frequency-domain (position-domain) annihilation operators $a_+(\omega)$ and $a_-(\omega)$ ($a_+(x_+)$ and $a_-(x_-)$) respectively. A mirror, modelled as a beam-splitter on the forward and backward propagating waveguide mode with parameters (θ, φ) , is located as $x_{\pm} = 0$ and the two-level system couples to both the waveguide modes at a distance t_d from the mirror. The decay rates of the two-level system into the forward and backward propagating waveguide modes are denoted by γ_+ and γ_- respectively. Finally, we also consider the dynamics of this system when the two-level system is driven by an external laser pulse — $\Omega(t)$ denotes the complex amplitude of the laser pulse that drives the two-level system.	66
4.4	Validation of our MPS update implementation for an ideal mirror (i.e. $\theta = \pi/2$) for two simulation settings: (a) Simulation of an un-driven two-level system ($\Omega(t) = 0$) which is initially in its excited state for different mirror phases φ and (b) simulation of a two-level system initially in its ground state and driven by an exponentially decaying pulse ($\Omega(t) = \Omega_0 e^{-\alpha t}$ for $t > 0$) for different mirror phases φ . $ \varepsilon(t) $ is the probability amplitude of the two-level system being in the excited state computed using $ \varepsilon(t) ^2 = \langle \sigma^\dagger \sigma \rangle$. It is assumed that $\gamma_+ = \gamma_- = \gamma/2$, $\delta_e = \omega_e - \omega_0 = 0$, $\omega_0 t_d = \pi$, $\gamma t_d = 2$ and $\alpha = 2\gamma$. For the discretization into an MPS, we use $\gamma \Delta t = 0.05$, and truncate the dimensionality of the Hilbert space of each waveguide bin to 2 for both forward and backward propagating modes. A threshold of 0.01 is used in all the Schmidt decompositions performed while applying the swap gates and the short-range gates. Refer to appendix G for convergence studies of the MPS simulations.	71

4.5 Impact of mirror reflectivity on the dynamics of the time-delayed feedback system for two simulation settings: (a) Simulation of an undriven two-level system ($\Omega(t) = 0$) which is initially in its excited state for different mirror reflectivities $\cos\theta$ and (b) simulation of a two-level system initially in its ground state and driven by an exponentially decaying pulse ($\Omega(t) = \Omega_0 e^{-\alpha t}$ for $t > 0$) for different mirror reflectivities $\cos\theta$. $|\varepsilon(t)|$ is the probability amplitude of the two-level system being in the excited state computed using $|\varepsilon(t)|^2 = \langle \sigma^\dagger \sigma \rangle$. It is assumed that $\gamma_+ = \gamma_- = \gamma/2$, $\delta_e = \omega_e - \omega_0 = 0$, $\omega_0 t_d = \pi$, $\gamma t_d = 2$, $\varphi = 0$ and $\alpha = 2\gamma$. For the discretization into an MPS, we use $\gamma\Delta t = 0.05$, and truncate the dimensionality of the Hilbert space of each waveguide bin to 2 for both forward and backward propagating modes. A threshold of 0.01 is used in all the Schmidt decompositions performed while applying the swap gates and the short-range gates. Refer to appendix G for convergence studies of the MPS simulations.

72

G.1 Convergence studies on the MPS simulations for the time-delayed feedback system introduced in section 4.2. The undriven two-level system ($\Omega(t) = 0$) is initially in its excited state and is allowed to decay into the forward and backward propagating waveguide modes with an ideal mirror ($\theta = \pi/2, \varphi = 0$) providing feedback. $|\varepsilon(t)|$ simulated using MPS update for (a) different discretization time-steps Δt and (b) different tolerances that govern the number of Schmidt vectors retained after every Schmidt decomposition on the MPS. The dotted black line shows $|\varepsilon(t)|$ obtained on solving the ODE (Eq. G.1) with a very small time-step ($\gamma\Delta t = 0.001$). $|\varepsilon(t)|$ is the probability amplitude of the two-level system being in the excited state computed using $|\varepsilon(t)|^2 = \langle \sigma^\dagger \sigma \rangle$. In the simulations shown in (a) the Schmidt tolerance is assumed to be 0.01 and in the simulations shown in (b) $\gamma\Delta t = 0.05$. It is also assumed that $\gamma_+ = \gamma_- = \gamma/2$, $\delta_e = \omega_e - \omega_0 = 0$, $\omega_0 t_d = \pi$ and $\gamma t_d = 2$.

94

Chapter 1

Introduction

Since the inception in the 1980s of the idea of using systems described by the laws of quantum mechanics for solving computational problems [1, 2, 3], the field of quantum computing has grown extensively. With the ideal of a fault-tolerant quantum computer [4, 5] that is resilient to noise as the goal, there has been rapid progress in various quantum computing experimental platforms like trapped ions [6], neutral atoms [7], and superconducting quantum systems [8]. With each step of this progress, the number of controllable qubits available per computer has increased or the noise rates affecting the computations have decreased. Furthermore, a network of connected quantum processors [9] can be used to realize scalable, distributed quantum computing [10]. To aid the effort towards realizing both individual error-corrected quantum computers and their connection in a quantum internet, it is important to solve simulation, design, and analysis problems arising at various levels. In this thesis, I describe theoretical and computational solutions relying on techniques from numerical optimization theory and tensor network methods to tackle certain engineering and analysis problems relevant to the development of quantum computers.

First, I consider the problem of the development of a quantum internet by the connection of distant superconducting quantum computers, each of which operate at microwave frequencies. Optical fibers can be used as the quantum channels for such a network if transducers of single photons from microwave to optical frequencies are

available. Ensembles of solid-state emitters (like color centers in diamond and silicon carbide and rare-earth ions doped in crystals) are an attractive platform for implementing such transducers due to scalable nano-fabrication [11, 12] and their integrability with superconducting quantum systems [13, 14]. Collective coupling of an ensemble of identical quantum emitters to microwave and optical fields can result in a superradiant enhancement [15, 16] of coupling strengths and better transduction efficiencies. However, inhomogeneous broadening in the transition frequencies [17, 18] of emitters can hamper the formation of a collective superradiant state and lower transduction efficiencies. I present a strategy relying on the laser driving of an emitter ensemble-based transducer as a quantum control [19] for single photon scattering [20]. We employ a gradient-based optimization algorithm to design the temporal shape of the laser drive to mitigate the effects of inhomogeneous broadening and demonstrate up to an order of magnitude improvement in transduction efficiencies.

Second, considering that quantum computers can potentially outperform classical computers in certain computational tasks, I present an approach to answer if this advantage can persist in the presence of noise without error correction. Finding ground states of classical and quantum Hamiltonians is a paradigmatic problem in both computer science and many-body physics [21, 22]. There has been great interest [23, 24, 25] in understanding whether quantum computers can be used to solve these problems. While a fault tolerant quantum computer could provide an advantage in these problems in certain scenarios, building one remains a technological hurdle. Consequently, there has been great interest in understanding if noisy intermediate-scale quantum devices can be used to implement quantum circuits to approximate ground states [26, 27, 28, 29] and in what circumstances they definitely fail to provide any benefit over classical algorithms.

To address this problem, I describe in this thesis the development of an impossibility result for quantum advantage - we accomplish this by developing a numerical method to classically compute certifiable performance bounds on noisy quantum circuits which can then be compared to certifiable classical algorithms [30, 31, 32] to outline noise regimes where there is no quantum advantage. Our formulation is based on tracking

the noise-induced entropy accumulation through the quantum circuit, together with using the principle of Lagrangian duality to account for the circuit architecture. While rigorous bounds on noisy quantum circuits have been previously provided [33, 34, 35], our formulation is the first work to provide lower bounds that capture the propagation of errors in a quantum circuit. We provide both numerical evidence in 1D and 2D circuits of 50 qubits, as well as analytical results showing that our bounds predict a super-exponentially worse degradation of the performance of the circuit with circuit depth compared to previously studied bounds.

Finally, I present the development of a Hamiltonian model for linear optical devices [36, 37, 38] acting on propagating optical modes and describe the utility of such a model for simulating quantum optical systems with feedback [39, 40], as such systems can potentially be useful for generating entanglement for quantum computing or realizing quantum memories. We show how to construct the Hamiltonian corresponding to a general frequency-independent linear optical device described by a classical scattering matrix, and provide examples of Hamiltonians for some commonly used devices. We then use the Hamiltonian to rigorously formulate a matrix-product-state (tensor network) [41, 42] based simulation for time-delayed feedback systems wherein the feedback is provided by a linear optical device described by a scattering matrix as opposed to a hard boundary condition (e.g. a mirror with less than unity reflectivity).

Chapter 2

Control design for single-photon quantum transducers

Presently, superconducting quantum systems are able to achieve non-trivial quantum computational tasks, and are a promising candidate for forming the nodes of a quantum internet to realize scalable, distributed quantum computing. But direct connection of distant superconducting quantum systems proves difficult as they operate at microwave frequencies, and commercial microwave cables are dominated by thermal noise at room temperature and hence face huge loss over long distances. On the other hand, cryo-cooled superconducting transmission lines are low loss but limited to short distances [43]. Optical photons can serve as better ‘flying’ qubits as they can be transmitted with low loss over long distances through optical fibers. To connect superconducting quantum systems, there is thus a necessity to realize coherent transduction systems that can convert photons coherently and bi-directionally between microwave and optical frequencies.

Many approaches have been proposed to construct such transducers [44, 45]. Microwave-to-optical transducers couple fields oscillating at the respective frequencies through a non-linear medium that can be driven externally to bridge the gap between these frequency regimes. The different types of non-linear media that have been studied so far are, electro-optic materials [46, 47, 48, 49, 50, 51], magnon modes [52, 53, 54], optomechanical systems [55, 56, 57, 58, 59, 60, 61, 62, 63, 64, 65, 66, 67, 68, 69], and broadly,

ensembles of atomic systems [70, 71, 72, 73, 74, 75, 76, 77, 78, 79, 80, 81, 82, 83, 84, 85]. Solid-state emitters (like color centers in diamond and silicon carbide and rare-earth ions doped in crystals) can have transitions coupling to both microwave and optical fields. They provide an attractive platform for implementing quantum transducers owing to the possibility of integration with superconducting quantum systems [13, 14] and scalability afforded by rapidly developing nano-fabrication techniques [11, 12, 86]. However, single defects are often only weakly coupled to the microwave and optical fields, leading to low transduction efficiencies. An approach to overcoming this limitation is to use ensembles of such emitters coupling to the same microwave and optical channels — the coupling strength is then enhanced proportionally to the number of emitters as a consequence of the formation of a collective superradiant state of the emitters [87, 88, 15, 38, 16, 89].

In practical devices, emitters do not have identical resonant frequencies [17, 18, 90] — this inhomogeneous broadening in the resonant frequencies prohibits the formation of a collective superradiant state and lowers the transduction efficiencies. However, the temporal shape of the lasers driving the emitter ensembles can be experimentally tuned — this opens up the possibility of using quantum control techniques to compensate for inhomogeneous broadening in the emitter ensemble, restore superradiance, and improve transduction efficiencies.

Our approach to solving this design problem is to use a time-dependent scattering theory framework [20] to pose the problem of inhomogeneity compensation as a control problem — this framework not only allows us to account for the collective interaction between the emitters as mediated by the optical and microwave fields, but also account for properties of the emitted and absorbed photons in the resulting quantum control problem. For the emitter based transduction system, we solve the resulting control problem using a gradient-based optimization algorithm to demonstrate an order of magnitude improvement in the transduction efficiencies. Furthermore, to assess the optimality of the resulting solution, we calculate provable upper bounds on the transduction efficiencies achievable by designing the temporal shape of the laser drive. Our work is closely related to, but distinct from Ref. [91] wherein a similar framework was used to design quantum controls for mediating interactions between

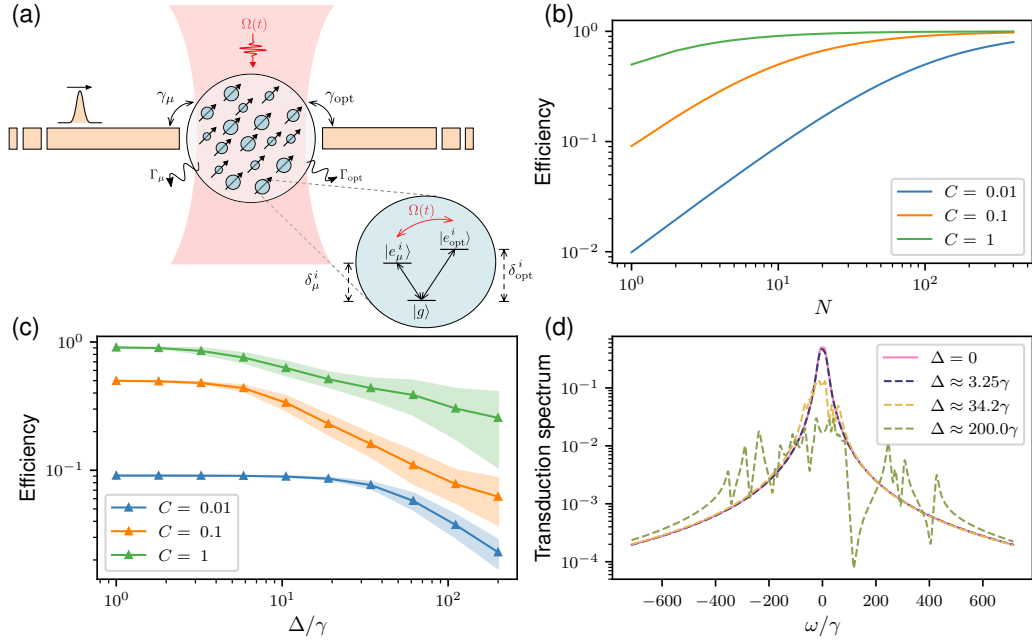


Figure 2.1: (a) Schematic of a three-level system ensemble-based transducer device. (b) Scaling of transduction efficiency with increasing number (N) of three-level systems in a homogeneous ensemble for different cooperativities C (we keep γ fixed and vary Γ to vary cooperativity). (c) Decrease in the transduction efficiency through randomly inhomogeneously broadened ensembles of $N = 10$ emitters with increasing inhomogeneous broadening Δ for different cooperativities C . For each value of the inhomogeneous broadening Δ , 100 randomly broadened ensembles are created by sampling the emitter detunings $\delta_\mu^{(i)}, \delta_{\text{opt}}^{(i)}$ from a Gaussian distribution with standard deviation equal to Δ . Each plot point corresponds to the mean over the 100 ensembles with inhomogeneous broadening equal to the corresponding value of Δ and the shaded regions represent the standard deviation. (d) Transduction spectra of ensembles ($N = 10, C = 0.1$) with varying inhomogeneous broadening Δ .

ensembles of emitters with controllable transition frequencies to implement quantum memories.

2.1 Model

The transducer model being considered is schematically depicted in Fig. 2.1a. The emitter ensemble, with each emitter considered to be a three-level system, is coupled

to microwave and optical modes with coupling operators L_μ and L_{opt} respectively, where

$$L_\mu = \sum_{i=1}^N \sqrt{\gamma_\mu} \sigma_\mu^i \text{ and } L_{\text{opt}} = \sum_{i=1}^N \sqrt{\gamma_{\text{opt}}} \sigma_{\text{opt}}^i. \quad (2.1)$$

Here, γ_μ and γ_{opt} are the decay rates of the emitters into the microwave and optical modes respectively, N is the number of emitters in the ensemble, and σ_μ^i and σ_{opt}^i are the lowering operators for transitions of the i th emitter in the ensemble. In addition to coupling to the optical and microwave modes, each emitter can also decay into additional loss channels, modeling unwanted radiative and non-radiative losses, with decay rates Γ_μ and Γ_{opt} from the excited states $|e_\mu^i\rangle$ and $|e_{\text{opt}}^i\rangle$, respectively. Furthermore, the transition between the two excited states is driven by a laser with envelope $\Omega(t)$.

2.1.1 Input-output equations

We derive the input-output equations describing the dynamics of the quantum transduction process. The Hamiltonian describing the ensemble is,

$$H_{\text{sys}}(\Omega(t)) = \sum_i \left[\delta_\mu^i \sigma_\mu^{i\dagger} \sigma_\mu^i + \delta_{\text{opt}}^i \sigma_{\text{opt}}^{i\dagger} \sigma_{\text{opt}}^i \right] + \sum_i \Omega(t) (\sigma_\mu^{i\dagger} \sigma_{\text{opt}}^i + \text{H. c.}), \quad (2.2)$$

where the transition operators $\sigma_{\mu,\text{opt}}^i$. We point out that the laser field is actually $\Omega(t) e^{i\omega_L t}$, where ω_L is the central frequency. The Hamiltonian in Eq. 2.2 is obtained by going into a rotating frame to remove the term oscillating at ω_L from the drive. The Hamiltonian of the entire system, i.e., the microwave and optical waveguide modes together with the ensemble is,

$$H = -i \int dx \left(a_{\mu,x}^\dagger \frac{\partial}{\partial x} a_{\mu,x} + a_{\text{opt},x}^\dagger \frac{\partial}{\partial x} a_{\text{opt},x} \right) + \left(a_{\mu,x=0}^\dagger L_\mu + \text{H.c.} \right) + \left(a_{\text{opt},x=0}^\dagger L_{\text{opt}} + \text{H.c.} \right) + H_{\text{sys}}, \quad (2.3)$$

where $a_{\mu,x}$ and $a_{\text{opt},x}$ are the spatial annihilation operators for the microwave and

optical waveguide modes respectively [20]. The terms in Eq. 2.3 with the operators L_s where $s \in \{\mu, \text{opt}\}$ represent the ensemble-waveguide interaction.

We define the number operator,

$$N_e = \int dx \left(a_{\mu,x}^\dagger a_{\mu,x} + a_{\text{opt},x}^\dagger a_{\text{opt},x} \right) + \sum_{i=1}^N \left(\sigma_\mu^{i\dagger} \sigma_\mu^i + \sigma_{\text{opt}}^{i\dagger} \sigma_{\text{opt}}^i \right), \quad (2.4)$$

which commutes with the Hamiltonian H . We consider an initial state with a single photon in the microwave waveguide mode. Thus, the state of the whole system is restricted to the single-excitation subspace at all times, and we assume the following ansatz for the state at time t in the Schrödinger picture,

$$\begin{aligned} |\psi(t)\rangle = & \int dx \alpha(x, t) a_{\mu,x}^\dagger |\text{vac}\rangle \otimes |G\rangle \otimes |\text{vac}\rangle + |\text{vac}\rangle \otimes |\psi_e(t)\rangle \otimes |\text{vac}\rangle \\ & + |\text{vac}\rangle \otimes |G\rangle \otimes \int dx \beta(x, t) a_{\text{opt},x}^\dagger |\text{vac}\rangle, \end{aligned} \quad (2.5)$$

where $|\text{vac}\rangle$ is the vacuum state of a waveguide mode and $|G\rangle = \bigotimes_{i=1}^N |g\rangle$ is the ground state of the ensemble.

Given this ansatz, Schrödinger's equations for the system are,

$$i \frac{d}{dt} |\psi_e(t)\rangle = H_{\text{sys}} |\psi_e(t)\rangle + \alpha(0, t) L_\mu^\dagger |G\rangle + \beta(0, t) L_{\text{opt}}^\dagger |G\rangle \quad (2.6)$$

$$\frac{\partial}{\partial t} \alpha(x, t) = -\frac{\partial}{\partial x} \alpha(x, t) - i\delta(x) \langle G | L_\mu | \psi_e(t) \rangle \quad (2.7)$$

$$\frac{\partial}{\partial t} \beta(x, t) = -\frac{\partial}{\partial x} \beta(x, t) - i\delta(x) \langle G | L_{\text{opt}} | \psi_e(t) \rangle, \quad (2.8)$$

Solving Eq. 2.7 and Eq. 2.8 for $\alpha(0, t)$ and $\beta(0, t)$,

$$\alpha(0, t) = a_\mu(t) - \frac{i}{2} \langle G | L_\mu | \psi_e(t) \rangle \quad (2.9)$$

$$\beta(0, t) = -\frac{i}{2} \langle G | L_{\text{opt}} | \psi_e(t) \rangle, \quad (2.10)$$

where $a_\mu(t) = \lim_{t_0 \rightarrow -\infty} \alpha(t_0 - t, t_0)$ describes the time-domain wave-packet of the input photon in the microwave waveguide mode. Similarly, $a_{\text{opt}}(t) = \lim_{t_1 \rightarrow \infty} \beta(t_1 - t, t_1)$

describes the time-domain wave-packet of the output photon in the optical waveguide mode. From the solution of Eq. 2.8 we have,

$$a_{\text{opt}}(t) = -i\langle G|L_{\text{opt}}|\psi_e(t)\rangle. \quad (2.11)$$

Substituting Eq. 2.9 and Eq.2.10 into Eq. 2.6, we have,

$$i\frac{d}{dt}|\psi_e(t)\rangle = \left(H_{\text{sys}} - \frac{i}{2}L_{\mu}^{\dagger}|G\rangle\langle G|L_{\mu} - \frac{i}{2}L_{\text{opt}}^{\dagger}|G\rangle\langle G|L_{\text{opt}} \right) |\psi_e(t)\rangle + a_{\mu}(t)L_{\mu}^{\dagger}|G\rangle. \quad (2.12)$$

We point out that $L_s^{\dagger}L_s = L_s^{\dagger}(P_e + |G\rangle\langle G|)L_s = L_s^{\dagger}|G\rangle\langle G|L_s$ where $s \in \{\mu, \text{opt}\}$ and P_e is the projector onto the excited state space spanned by $\{|e_{\mu}^i\rangle, |e_{\text{opt}}^i\rangle : i \in \{1, \dots, N\}\}$. Thus, Eq. 2.12 can be rewritten as,

$$i\frac{d}{dt}|\psi_e(t)\rangle = \left(H_{\text{sys}} - \frac{i}{2}L_{\mu}^{\dagger}L_{\mu} - \frac{i}{2}L_{\text{opt}}^{\dagger}L_{\text{opt}} \right) |\psi_e(t)\rangle + a_{\mu}(t)L_{\mu}^{\dagger}|G\rangle. \quad (2.13)$$

Furthermore, the decays from the excited states of the emitters into various loss channels besides the waveguides can be captured in a similar manner by adding terms like $-\frac{i\Gamma_s^i}{2}\sigma_s^{i\dagger}\sigma_s^i|\psi_e(t)\rangle$ where $s \in \{\mu, \text{opt}\}$ to the right side of Eq. 2.13. Then we have,

$$i\frac{d}{dt}|\psi_e(t)\rangle = H_{\text{eff}}(\Omega(t))|\psi_e(t)\rangle + a_{\mu}(t)L_{\mu}^{\dagger}|G\rangle, \quad (2.14)$$

where,

$$H_{\text{eff}}(\Omega(t)) = \left(H_{\text{sys}}(\Omega(t)) - \sum_i \left(\frac{i\Gamma_{\mu}^i}{2}\sigma_{\mu}^{i\dagger}\sigma_{\mu}^i - \frac{i\Gamma_{\text{opt}}^i}{2}\sigma_{\text{opt}}^{i\dagger}\sigma_{\text{opt}}^i \right) - \frac{i}{2}L_{\mu}^{\dagger}L_{\mu} - \frac{i}{2}L_{\text{opt}}^{\dagger}L_{\text{opt}} \right). \quad (2.15)$$

Eq. 2.14 and Eq. 2.11 (upto a phase factor of i) are the input-output equations describing the dynamics of the quantum transducer.

2.1.2 Control design as an optimization problem

For emitter ensembles formed out of identical emitters, the transduction efficiency is determined by the cooperativity of the individual transitions, $C_\mu = \gamma_\mu/\Gamma_\mu$ for microwave and $C_{\text{opt}} = \gamma_{\text{opt}}/\Gamma_{\text{opt}}$ for optical, as well as the number of emitters. We assume $\gamma_\mu = \gamma_{\text{opt}} = \gamma$, $\Gamma_\mu = \Gamma_{\text{opt}} = \Gamma$, and $C_\mu = C_{\text{opt}} = C = \gamma/\Gamma$ in our simulations for simplicity of analysis. Fig. 2.1b shows the transduction efficiency of this system as a function of the number of emitters for different emitter cooperativities — due to the formation of a collective superradiant state between the different emitters, this efficiency asymptotically reaches 1 on increasing the number of emitters. Furthermore, the number of emitters needed to obtain high efficiency increases with a decrease in the cooperativity of the individual emitters. We point out that for high microwave and optical cooperativities, near unity transmissions can be obtained with a single emitter and consequently it is unnecessary to use emitter ensembles. We thus focus on low cooperativity emitters. On introducing inhomogeneous broadening into the emitter frequencies, the efficiency of the transduction system decreases (Fig. 2.1c) — for large inhomogeneous broadening, the emitters do not form a collective superradiant mode and the transduction spectrum simply comprises of the individual transduction spectra of the emitters in the ensemble (Fig. 2.1d).

Since the laser pulse $\Omega(t)$ couples the microwave and optical transitions, we expect that unwanted variations in the transition frequencies can be compensated for by modulating the temporal form of this laser. However, in practical transduction systems, it is difficult to address individual emitters with separate lasers and consequently any modulation of $\Omega(t)$ impacts all the emitters. This makes designing the laser pulses difficult and calls for an application of numerical optimization techniques. We thus pose its design as maximizing the total power obtained in the optical mode when the

emitter ensemble is excited with a single photon in the microwave mode:

$$\begin{aligned} & \max_{\Omega(t)} \int_{-\infty}^{\infty} dt |a_{\text{opt}}(t)|^2 \\ \text{subject to } & i \frac{d|\psi_e(t)\rangle}{dt} = H_{\text{eff}}(\Omega(t)) |\psi_e(t)\rangle + a_{\mu}(t) L_{\mu}^{\dagger} |G\rangle, \\ & a_{\text{opt}}(t) = -i \langle G | L_{\text{opt}} | \psi_e(t) \rangle. \end{aligned} \quad (2.16)$$

where the time-domain wave-packets of the single microwave input photon and optical output photon are described by $a_{\mu}(t)$ and $a_{\text{opt}}(t)$ respectively, $|\psi_e\rangle$ is the state of the emitters in the ensemble, $|G\rangle$ is the ground state of the ensemble, and $H_{\text{eff}}(\Omega)$ is the non-Hermitian effective Hamiltonian of the system when all the emitters are uniformly driven by a laser with amplitude Ω . We point out that the constraints are simply the input-output equations describing the dynamics of the transduction process under excitation with a single photon. Furthermore, since experimentally realizable laser pulses will be band-limited, we parametrize $\Omega(t)$ as a finite sum of harmonics,

$$\Omega(t) = \sum_{n=0}^{N_h} \Omega_n \cos(n\omega_0 t + \phi_n), \quad (2.17)$$

consequently constraining its bandwidth to be $N_h\omega_0$. The design problem (2.16) can be solved using off-the-shelf gradient-based local optimizers. The gradient of the objective function in problem (2.16) with respect to the parameters Ω_n, ϕ_n can be computed using the time-domain adjoint variable method [92, 93].

2.2 Gradient-based optimization of drives

2.2.1 Adjoint variable method

The adjoint variable method can be used to calculate the gradient with respect to all the parameters describing the laser drive efficiently in only two simulations (named forward and backward simulations).

First, we rewrite Eq. 2.14 and Eq. 2.11 as,

$$i \frac{dy(t)}{dt} = (H_0 + \Omega(t)H_1)y(t) + v_\mu a_\mu(t) \quad (2.18)$$

$$a_{\text{opt}}(t) = v_{\text{opt}}^\dagger y(t), \quad (2.19)$$

where $y(t) := |\psi(t)\rangle$ is the vector describing the state of the ensemble, and

$$H_0 := \sum_i \left[\delta_\mu^i \sigma_\mu^{i\dagger} \sigma_\mu^i + \delta_{\text{opt}}^i \sigma_{\text{opt}}^{i\dagger} \sigma_{\text{opt}}^i \right] - \sum_i \left(\frac{i\Gamma_\mu}{2} \sigma_\mu^{i\dagger} \sigma_\mu^i - \frac{i\Gamma_{\text{opt}}}{2} \sigma_{\text{opt}}^{i\dagger} \sigma_{\text{opt}}^i \right) - \frac{i}{2} L_\mu^\dagger L_\mu - \frac{i}{2} L_{\text{opt}}^\dagger L_{\text{opt}} \quad (2.20)$$

$$H_1 := \sum_i (\sigma_\mu^{i\dagger} \sigma_{\text{opt}}^i + \text{H. c.}) \quad (2.21)$$

$$v_\mu := L_\mu^\dagger |G\rangle, \quad v_{\text{opt}} := iL_{\text{opt}}^\dagger |G\rangle \quad (2.22)$$

We discretize the total simulation time range $[0, T]$ into $N - 1$ steps of duration δt each. On this grid, the differential equation Eq. 2.18 can be discretized as,

$$y[k+1] = U[k] (y[k] - i\delta t a_\mu[k] v_\mu) \quad k \in \{0, \dots, N-2\} \quad (2.23)$$

$$y[0] = 0 \text{ (initial condition)}, \quad (2.24)$$

where, $U[k] := \exp(-i \delta t (H_0 + \Omega[k]H_1))$, $\Omega[k] := \Omega(k\delta t)$, $y[k] := y(k\delta t)$, $a_\mu[k] := a_\mu(k\delta t)$. We refer to solving this system of equations as the forward simulation.

The transduced power in the optical mode can be expressed in terms of the result of the forward simulation as,

$$P = \sum_{k=0}^{N-1} |a_{\text{opt}}[k]|^2 = \sum_{k=1}^{N-1} |v_{\text{opt}}^\dagger y[k]|^2. \quad (2.25)$$

The latter sum starts from $k = 1$ as $y[0] = 0$ is enforced as the initial condition.

The derivative of P with respect to the drive at the l th time step is,

$$\frac{\partial P}{\partial \Omega[l]} = \sum_{k=1}^{N-1} r[k]^\dagger \frac{\partial y[k]}{\partial \Omega[l]} + C.c., \quad (2.26)$$

where, ‘*C.c.*’ means ‘complex conjugate’ and $r[k] := (v_{\text{opt}}^\dagger y[k])^* v_{\text{opt}}$.

We construct the following block vectors and matrices,

$$y := \begin{pmatrix} y[1] \\ y[2] \\ \vdots \\ y[N-1] \end{pmatrix} \quad r := \begin{pmatrix} r[1] \\ r[2] \\ \vdots \\ r[N-1] \end{pmatrix} \quad a := -i \delta t \begin{pmatrix} a_\mu[1]v_\mu \\ a_\mu[2]v_\mu \\ \vdots \\ a_\mu[N-1]v_\mu \end{pmatrix} \quad (2.27)$$

$$M := \begin{pmatrix} 0 & \cdots & 0 \\ U[1] & & \vdots \\ & U[2] & \\ \vdots & & \ddots \\ 0 & \cdots & U[N-2] & 0 \end{pmatrix} \quad U := \begin{pmatrix} U[0] & 0 & \cdots & 0 \\ 0 & U[1] & \cdots & 0 \\ \vdots & \vdots & \ddots & \vdots \\ 0 & 0 & \cdots & U[N-2] \end{pmatrix}. \quad (2.28)$$

The only non-zero blocks in the matrix M are the subdiagonal blocks.

The forward simulation Eq. 2.23 can now be written as,

$$y = My + Ua \quad (2.29)$$

As $\frac{\partial U[k]}{\partial \Omega[l]} = 0$ if $k \neq l$, taking the derivative of Eq. 2.29 with respect to the drive at the l th time step results in,

$$\frac{\partial y}{\partial \Omega[l]} = M \frac{\partial y}{\partial \Omega[l]} + p[l] \quad (2.30)$$

$$\Rightarrow \frac{\partial y}{\partial \Omega[l]} = (\mathbf{1} - M)^{-1} p[l] \quad l \in \{0, \dots, N-2\} \quad (2.31)$$

where $\mathbb{1}$ is the identity matrix and,

$$p[l] = \begin{pmatrix} 0_{ld \times 1} \\ \alpha[l] \\ 0_{(N-l-2)d \times 1} \end{pmatrix} \quad (2.32)$$

$$\alpha[l] = \frac{\partial U[l]}{\partial \Omega[l]}(y[l] + \delta t a_\mu[l] v_\mu). \quad (2.33)$$

In Eq. 2.32, d is the dimension of the state vector $y(t)$ and $0_{m \times n}$ is a zero matrix of dimension $m \times n$. To calculate $\alpha[l]$, we estimate the derivative $\frac{\partial U[l]}{\partial \Omega[l]}$ by a finite difference.

Using Eq. 2.31 in Eq. 2.26, we have,

$$\frac{\partial P}{\partial \Omega[l]} = r^\dagger (\mathbb{1} - M)^{-1} p[l] + C.c. \quad (2.34)$$

We define a vector $q = (q[1], q[2], \dots, q[N-1])^T$ such that,

$$q^\dagger := r^\dagger (\mathbb{1} - M)^{-1} \quad (2.35)$$

$$\Rightarrow q = M^\dagger q + r \quad (2.36)$$

Using the definition of M and expanding out Eq. 2.36 in terms of the elements of q and r results in the following system of equations,

$$q[N-k] = U[N-k]^\dagger q[N-k+1] + r[N-k] \quad k \in \{2, 3, \dots, N-1\} \quad (2.37)$$

$$q[N-1] = r[N-1]. \quad (2.38)$$

We refer to $q[k]$ as the adjoint variables and to solving this system of equations (Eq. 2.37 and Eq. 2.38) as the backward simulation. The initial condition for the backward simulation is provided at the final time point unlike the forward simulation. Once the forward and backward simulations are done, the gradient with respect to the drive at each time step can be computed just with an inner product of two

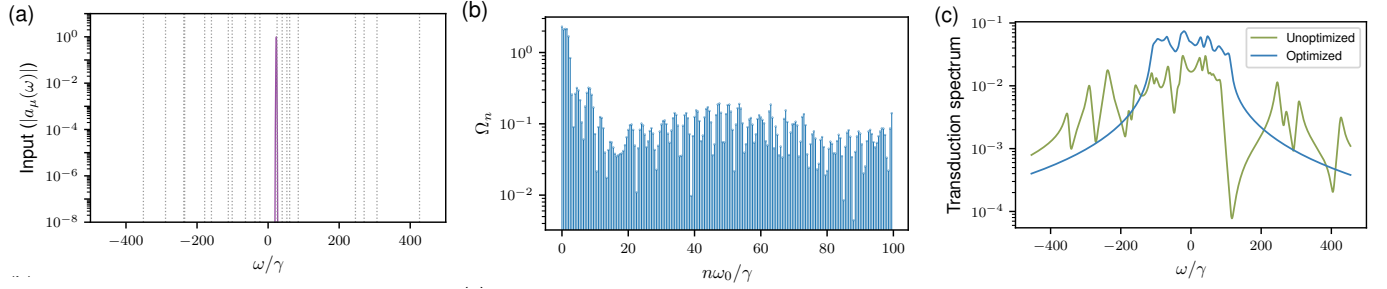


Figure 2.2: (a) Fourier transform of the input microwave field (Gaussian waveform). Dashed lines are representative of the individual emitter frequencies in a random ensemble ($N = 10$, $\Delta = 200\gamma$). (b) Amplitudes of the harmonic components of the optimized $\Omega(t)$ designed for the same ensemble. (c) Comparison of the transduction spectrum of the same ensemble with and without optimized drives applied — the transduction spectrum with the optimized drive is computed using a Floquet scattering theory approach [94].

d -dimensional vectors,

$$\frac{\partial P}{\partial \Omega[l]} = q^\dagger p[l] + C.c., \quad (2.39)$$

$$\Rightarrow \frac{\partial P}{\partial \Omega[l]} = q[l+1]^\dagger \alpha[l] + C.c. \quad (2.40)$$

The chain rule can then be used to compute the gradient with respect to the harmonic parameters Ω_n and ϕ_n ,

$$\frac{\partial P}{\partial \Omega_n} = \sum_{l=0}^{N-2} \frac{\partial \Omega[l]}{\partial \Omega_n} \frac{\partial P}{\partial \Omega[l]} = \sum_{l=0}^{N-2} \cos(n\omega_0 l \delta t + \phi_n) \frac{\partial P}{\partial \Omega[l]} \quad (2.41)$$

$$\frac{\partial P}{\partial \phi_n} = \sum_{l=0}^{N-2} \frac{\partial \Omega[l]}{\partial \phi_n} \frac{\partial P}{\partial \Omega[l]} = \sum_{l=0}^{N-2} -\Omega_n \sin(n\omega_0 l \delta t + \phi_n) \frac{\partial P}{\partial \Omega[l]} \quad (2.42)$$

2.2.2 Results

As an example, we consider a transduction system with $N = 10$ inhomogeneous emitters excited with a single microwave photon with a Gaussian spectrum. Figure 2.2a shows the spectrum of the input photon, with the dashed lines depicting the

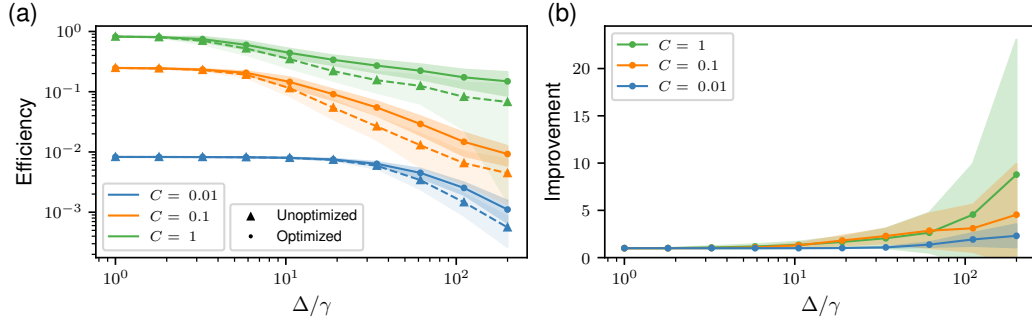


Figure 2.3: Optimized drives countering inhomogeneous broadening. (a) Transduction efficiency and (b) improvement in the transduction efficiency through randomly inhomogeneously broadened ensembles of $N = 10$ emitters with increasing inhomogeneous broadening for different cooperativities C when the optimized drives are applied. For each Δ , optimized drives are designed for each of the same 100 randomly generated ensembles with inhomogeneous broadening equal to Δ as used in Fig. 2.1c. Before running the optimizations, for each ensemble, the input photon is frequency-shifted to match the highest peak of the unoptimized transduction spectrum. Also, the initial condition for the optimization is $\Omega(t) = (N\gamma + \Gamma)/2$, which is a constant drive that maximises the transduction efficiency through a homogeneous ensemble with the same decay rates (see Appendix A). Improvement is defined as the ratio of the efficiencies with and without the optimized drive applied. Each plot point corresponds to the mean over the 100 ensembles with inhomogeneous broadening equal to the corresponding value of Δ and the shaded regions represent the standard deviation.

resonant frequencies of the transduction spectra of the individual emitters. Given its narrow bandwidth, we expect the input photon to effectively only interact with a single emitter, leading to a low transduction efficiency comparable to what can be achieved by using just one emitter instead of many. The optimized drive obtained on solving problem (2.16) is depicted in Fig. 2.2b — as can be seen from Fig. 2.2c, the transduction spectrum in the presence of the optimized drive shows improvement relative to the one with constant (unoptimized) drive.

Statistical studies of performance of the optimization procedure for different sets of emitter frequencies is shown in Fig. 2.3 — Fig. 2.3a shows the optimized transduction efficiencies and Fig. 2.3b shows the improvement in the transduction efficiencies. We

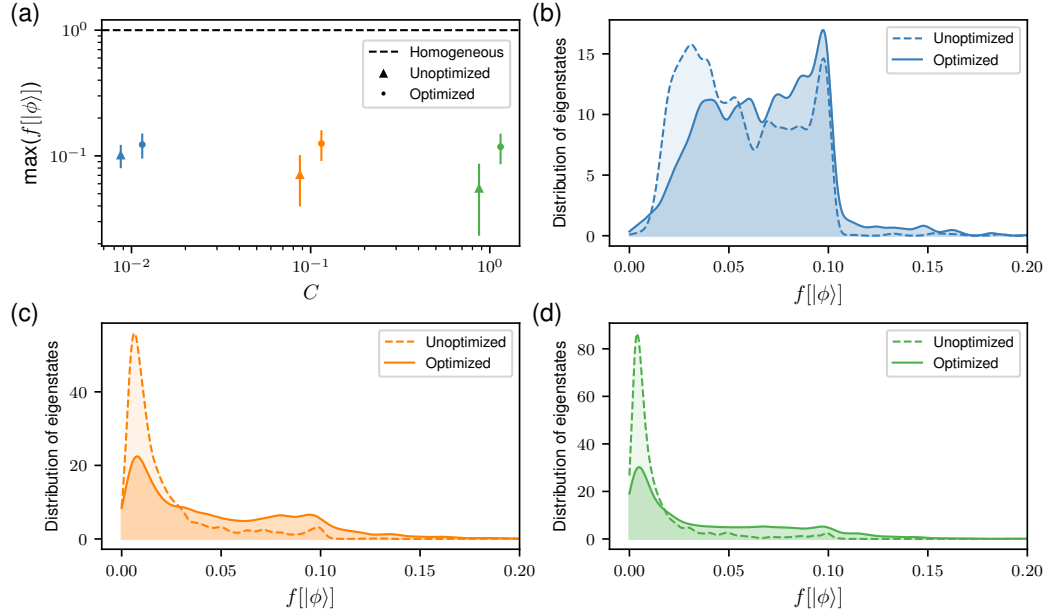


Figure 2.4: (a) Comparison of the superradiance metric for ensembles with inhomogeneous broadening $\Delta = 200\gamma$ with and without optimized drives applied (data for optimized and unoptimized cases are dodged in the plot for visual clarity). After generating the optimized drives used in Fig. 2.3, we compute the metric for all eigenstates of each of the 100 random ensembles with inhomogeneous broadening $\Delta = 200\gamma$ by numerically diagonalising the propagator over one time period of the effective Hamiltonian. Each plot point and associated error bars correspond to the mean and standard deviation (over the collection of ensembles with $\Delta = 200\gamma$) of the maximum value of the superradiance measure $f[|\phi\rangle]$ over all Floquet eigenstates $|\phi\rangle$. The dashed line denotes the same for a homogeneous ensemble. As we increase Γ to decrease the cooperativity, the metric is larger on average in the unoptimized case. We attribute this to the simultaneous increase in the unoptimized drive $\Omega(t) = (N\gamma + \Gamma)/2$ overshadowing the constant inhomogeneous broadening $\Delta = 200\gamma$ (see Appendix B). (b, c, d) Density plots (obtained by kernel density estimation using Gaussian kernels) of the superradiance measure for eigenstates of the 100 ensembles with inhomogeneous broadening $\Delta = 200\gamma$, (b) $C = 0.01$, (c) $C = 0.1$, (d) $C = 1$.

observe that the improvements are larger at higher inhomogeneous broadening. Furthermore, the cooperativities of the emitters set a limit on improvement that can be obtained by shaping the laser pulse — as can be seen from Fig. 2.3b, the improvements are generally smaller for lower cooperativities.

While it is intuitively expected that improvement in transduction efficiency with the application of an optimized drive is due to recovery of superradiance, this can be made more concrete by studying the Floquet eigenstates of the optimized (time-dependent) effective Hamiltonian. The ‘superradiance’ in an eigenstate $|\phi\rangle$ of the propagator over one time period of the effective Hamiltonian, can be quantified with the metric,

$$f[|\phi\rangle] = \frac{2}{N\sqrt{\gamma_\mu\gamma_{\text{opt}}}} |\langle G|L_{\text{opt}}|\phi\rangle\langle\phi|L_\mu^\dagger|G\rangle|. \quad (2.43)$$

For a homogeneous ensemble, the metric is 1 for two eigenstates formed by the drive-induced hybridization of superradiant states corresponding to the microwave and optical transitions. Furthermore, it is 0 for the remaining eigenstates since they are subradiant/dark. Since the eigenstates for an inhomogeneous ensembles are not perfectly superradiant or subradiant, their corresponding metric lies between 0 and 1 and quantifies the extent of their subradiant or superradiant character. Figure 2.4a indicates that an application of the optimized drive statistically increases the value of this metric, indicating partial recovery of superradiance. The density plots in Fig. 2.4(b, c, d) show the distribution of the superradiance metric of the eigenstates of an inhomogeneously broadened ensemble.

The results discussed above indicate that pulse-shaping the laser can be used to improve the performance of transduction systems. However, the optimized laser pulses can only be computed if the emitter frequencies are known. For systems with large number of emitters, such characterization might not be practical at scale and it would be desirable to find an optimized pulse which is robust to the specific frequencies of the emitters and depends only on their distribution. To design such a laser pulse, we modify the optimization problem (2.16) to

$$\begin{aligned} \max_{\Omega(t)} \quad & \frac{1}{N_s} \sum_{n=1}^{N_s} \int_{-\infty}^{\infty} dt \left| a_{\text{opt}}^{(n)}(t) \right|^2 \\ \text{s.t.} \quad & i \frac{d|\psi_e^{(n)}(t)\rangle}{dt} = H_{\text{eff}}^{(n)}(\Omega(t)) |\psi_e^{(n)}(t)\rangle + a_\mu(t) L_\mu^\dagger |G\rangle, \\ & a_{\text{opt}}^{(n)}(t) = -i \langle G|L_{\text{opt}}|\psi_e^{(n)}(t)\rangle, \end{aligned} \quad (2.44)$$

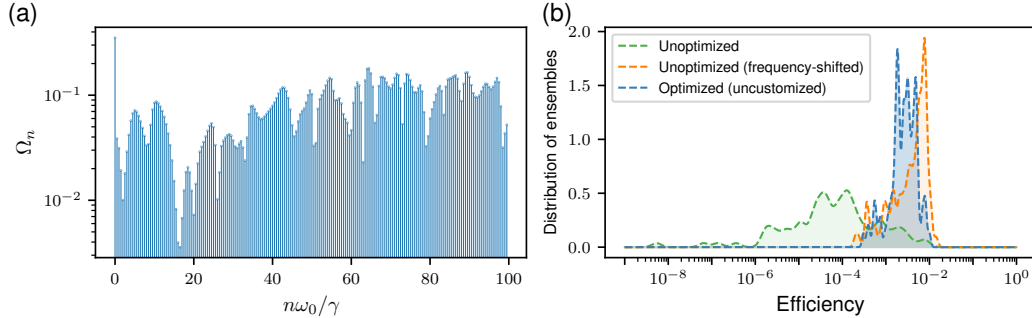


Figure 2.5: Transduction efficiency improvement with uncustomized optimization. (a) Amplitudes of the frequency components comprising the uncustomized drive. (b) Density plots of the transduction efficiency through 100 ensembles (test set) with $\Delta = 200\gamma$, $C = 0.1$ for three cases – (green) no optimised drive is applied and the input photon is fixed at the resonance of a homogeneous ensemble, (orange) no optimised drive is applied but the input photon is frequency-shifted to match the highest peak of the unoptimized transduction spectrum for each inhomogeneous ensemble, and (blue) the uncustomized optimized drive is applied and the input photon is fixed at the resonance of a homogeneous ensemble.

where we generate N_s inhomogeneous emitter samples from the same inhomogeneous broadening distribution and find a laser pulse that $\Omega(t)$ that optimizes the average transduced power over all the samples. The superscript over a quantity in problem (2.44) indicates that that quantity is computed for a specific sample. We design such a drive, shown in Fig. 2.5a, for a training set of $N_s = 100$ random ensembles with inhomogeneous broadening $\Delta = 200\gamma$ and with the input-photon being incident at the resonance of a homogeneous ensemble. Figure 2.5b shows the resulting improvement in transduction efficiency from applying the optimized drive to a test set of 100 random ensembles that are generated from the same inhomogeneous broadening distribution, independently of the training set. While there is significant improvement over the unoptimized case, we point out that simply shifting the spectrum of the input photon without shaping the driving laser pulse results in similar improvements. Therefore, it is not expected that this optimized drive is restoring superradiance in the emitter ensemble, rather it is effectively matching the resonance of the transduction spectrum to the input photon in a manner robust to the specific emitter

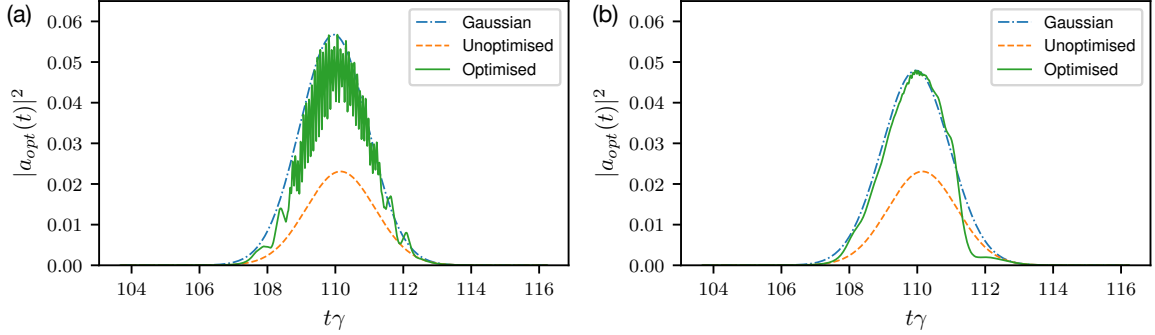


Figure 2.6: Temporal mode overlap-based design of drives. The amplitude $|a_{\text{opt}}(t)|^2$ of the output photon’s temporal wave-packet after transduction by an ensemble of $N = 3$ emitters, with $C = 0.1$, $\Delta \approx 61.61\gamma$, and under the application of drives obtained by locally solving problem (2.45) for (a) $c_0 \approx 1.331, c_1 = 0$ (b) $c_0 \approx 1.331, c_1 \approx 247.02$. The improvement in transduction efficiencies are (a) $4.466\times$ and (b) $3.977\times$, respectively.

frequencies. This could still be technologically useful since this optimized drive is agnostic to the specific emitter frequencies, thus obviating the need to characterize the emitter resonances. Furthermore, if many transducers are to be operated simultaneously, experimentally realizing and supplying drives customized to each transducer can be challenging to scale — having a common, uncustomized drive would solve this problem.

Quantum information can be encoded in the temporal modes of photons for the purposes of quantum communication [95]. Such encoding would necessitate a transduction process that preserves the fidelity of the transduced photon’s wave-packet to specific temporal modes. We demonstrate that it is possible to extend our design method to compensate for inhomogeneous broadening and produce improvements in transduction efficiency while preserving the overlap with a specified temporal mode. To achieve this, we pose the design of the drive as maximising the overlap of the output photon’s temporal wave-packet with a specified Hermite-Gaussian function [96] while simultaneously minimising its overlap with unwanted Hermite-Gaussian

functions. For example,

$$\max_{\Omega(t)} \left| \int_{-\infty}^{\infty} dt c_0 \varphi_0(t) a_{\text{opt}}(t) \right|^2 - \left| \int_{-\infty}^{\infty} dt c_1 \varphi_1(t) a_{\text{opt}}(t) \right|^2 \quad (2.45)$$

$$\text{subject to } i \frac{d|\psi_e(t)\rangle}{dt} = H_{\text{eff}}(\Omega(t)) |\psi_e(t)\rangle + a_{\mu}(t) L_{\mu}^{\dagger} |G\rangle, \quad (2.46)$$

$$a_{\text{opt}}(t) = -i \langle G | L_{\text{opt}} | \psi_e(t) \rangle. \quad (2.47)$$

where $\varphi_0(t)$ and $\varphi_1(t)$ are the 0th- and 1st-order Hermite-Gaussian functions (normalized to unity) [96] and the coefficients $c_0, c_1 \geq 0$ represent their weights. We solve problem (2.45) for an input microwave photon with a Gaussian wave-packet incident on a randomly generated inhomogeneous ensemble with $N = 3$ emitters for two cases: $c_1 = 0$ and $c_1 \neq 0$. Fig. 2.6 shows that, in both cases, we observe improved transduction efficiencies and the fidelity to the 0th-order mode is higher when $c_1 \neq 0$, in which case the output photon's shape closely resembles a Gaussian function. In case the input photon occupies a mode other than the 0th-order mode, this approach can be extended to design drives that improve the overlap of output photons with other Hermite-Gaussian modes too.

2.3 Optimality of drive design

We address the question about the optimality of the laser pulses calculated using the gradient-based optimization algorithm. Since the optimization problem (2.16) is non-convex, we can only solve it locally and calculating the solution globally will likely be hard. However, one method to assess how close the laser pulses obtained above are to the globally optimal solution is to calculate upper bounds on the achievable transduction efficiency and compare it to the locally optimized results.

The physically motivated idea behind calculating such an upper bound is to note that the efficiency is limited by the amplitude of the emitters in their excited state while interacting with the input photon, as well as the time that the emitters spend in the excited state. More rigorously, in the presence of the incident single-photon wave-packet as well as a decay of the excited state, the time-integrated norm of the excited

state amplitude $|\psi_e(t)\rangle$ cannot be arbitrarily high. Consequently, an upper bound on the transduction efficiency can be obtained by simply maximizing the emitted photon energy as only constrained by this norm, which translates to solving the following optimization problem

$$\begin{aligned} & \max_{\Omega(t)} \int_{-\infty}^{\infty} |a_{\text{opt}}(t)|^2 dt \\ \text{subject to} & \int_{-\infty}^{\infty} \|\psi_e(t)\rangle - |\psi_{e,0}(t)\rangle\|_2^2 dt \leq \varepsilon \\ & a_{\text{opt}}(t) = -i\langle G|L_{\text{opt}}|\psi_e(t)\rangle, \end{aligned} \quad (2.48)$$

where $|\psi_{e,0}(t)\rangle$ is a reference state, $\|\cdot\|_2$ denotes the l_2 -norm, and ε is parameter that can be considered as the solution of the following optimization problem:

$$\begin{aligned} & \max_{\Omega(t)} \int_{-\infty}^{\infty} \|\psi_e(t)\rangle - |\psi_{e,0}(t)\rangle\|_2^2 dt \\ \text{subject to} & i\frac{d|\psi_e(t)\rangle}{dt} = H_{\text{eff}}(\Omega(t))|\psi_e(t)\rangle + a_{\mu}(t)L_{\mu}^{\dagger}|G\rangle. \end{aligned} \quad (2.49)$$

We point out that since by construction ε provides an upper bound on the integrated norm of the difference of the excited state from the reference state for all allowed laser pulses, the optimization problem 2.48 is a *relaxation* of the original non-convex optimization problem (problem 2.16). Therefore, the solution of problem 2.48 provides an upper bound to the (global) solution of problem 2.16.

Problem (2.48) is a quadratically-constrained quadratic program and bounds on its optimal value can be calculated by using the principle of Lagrangian duality [97, 98], as we describe in the next section. However, computing ε , which is required to solve problem 2.48, again requires solving a non-convex problem (problem 2.49). In order to get around this issue, as explained below, we construct a provable upper bound, ε_c on ε which can also be used together with problem 2.48 to obtain an upper bound on the transduction efficiency. We point out that this bound will be looser than the one obtained on using ε , i.e., the tighter the bound on the norm of the excited state, the better the bound on the transduction efficiency.

2.3.1 Lagrangian duals

In this section, we first show that the Lagrange dual for optimization problem (2.16) leads to a trivial bound, then we derive the Lagrange dual for the distance-constrained problem (2.48), and finally provide a derivation for the upper bound ε_c on the optimal value of problem (2.49).

For notational clarity, we rewrite problem (2.16) in the following manner,

$$\max_{\Omega(t), y(t)} \int_{-\infty}^{\infty} y(t)^\dagger v_{\text{opt}} v_{\text{opt}}^\dagger y(t) dt \quad (2.50)$$

$$\text{subject to } \frac{dy(t)}{dt} = -i(H_0 + \Omega(t)H_1)y(t) - iv_\mu a_\mu(t), \quad (2.51)$$

where $y(t) := |\psi_e(t)\rangle$ and $H_0, H_1, v_\mu, v_{\text{opt}}$ are defined in Eqs. 2.20, 2.21, 2.22.

Introducing the dual variables $\eta(t)$, the Lagrangian for problem (2.16) is:

$$\mathcal{L}(y(t), \Omega(t); \eta(t)) = \int_{-\infty}^{\infty} y(t)^\dagger V y(t) dt + \quad (2.52)$$

$$2 \int_{-\infty}^{\infty} \text{Re} \left[\eta(t)^\dagger \left(\frac{dy(t)}{dt} + iH_1\Omega(t)y(t) + iH_0y(t) + iv_\mu a_\mu(t) \right) \right], \quad (2.53)$$

where $\text{Re}[\cdot]$ denotes the real part of a complex number and $V := v_{\text{opt}} v_{\text{opt}}^\dagger$. We point out that V is a positive-definite matrix.

Integrating by parts the term with the derivative of the state in the equation above, we have,

$$\mathcal{L}(y(t), \Omega(t); \eta(t)) = \int_{-\infty}^{\infty} y(t)^\dagger V y(t) dt + \lim_{T \rightarrow \infty} 2 \text{Re} [\eta(T)^\dagger y(T) - \eta(-T)^\dagger y(-T)] + \quad (2.54)$$

$$\int_{-\infty}^{\infty} 2 \text{Re} [z(t)^\dagger y(t)] dt + \int_{-\infty}^{\infty} 2 \text{Re} [i \eta(t)^\dagger v_\mu a_\mu(t)], \quad (2.55)$$

where

$$z(t) := -\frac{d\eta(t)}{dt} - iH_1\Omega(t)\eta(t) - iH_0\eta(t). \quad (2.56)$$

The Lagrange dual function $g(\eta(t))$ is given by,

$$g(\eta(t)) := \sup_{y(t), \Omega(t)} \mathcal{L}(y(t), \Omega(t); \eta(t)), \quad (2.57)$$

where sup denotes the supremum. As the matrix V is positive-definite, the supremum of the Lagrangian over $y(t)$ is unbounded as the norm of $y(t)$ increases, and hence the dual function is unbounded too. Therefore, in this case, Lagrangian duality reveals a trivial upper bound on the transduced power.

On the other hand, the Lagrangian for problem (2.48) is

$$\mathcal{L}(y(t); \lambda) = \int_{-\infty}^{\infty} y(t)^\dagger V y(t) dt + \lambda \left(\varepsilon - \int_{-\infty}^{\infty} \|y(t) - y_0(t)\|_2^2 dt \right) \quad (2.58)$$

$$= \int_{-\infty}^{\infty} y(t)^\dagger (V - \lambda \mathbf{1}) y(t) dt + \lambda \left(\varepsilon - \int_{-\infty}^{\infty} \|y_0(t)\|_2^2 dt \right) + \int_{-\infty}^{\infty} 2 \operatorname{Re} [z(t)^\dagger y(t)] dt \quad (2.59)$$

where $y_0(t) := |\psi_{e,0}(t)\rangle$ is the reference state, λ is a dual variable and $z(t) := \lambda y_0(t)$.

The corresponding dual function is,

$$g(\lambda) = \sup_{y(t)} \mathcal{L}(y(t); \lambda) \quad (2.60)$$

$$= \begin{cases} \int_{-\infty}^{\infty} z(t)^\dagger (\lambda \mathbf{1} - V)^{-1} z(t) dt + \lambda \left(\varepsilon - \int_{-\infty}^{\infty} \|y_0(t)\|_2^2 dt \right), & \text{if } \lambda \mathbf{1} - V \geq 0 \\ \infty, & \text{otherwise} \end{cases} \quad (2.61)$$

To obtain the least upper bound, the dual function has to be minimised, leading to

the following Lagrange dual problem,

$$\begin{aligned} \min_{\lambda, \beta(t)} \quad & \int_{-\infty}^{\infty} \beta(t) dt + \lambda \left(\varepsilon - \int_{-\infty}^{\infty} \|y_0(t)\|_2^2 dt \right) \\ \text{subject to} \quad & \beta(t) \geq z(t)^\dagger (\lambda \mathbb{1} - V)^{-1} z(t) \\ & \lambda \mathbb{1} - V \geq 0, \end{aligned}$$

where we have introduced additional dual variables $\beta(t)$.

The analytical upper bound on ε^* can be derived by rewriting Eq. 2.18 as,

$$\frac{dy(t)}{dt} = (-iH_{\text{sys}}(\Omega(t)) - D)y(t) - iv_\mu a_\mu(t) \quad (2.62)$$

where $H_{\text{sys}}(\Omega(t))$ is defined in Eq. 2.2 and,

$$D := \sum_i \left(\frac{\Gamma_\mu}{2} \sigma_\mu^{i\dagger} \sigma_\mu^i + \frac{\Gamma_{\text{opt}}}{2} \sigma_{\text{opt}}^{i\dagger} \sigma_{\text{opt}}^i \right) + \frac{1}{2} L_\mu^\dagger L_\mu + \frac{1}{2} L_{\text{opt}}^\dagger L_{\text{opt}}. \quad (2.63)$$

Using the fact that $D^\dagger = D$, the time-evolution of the norm of the state can be written as,

$$\frac{dy(t)^\dagger y(t)}{dt} = -2y(t)^\dagger D y(t) + 2 \text{Re} [-iy(t)^\dagger v_\mu a_\mu(t)] \quad (2.64)$$

$$\leq -2d_{\min} y(t)^\dagger y(t) + 2 \text{Re} [-iy(t)^\dagger v_\mu a_\mu(t)], \quad (2.65)$$

where d_{\min} is the smallest eigenvalue of D .

From the inequality (2.65) we have,

$$\|y(t)\|_2^2 \leq \int_0^t e^{-2d_{\min}(t-\tau)} 2 \text{Re} [-iy(\tau)^\dagger v_\mu a_\mu(\tau)] d\tau \quad (2.66)$$

$$\leq \int_0^t 2e^{-2d_{\min}(t-\tau)} \|y(\tau)\|_2 \|v_\mu a_\mu(\tau)\|_2 d\tau \quad (2.67)$$

$$\leq \int_0^t 2e^{-2d_{\min}(t-\tau)} \|v_\mu a_\mu(\tau)\|_2 d\tau := d(t), \quad (2.68)$$

where, to go from (2.67) to (2.68) we use the fact $\|y(t)\|_2 \leq 1, \forall t$.

Therefore,

$$\int_{-\infty}^{\infty} \|y(t) - y_0(t)\|_2^2 dt \leq \int_{-\infty}^{\infty} (\|y(t)\|_2 + \|y_0(t)\|_2)^2 dt \quad (2.69)$$

$$\leq \int_{-\infty}^{\infty} \left(\sqrt{d(t)} + \|y_0(t)\|_2 \right)^2 dt := \varepsilon_c \quad (2.70)$$

2.3.2 Results

Fig. 2.7 shows numerical studies of the upper bounds calculated on the transduction efficiency together with its comparison with the locally optimized results. In our studies, we solve problem 2.48 to compute both a *certifiable* bound, which uses the upper bound ε_c on ε , and a *heuristic* bound calculated with only locally optimal solutions of problem 2.49. As physically expected, the bounds decrease on average with increasing inhomogeneous broadening and are higher for higher cooperativities. Furthermore, the optimized transduction efficiencies are within an order of magnitude of the bound, which provides us with an estimate of the performance of the optimization method.

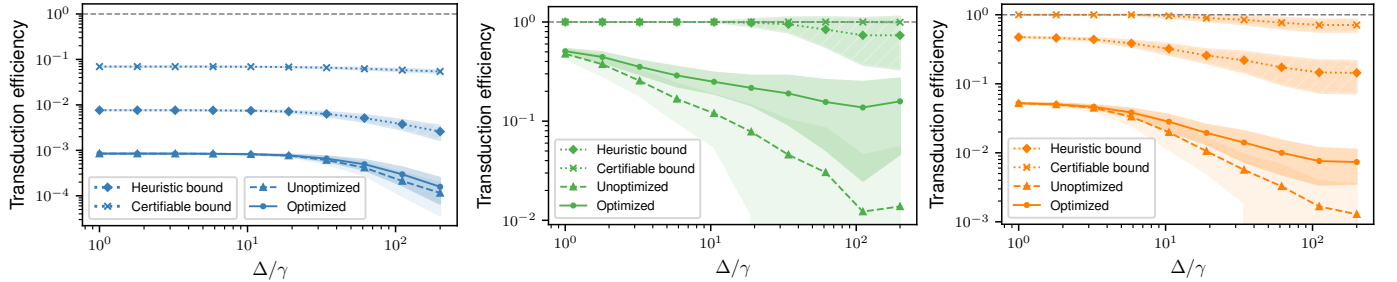


Figure 2.7: Heuristic and certifiable upper bounds and unoptimized and optimized transduction efficiencies calculated for ensembles with $N = 3$ emitters and cooperativities (a) $C = 0.01$, (b) $C = 0.1$, (c) $C = 1$. For each Δ , 100 random ensembles are generated with inhomogeneous broadening equal to Δ . For each such ensemble, optimized drives are designed to improve transduction efficiency by using a local optimizer to solve problem (2.16). Then, using the state obtained by solving the input-output equation with the aforementioned optimized drive as the reference state, heuristic and certifiable bounds are calculated. Each plot point corresponds to the mean over the 100 ensembles with inhomogeneous broadening equal to the corresponding value of Δ and the shaded regions represent the standard deviation.

2.4 Conclusion

In summary, we employed gradient-based inverse design of the temporal shape of the driving field as a technique to compensate for the effects of inhomogeneous broadening to help realize more efficient transducers. We demonstrated that optimized driving fields can lead to improvement in transduction efficiencies and showed that this improvement can be correlated with restoration of superradiant effects. Finally, to characterise the limits of the performance of time-dependent drives obtained by optimization-based design, we calculated upper bounds on optimal transduction efficiencies.

Chapter 3

Classically computing performance bounds on noisy quantum circuits

One of the most promising computational tasks at which fault-tolerant quantum computers could potentially outperform classical computers is the problem of finding the ground state of a given many-body Hamiltonian — a problem that naturally arises in studying equilibrium properties of condensed matter systems [21]. Moreover, classical optimization problems can also be framed as finding ground states of commuting Hamiltonians [22]. There has been extensive research on ground state-finding algorithms [23, 24, 25], for example, those based on phase estimation and adiabatic evolution [99, 100], and heuristic approaches like quantum adiabatic algorithms or variational quantum algorithms [26, 27, 28, 29].

Presently realizable noisy-intermediate scale quantum devices, however, are not fault-tolerant and consequently noise places a severe constraint on the performance of these quantum algorithms. It has thus become of interest to develop no-go results by providing theoretical bounds on the minimum energy that a noisy quantum circuit can achieve for a given Hamiltonian — if a classical algorithm [30, 31, 32] could obtain an energy better than this lower bound, then we can conclude that a reduction in noise rate is necessarily needed for a possible quantum advantage.

The impact of noise on quantum algorithms can be assessed by directly simulating the

circuit, e.g. by tensor network methods [101, 102, 103] — in fact, the classical simulation is made easier by the presence of noise [104, 105]. However, most of the tensor network methods lack rigorous accuracy guarantees and cannot certify an accurate simulation of the quantum circuit, especially in low noise regimes. Alternatively, this problem has been approached analytically using tools from quantum information theory. For instance, Refs. [33, 34, 35] analyzed the increase in entropy of the quantum state due to noise, and showed that it can allow for an analytical lower bound on the attainable minimum energy. However, while providing rigorous no-go results, these analyses were circuit-architecture independent and were thus expected to underestimate the impact of noise. Certain circuit architectures are expected to significantly worsen the impact of noise, and this phenomena has been theoretically demonstrated in random quantum circuits models [106, 107]. However, it remains unclear if it is possible to provide an architecture-dependent lower bound for a specific engineered quantum circuit.

We propose a method for efficiently computing rigorous bounds on the performance of any *specified* quantum circuit in the presence of a constant rate of depolarizing noise. The key insight behind our proposed method is the formulation of a Lagrangian dual corresponding to the circuit dynamics, which allows us to account for the circuit architecture in addition to the increase in the entropy, or equivalently, the decrease in the purity of the quantum state. We show that the Lagrangian dual yields a hierarchy of classically computable lower bounds on energy, with respect to a specified Hamiltonian, obtained at the output of a noisy quantum circuit. We provide numerical and analytical evidence that this formulation can capture the circuit-architecture dependent propagation of errors through the noisy quantum circuit and thus provide more stringent lower bounds than currently available.

3.1 Notation

Given a finite-dimensional Hilbert space \mathcal{H} , we use $\mathcal{D}_1(\mathcal{H})$ to denote the set of all density matrices on \mathcal{H} , and $\mathcal{M}(\mathcal{H})$ to denote the set of Hermitian linear operators on \mathcal{H} . Unless otherwise mentioned, for any linear operator A on \mathcal{H} , $\|A\|$ will denote

its operator norm i.e. the maximum singular value of A and $\|A\|_F = \sqrt{\text{Tr}(A^\dagger A)}$ will denote its Frobenius norm.

We use the computer-science big-O notation for function asymptotics. In particular, given two functions $f, g : [0, \infty) \rightarrow [0, \infty)$, $f = O(g)$ if, for some $c > 0$, $f(x) \leq cg(x)$ as $x \rightarrow \infty$ and $f = \Omega(g)$ if, for some $c > 0$, $f(x) \geq cg(x)$ as $x \rightarrow \infty$.

3.2 Duality based bounds

3.2.1 Single-qubit example

As a simple illustrative example of the Lagrangian dual formulation, we first consider a single-qubit circuit [Fig. 3.1(a)] — consider a qubit initially in $|0\rangle$, with a gate $U = e^{-i\theta Y}$ being applied on it followed by depolarizing noise with probability p . We would like to find the parameter θ to minimize the energy corresponding to the Hamiltonian $H = \Delta Z$ — in the absence of noise ($p = 0$), it is straightforward to verify that this would be accomplished by setting $\theta = \pi/2$ to obtain an energy $-\Delta$.

However, in the presence of depolarizing noise, the qubit will necessarily be in a mixed state. The extent to which the state is mixed can be quantified with a purity measure, for instance the von Neumann entropy of the qubit state, its trace purity or even higher order Renyi Entropies [108]. For concreteness, we use the trace purity measure of a state ρ : $P(\rho) = \text{Tr}(\rho^2)$ — $P(\rho) = 1$ if and only if ρ is a pure state, else $P(\rho) < 1$. Now, since the state ρ_θ at the output of the single-qubit circuit in Fig. 3.1(a) is obtained by applying the depolarizing noise channel to a single qubit pure state, $P(\rho_\theta) = P_0 := p^2/4 + (1 - p/2)^2 < 1$. Since ρ_θ is necessarily mixed, it cannot produce the pure ground state of the Hamiltonian H perfectly irrespective of the choice of θ — in fact, this simple observation can be used to lower bound the energy that can possibly be obtained at the output of the circuit by minimizing it with respect to states with purity at-most P_0 i.e. solving the following optimization

problem,

$$\begin{aligned} & \underset{\rho \in \mathcal{D}_1(\mathbb{C}^2)}{\text{minimize}} && \text{Tr}(H\rho) \\ & \text{subject to} && P(\rho) \leq P_0, \end{aligned} \tag{3.1}$$

where $\mathcal{D}_1(\mathbb{C}^d)$ is the space of density matrices on the Hilbert space \mathbb{C}^d . The optimization problem in Eq. 3.1 is solved by $\rho = (1 - p/2)|1\rangle\langle 1| + (p/2)|0\rangle\langle 0|$ with energy $-\Delta(1 - p)$. This bound clearly exhibits the intuitively expected dependence on the noise rate p — if $p = 0$, then the energy attained coincides with the ground state energy of $-\Delta$, and if $p = 1$, it is simply the energy obtained by the maximally mixed state.

However, this bound does not account for the unitary being applied on the qubit, and a better bound can be obtained by explicitly accounting for the circuit. To do so, we use the method of Lagrange duality [109, 110]. For this, we extend the problem in

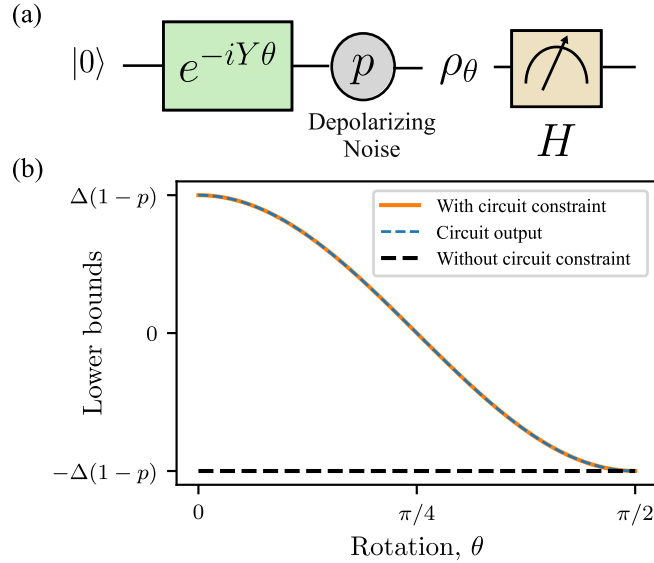


Figure 3.1: Comparison of bounds, with and without accounting for circuit constraints, on the minimum energy corresponding to the Hamiltonian $H = \Delta Z$ attainable by the output of the single qubit circuit shown in the schematic. The circuit consists of a Y-axis rotation followed by depolarizing noise acting with probability p .

Eq. 3.1 by adding an additional constraint due to the circuit:

$$\begin{aligned} & \underset{\rho \in \mathcal{D}_1(\mathbb{C}^2)}{\text{minimize}} && \text{Tr}(H\rho) \\ & \text{subject to} && \rho = \mathcal{E}_\theta(\rho_0), \\ & && P(\rho) \leq P_0, \end{aligned} \tag{3.2}$$

where $\rho_0 = |0\rangle\langle 0|$ and \mathcal{E}_θ is the channel corresponding to the unitary $e^{-iY\theta}$ followed by the single-qubit depolarizing noise. Note that the purity constraint $P(\rho) \leq P_0$ is redundant and is already implied by the circuit constraint $\rho = \mathcal{E}_\theta(\rho_0)$. However, as we will see in the following discussion, while redundant constraints do not impact the solution of an optimization problem, depending on the specific technique used to obtain a lower bound on the problem, they can have a considerable impact.

To provide a lower bound on this optimization, we construct its Lagrangian $\mathcal{L}(\sigma, \lambda)$ by introducing Lagrange multipliers $\sigma \in \mathcal{M}(\mathbb{C}^2)$, and $\lambda \geq 0$,

$$\begin{aligned} \mathcal{L}(\rho, \sigma, \lambda) &= \text{Tr}[H\rho] + \text{Tr}[\sigma(\rho - \mathcal{E}_\theta(|0\rangle\langle 0|))] \\ &+ \lambda(P(\rho) - P_0). \end{aligned} \tag{3.3}$$

$\mathcal{L}(\rho, \sigma, \lambda)$ can be considered to be a modified energy function which, in addition to the energy $\text{Tr}[H\rho]$, also penalizes violation of the two constraints: $\rho = \mathcal{E}_\theta(\rho_0)$ imposed by the circuit and $P(\rho) \leq P_0$ on the purity of the state ρ . Minimizing the Lagrangian with respect to ρ , we obtain the *dual function*,

$$g(\sigma, \lambda) = \min_{\rho} \mathcal{L}(\rho, \sigma, \lambda), \tag{3.4}$$

which is a function of σ, λ , the *dual variables*. It follows from the principle of Lagrange duality that for any σ and $\lambda \geq 0$, $g(\sigma, \lambda)$ is a lower bound on the energy attained by the circuit. This can easily be seen from Eq. 3.3 by noting that when \mathcal{L} is evaluated at the circuit output $\rho_\theta = \mathcal{E}_\theta(|0\rangle\langle 0|)$, we obtain

$$\mathcal{L}(\rho_\theta, \sigma, \lambda) = \text{Tr}[H\rho_\theta] + \lambda(P(\rho_\theta) - P_0) \leq \text{Tr}[H\rho_\theta],$$

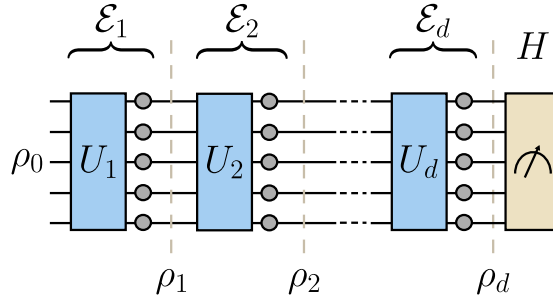


Figure 3.2: Schematic depiction of the problem setting. The unitaries (colored boxes) implement a quantum algorithm to prepare an approximation of the ground state of a target Hamiltonian H in the absence of noise. Each layer of unitary is followed by single-qubit depolarizing noise (gray circles) on the qubits applied with a probability p .

since $P(\rho_\theta) \leq P_0$ and $\lambda \geq 0$. Since from Eq. 3.4 $g(\sigma, \lambda)$ is the smallest attainable value of $\mathcal{L}(\rho, \sigma, \lambda)$ on varying ρ , we obtain $g(\sigma, \lambda) \leq \text{Tr}[H\rho_\theta]$. We emphasize that the dual function $g(\sigma, \lambda)$, evaluated at any $\sigma, \lambda \geq 0$, is a lower bound on the energy $\text{Tr}[H\rho_\theta]$ attained by the circuit, and the best lower bound can be obtained by maximizing $g(\sigma, \lambda)$ with respect to σ, λ . Furthermore, since the construction of the dual function explicitly accounts for the circuit constraint, it gives a better bound than obtained from the problem in Eq. 3.1 i.e. by just accounting for the final purity of the state. This is exhibited in Fig. 3.1(b), where $\max_{\sigma, \lambda \geq 0} g(\sigma, \lambda)$ compared with $-\Delta(1-p)$ and it can be seen that the dual function provides a better lower bound for most values of θ . For the simple example of a single qubit, the duality-based bound that we can compute coincides exactly with the circuit output and thus models it exactly. As we will see in the next sections, this will not be the case for circuits over a large number of qubits.

3.2.2 General formulation

We can now extend the duality lower bound to more general quantum circuits [Fig. 3.2] — consider a quantum circuit of depth d , consisting of unitaries $U_1, U_2 \dots U_d$ that has been designed to approximate the ground state of a target Hamiltonian H of N qubits. In the presence of noise, the state becomes increasingly mixed as the

unitaries are applied on it — while it is typically hard to compute exactly how mixed the state is, an analytical upper bound on several purity measures can be obtained. In particular, Refs. [33, 35] establish explicit upper bounds for two purity measures after t time-steps — the information content of the quantum state, as well as its trace purity.

Lemma 1 [Refs. [33], [35]] *Suppose ρ_t is the quantum state on N qubits obtained from an initial pure state after applying t unitaries and single qubit depolarizing channels, then*

$$\begin{aligned} I(\rho_t) &:= N + \text{Tr}[\rho_t \log_2(\rho_t)] \leq N(1 - p)^t, \\ P_{\text{tr}}(\rho_t) &:= \text{Tr}(\rho_t^2) \leq 2^{-N(1 - (1-p)^t)}, \end{aligned}$$

where p is the probability of applying the depolarizing noise at each time-step independently on each qubit.

Both the information content and trace purity can be viewed as measures of how mixed the given state is. Both are largest for a pure state ($I(|\psi\rangle\langle\psi|) = N$ and $P_{\text{tr}}(|\psi\rangle\langle\psi|) = 1$), and are lowest for the maximally mixed state ($I(I/2^N) = 0$ and $P_{\text{tr}}(I/2^N) = 2^{-N}$).

In the remainder of this subsection, we denote by P_t an upper bound on the purity of the state at t^{th} time-step — we will formulate the results of this subsection for general convex purity measures, and specialize them to concrete purity measures (such as information content or trace purity) in the following sections. Now, as with the single-qubit case, the energy attained at the output of the circuit can now be written as,

$$\begin{aligned} &\underset{\rho_1, \rho_2, \dots, \rho_d \in \mathcal{S}}{\text{minimize}} && \text{Tr}(H\rho_d) \\ &\text{subject to} && \rho_t = \mathcal{E}_t(\rho_{t-1}), \quad t \in \{1, \dots, d\}, \\ &&& P(\rho_t) \leq P_t, \quad t \in \{1, \dots, d\}, \end{aligned} \tag{3.5}$$

where $\mathcal{E}_t(\cdot)$ is the quantum channel that applies the unitary U_t for the t^{th} layer of the

circuit followed by depolarizing noise acting individually on the qubits, and ρ_0 is a fixed and known initial state. Importantly, in Eq. 3.5, \mathcal{S} is the set of N qubit operators over which we allow the states $\rho_1, \rho_2 \dots \rho_d$ to vary — this set can be chosen to be *any* set containing density matrices over N qubits $\mathcal{D}_1((\mathbb{C}^2)^{\otimes N})$ since the circuit constraints ($\rho_t = \mathcal{E}_t(\rho_{t-1})$) enforce $\rho_1, \rho_2 \dots \rho_d$ to be valid density matrices. For instance, \mathcal{S} can be chosen to be just the set of N -qubit Hermitian operators, or the set of N -qubit Hermitian operators with unity trace. As we will see below, the choice of this set together with the purity measure determines the form of the dual function.

To construct the dual function corresponding to Eq. 3.5 — we introduce the dual variables $\vec{\sigma} = \{\sigma_1, \sigma_2 \dots \sigma_d\}$, which are N -qubit Hermitian operators, corresponding to the circuit constraints and $\vec{\lambda} = \{\lambda_1, \lambda_2 \dots \lambda_d \geq 0\}$ corresponding to the purity constraints. The Lagrangian is now constructed by adding penalties corresponding to the circuit constraints and purity constraints at each time-step to the output energy:

$$\begin{aligned} \mathcal{L}(\vec{\rho}, \vec{\sigma}, \vec{\lambda}) &= \text{Tr}[H\rho_d] + \sum_{t=1}^d \text{Tr} \left[\sigma_t (\rho_t - \mathcal{E}_t(\rho_{t-1})) \right] + \\ &\quad \sum_{t=1}^d \lambda_t \left[P(\rho_t) - P_t \right], \\ &= \sum_{t=1}^d \text{Tr}(\rho_t H_t) + \lambda_t \left[P(\rho_t) - P_t \right], \end{aligned} \quad (3.6)$$

where $H_d = H + \sigma_d$, $H_t = \sigma_t - \mathcal{E}_{t+1}^\dagger(\sigma_{t+1})$ for $t \in \{1, 2 \dots d-1\}$ The dual function is obtained by minimizing the Lagrangian with respect to $\rho_1, \rho_2 \dots \rho_d \in \mathcal{S}$ i.e.

$$\begin{aligned} g(\vec{\sigma}, \vec{\lambda}) &= \min_{\rho_1, \rho_2 \dots \rho_d \in \mathcal{S}} \mathcal{L}(\vec{\rho}, \vec{\sigma}, \vec{\lambda}), \\ &= \sum_{t=1}^d \min_{\rho_t \in \mathcal{S}} \left[(\text{Tr}(\rho_t H_t) + \lambda_t P(\rho_t)) - \lambda_t P_t \right], \\ &= \sum_{t=1}^d \left(\mathcal{F}_{\mathcal{S}, P}(H_t, \lambda_t) - \lambda_t P_t \right) \end{aligned} \quad (3.7a)$$

where

$$\mathcal{F}_{\mathcal{S},P}(H, \lambda) = \min_{\rho \in \mathcal{S}} \left(\text{Tr}[H\rho] + \lambda P(\rho) \right). \quad (3.7b)$$

As with the single-qubit example, the dual function is a lower bound on the energy produced at the circuit output for any $\vec{\sigma}, \vec{\lambda} \geq 0$ i.e.

$$g(\vec{\sigma}, \vec{\lambda}) \leq \text{Tr}[\rho_d H] \quad \text{for all } \sigma_t \in \mathcal{M}((\mathbb{C}^2)^{\otimes N}), \lambda_t \geq 0.$$

The function $\mathcal{F}_{\mathcal{S},P}(H, \lambda)$ can be interpreted as a generalized free energy corresponding to the Hamiltonian H at temperature λ which depends on both the domain \mathcal{S} and the purity measure P . For instance, if the purity measure is taken to be the information content $I(\rho) = N - \text{Tr}[\rho \log_2(\rho)]$, then it reduces to the Gibbs free energy with an offset of $N\lambda$. However, by choosing different purity measures P as well as different domains \mathcal{S} , the dual function allows us to obtain a family of bounds on the noisy quantum circuit. As we will see in the next section, certain choices of P and \mathcal{S} provide lower bounds that can be classically computed.

Consider first the best lower bound that can be obtained from the dual function. In the following proposition, we show that the best lower bound attained by the dual function is exactly equal to the energy attained by the quantum circuit, and choice of dual variables $\sigma_1, \sigma_2 \dots \sigma_d$ that yields the largest value dual function corresponds to the Heisenberg picture evolution of the Hamiltonian H .

Proposition 1 *For the dual function defined in Eq. 3.7, it follows that its maximum over the dual variables is equal to the output energy of the noisy circuit i.e.*

$$\underset{\substack{\sigma_1, \sigma_2 \dots \sigma_d \in \mathcal{M}((\mathbb{C}^2)^{\otimes N}) \\ \lambda_1, \lambda_2 \dots \lambda_d \geq 0}}{\text{maximum}} g(\vec{\sigma}, \vec{\lambda}) = \text{Tr}[H \mathcal{E}_d \mathcal{E}_{d-1} \dots \mathcal{E}_1(\rho_0)],$$

and the maximum is attained at

$$\sigma_d = -H, \sigma_t = -\mathcal{E}_{t+1}^\dagger \mathcal{E}_{t+2}^\dagger \dots \mathcal{E}_d^\dagger(H),$$

and $\lambda_1 = \lambda_2 = \dots \lambda_d = 0$.

Proof: The proof of this proposition follows simply by noting that, from definition,

$$\mathcal{F}_{\mathcal{S},P}(0,0) = 0.$$

Now, if $\sigma_d = -H$, and $\sigma_t = -\mathcal{E}_{t+1}^\dagger \mathcal{E}_{t+2}^\dagger \dots \mathcal{E}_d^\dagger(H)$, then $H_t = 0$. Hence, we obtain that at this value of $\vec{\sigma}$ and at $\vec{\lambda} = 0$, $g(\vec{\sigma}, \vec{\lambda}) = \text{Tr}[\rho_0 \mathcal{E}_1^\dagger \mathcal{E}_2^\dagger \dots \mathcal{E}_d^\dagger(H)] = \text{Tr}[H \mathcal{E}_d \mathcal{E}_{d-1} \dots \mathcal{E}_1(\rho_0)]$. Since $\text{Tr}[H \mathcal{E}_d \mathcal{E}_{d-1} \dots \mathcal{E}_1(\rho_0)]$ is also an upper bound of $g(\vec{\sigma}, \vec{\lambda})$, the proposition follows. \square

This proposition establishes that finding the best dual bound is equivalent to exactly simulating the circuit, which we expect to be hard to do on classical computers. This hardness fundamentally stems from the fact that the dual variables $\sigma_1, \sigma_2 \dots \sigma_d$ are operators in an exponentially large space. However, since the dual function $g(\vec{\sigma}, \vec{\lambda})$ is a lower bound on the output energy for any $\vec{\sigma}, \vec{\lambda}$, a natural approach to evaluate a lower bound would be restrict σ_i to subsets of $\mathcal{M}((\mathbb{C}^2)^{\otimes N})$ where the dual function could be evaluated efficiently — the specific subset would depend on the choice of the purity measure. In Section 3.3, we will see that the dual function obtained on choosing the purity measure to be trace purity and the domain $\mathcal{S} = \mathcal{M}((\mathbb{C}^2)^{\otimes N})$ of N -qubit Hermitian operators can be evaluated efficiently if $\sigma_1, \sigma_2 \dots \sigma_d$ are chosen to be matrix product operators (MPOs) of bond-dimension $\text{poly}(N)$. In Section 3.4, we will consider the dual function obtained on choosing the purity measure to be the information content of the state, in which case $\sigma_1, \sigma_2 \dots \sigma_d$ can be restricted to the space of geometrically local Hamiltonians, allowing for an exact evaluation of the dual function.

Restricting the dual variables $\sigma_1, \sigma_2 \dots \sigma_d$ to a subset of $\mathcal{M}((\mathbb{C}^2)^{\otimes N})$ raises the question of whether the maximum value that the dual function can attain within this restricted set of dual variables gives a better lower bound on the energy compared to neglecting the circuit constraints and just accounting for the purity of the final state i.e. does the duality based bound still account for the circuit architecture. Our next proposition answers this question affirmatively, and shows that a better lower bound can be obtained as long as the restricted set of dual variables contains 0.

Proposition 2 Suppose $\mathcal{S}_\sigma \subset \mathcal{M}((\mathbb{C}^2)^{\otimes N})$, such that $0 \in \mathcal{S}_\sigma$, then

$$\underset{\substack{\sigma_1, \sigma_2, \dots, \sigma_d \in \mathcal{S}_\sigma \\ \lambda_1, \lambda_2, \dots, \lambda_d \geq 0}}{\text{maximum}} g(\vec{\sigma}, \vec{\lambda}) \geq \underset{\rho \in \mathcal{S}, P(\rho) \leq P_d}{\text{minimize}} \text{Tr}(H\rho)$$

Proof: Since $0 \in \mathcal{S}_\sigma$,

$$\underset{\lambda \geq 0}{\text{maximum}} g(\{0 \dots 0\}, \{0 \dots \lambda\}) \leq \underset{\substack{\sigma_1, \sigma_2, \dots, \sigma_d \in \mathcal{S}_\sigma \\ \lambda_1, \lambda_2, \dots, \lambda_d \geq 0}}{\text{maximum}} g(\vec{\sigma}, \vec{\lambda}).$$

Now, we can note that

$$g(\{0 \dots 0\}, \{0 \dots \lambda\}) = \mathcal{F}_{\mathcal{S}, P}(H, \lambda) - \lambda P_d.$$

It can be noted that $g(\{0 \dots 0\}, \{0 \dots \lambda\})$ is simply the dual function of the convex problem

$$\begin{aligned} & \underset{\rho \in \mathcal{S}}{\text{minimize}} \quad \text{Tr}(H\rho) \\ & \text{subject to} \quad P(\rho) \leq P_d. \end{aligned}$$

Furthermore, this convex problem trivially satisfies the Slater's conditions [111, 109]. This can be checked by noting that the Slater's conditions are satisfied if there is a $\rho \in \mathcal{S}$ such that $P(\rho) < P_d$ — this follows by noting that $P(I/2^N) < P_d$ and $I/2^N \in \mathcal{D}_1((\mathbb{C}^2)^{\otimes N}) \subseteq \mathcal{S}$. Since Slater's conditions are satisfied, this problem is strongly dual and consequently the optimal duality-bound is equal to the solution of the optimization problem i.e.

$$\underset{\lambda \geq 0}{\text{maximum}} g(\{0 \dots 0\}, \{0 \dots \lambda\}) = \underset{\rho \in \mathcal{S}, P(\rho) \leq P_d}{\text{minimize}} \text{Tr}(H\rho),$$

which proves the proposition. \square

While this proposition indicates that accounting for the circuit constraints while constructing the lower bound results in an improvement over only accounting for the final purity even with restricted space of dual variables, it says nothing about the extent

to which the bound improves. We expect the improvement to be strongly dependent on the purity function P , the domain set \mathcal{S} , and the dual set \mathcal{S}_σ used in formulating and evaluating the bound. In the next section, we consider a specific formulation of the dual function that uses the trace purity measure, and show that the lower bound obtained on accounting for the circuit constraints can be exponentially better than if the circuit constraints were not accounted for.

3.3 Trace purity-based lower bound

3.3.1 Formulation

In this section, we consider now a specific choice of the purity function and the domain \mathcal{S} that results in a dual function that can be computed exactly when the dual variables are parametrized as matrix product operators with poly(N) bond dimension. We choose the purity measure to be trace purity $P(\rho) = P_{\text{tr}}(\rho) = \text{Tr}(\rho^2)$, and the domain \mathcal{S} in Eq. 3.5 to be the space of Hermitian N -qubit operators $\mathcal{M}((\mathbb{C}^2)^{\otimes N})$. It then follows that $\mathcal{F}_{\mathcal{S},P}(H, \lambda)$ defined in Eq. 3.7b evaluates to

$$\mathcal{F}_{\mathcal{S},P}(H, \lambda) = -\frac{\text{Tr}(H^2)}{4\lambda},$$

and therefore, we obtain that

$$g(\vec{\sigma}, \vec{\lambda}) = -\text{Tr}[\rho_0 \mathcal{E}_1^\dagger(\sigma_1)] - \sum_{t=1}^d \left(\frac{\text{Tr}(H_t^2)}{4\lambda_t} + \lambda_t P_t \right),$$

where $H_d = H + \sigma_d$ and $H_t = \sigma_t - \mathcal{E}_{t+1}^\dagger(\sigma_{t+1})$. Furthermore, for this dual function, it is possible to perform the maximization over $\vec{\lambda}$ analytically to obtain

$$\begin{aligned} h(\vec{\sigma}) &= \underset{\vec{\lambda} \geq 0}{\text{maximum}} \quad g(\vec{\sigma}, \vec{\lambda}), \\ &= -\text{Tr}[\rho_0 \mathcal{E}_1^\dagger(\sigma_1)] - \sum_{i=1}^d \sqrt{P_i \text{Tr}(H_i^2)}. \end{aligned} \quad (3.8)$$

From the expression for $h(\vec{\sigma})$, we immediately notice that if $\sigma_1, \sigma_2 \dots \sigma_d$ are restricted to be matrix product operators with bond dimension D , then $h(\vec{\sigma})$ can be evaluated classically in time NdD^4 . However, as we established in proposition 1, the best lower bound is obtained $h(\vec{\sigma})$ when evaluating it at $\vec{\sigma}$ corresponding to a Heisenberg picture evolution of Hamiltonian H . While for most problems of interest (e.g. where H is a local or spatially-local Hamiltonian), H can be represented as a matrix product operator of a modest bond dimension, the unitaries involved in the circuit can, in general, grow its bond dimension exponentially. A natural choice of $\sigma_1, \sigma_2 \dots \sigma_d$ would then be to perform time-evolving block decimation (TEBD) [112, 113, 114, 115, 116] on the Heisenberg evolution and compress the operators in each step into bond-dimension D i.e. at $\vec{\sigma}^{h,D} = \{\sigma_1^{h,D}, \sigma_2^{h,D}, \dots, \sigma_d^{h,D}\}$

$$\begin{aligned} \sigma_d^{h,D} &= -H \text{ and,} \\ \sigma_t^{h,D} &= \Pi_D \mathcal{E}_{t+1}^\dagger(\sigma_{t+1}^{h,D}) \text{ for } t \in \{1, 2 \dots d-1\}, \end{aligned} \quad (3.9)$$

where Π_D compresses an N -qubit operator to an operator with a bond-dimension D [41].

Duality-bound and TEBD truncation errors. If a Heisenberg picture TEBD simulation, for some bond dimension D , of the noisy quantum circuit is exact, then by Proposition 1, the duality based bound $h(\vec{\sigma}^{h,D})$ is exactly equal to the expected energy at the output of the circuit. In practice, for small bond dimensions D , the TEBD algorithm is not exactly correct but incurs an error. However, as shown below, an upper bound on this error can also be efficiently computed for the TEBD algorithm. Consequently, tracking the error incurred in the TEBD algorithm allows us to calculate another lower bound on the output of the quantum circuit i.e. if the TEBD algorithm produces an estimate E_{TEBD} the output energy E of the circuit within an additive error δ , then $E_{\text{TEBD}} - \delta$ also lower bounds the energy E . A natural question to ask is if the duality based bounds are more informative than the bound obtained from just a TEBD simulation.

Consider now the problem of estimating the TEBD error following Ref. [113]. The

TEBD estimate of the energy at the circuit output, E_{TEBD} , can be expressed as

$$E_{\text{TEBD}} = \text{Tr} \left(\mathcal{E}_1(\rho_0) \left(\prod_{t=2}^d \Pi_D \mathcal{E}_t^\dagger \right) (H) \right),$$

while the true energy at the circuit output can be expressed as

$$E = \text{Tr} \left(\mathcal{E}_1(\rho_0) \left(\prod_{t=2}^d \mathcal{E}_t^\dagger \right) (H) \right).$$

Denoting by ρ_t the state of the qubits in the quantum circuit at time-step t , $\rho_t = \mathcal{E}_t \mathcal{E}_{t-1} \dots \mathcal{E}_1(\rho_0)$, we note that

$$\begin{aligned} E - E_{\text{TEBD}} &= \text{Tr} \left(\rho_1 \left(\prod_{t=2}^d \mathcal{E}_t^\dagger - \prod_{t=2}^d \Pi_D \mathcal{E}_t^\dagger \right) (H) \right), \\ &= \sum_{t=2}^d \text{Tr} \left(\rho_1 \left(\prod_{s=2}^{t-1} \mathcal{E}_s^\dagger \right) \left(\mathcal{E}_t^\dagger - \Pi_D \mathcal{E}_t^\dagger \right) \left(\prod_{s=t+1}^d \Pi_D \mathcal{E}_s^\dagger \right) (H) \right), \\ &= \sum_{t=2}^d \text{Tr} \left(\rho_{t-1} \left(\sigma_{t-1}^{h,D} - \mathcal{E}_t^\dagger(\sigma_t^{h,D}) \right) \right) = \sum_{t=1}^{d-1} \text{Tr}(\rho_t H_t), \end{aligned}$$

where, in the last step, we have used the fact that, by definition, $H_t = \sigma_{t-1}^{h,D} - \mathcal{E}_t^\dagger(\sigma_t^{h,D})$.

Now, an upper bound on the error $|E - E_{\text{TEBD}}|$ can be obtained via

$$|E - E_{\text{TEBD}}| \leq \sum_{t=1}^{d-1} |\text{Tr}(\rho_t H_t)| \leq \sum_{t=1}^{d-1} \|H_t\|_F, \quad (3.10)$$

where $\|A\|_F = \sqrt{\text{Tr}(A^\dagger A)}$ and we have used the fact that, by the Holder's inequality, $|\text{Tr}(\rho_t H_t)| \leq \|\rho_t\|_1 \|H_t\| \leq \|H_t\|_F$ since $\|\rho_t\|_1 = 1$ and $\|H_t\| \leq \|H_t\|_F$. We point out that an important reason why we express the error bound in terms of the Frobenius norm of H_t , instead of its operator norm, is because the Frobenius norm can be efficiently computed if H_t is a matrix product operator of a small bond dimension (which is the case while performing the TEBD simulation). The deviation bound in

Eq. 3.10 implies a lower bound

$$E \geq E_{\text{TEBD}} - \delta = -\text{Tr}[\rho_0 \mathcal{E}_1^\dagger(\sigma_1)] - \sum_{i=1}^d \sqrt{\text{Tr}(H_i^2)}. \quad (3.11)$$

This bound is significantly worse than the duality-based bound in Eq. 3.8 as $P_t \ll 1$ for all time steps t . The key reason why just accounting for a worst-case accumulation of TEBD errors yields a loose lower bound is that the upper bound in $|E - E_{\text{TEBD}}|$ *does not* account for the decrease in the trace purity of the quantum state in the presence of noise, which is explicitly factored into the formulation of the dual.

In Fig. 3.3, we numerically exhibit the difference between the bound in Eq. 3.11 and $h(\vec{\sigma}^{h,D})$ for a 1D circuit on $N = 40$ qubits [Fig. 3.3(a)], which is chosen to find the ground state of a commuting 1D Hamiltonian (see the figure caption for the exact circuit and Hamiltonian). As can be seen from Fig. 3.3(b), the lower bound computed from the trace purity based dual is significantly larger, and thus more representative of the impact of noise on the output energy, than the lower bound provided by Eq. 3.11. We point out that the dual variables $\vec{\sigma}^{h,D}$ obtained by TEBD in the Heisenberg picture are not necessarily the globally optimal choice in the space of all MPOs with bond dimension D to evaluate the dual function $h(\vec{\sigma})$. The function $h(\vec{\sigma})$ can potentially be optimized beyond the TEBD-based value to obtain better lower bounds. In practice, we observe that local optimization of $h(\vec{\sigma})$ with a gradient-based method starting from the initial point of $\vec{\sigma} = \vec{\sigma}^{h,D}$ yields only a modest improvement over $h(\vec{\sigma}^{h,D})$. Next, we study the improvement that the duality based bounds that account for the circuit constraint provide over bounds in existing literature that just account for the information content at the circuit output. In particular, we numerically compare the best lower bound ℓ_D^{dual} that we can obtain by evaluating $h(\vec{\sigma})$ at $\sigma_1, \sigma_2 \dots \sigma_d \in \text{MPO}_D$ (the space of all N -qubit MPOs of bond dimension D),

$$\ell_D^{\text{dual}} = \underset{\sigma_1, \sigma_2 \dots \sigma_d \in \text{MPO}_D}{\text{maximize}} h(\vec{\sigma}),$$

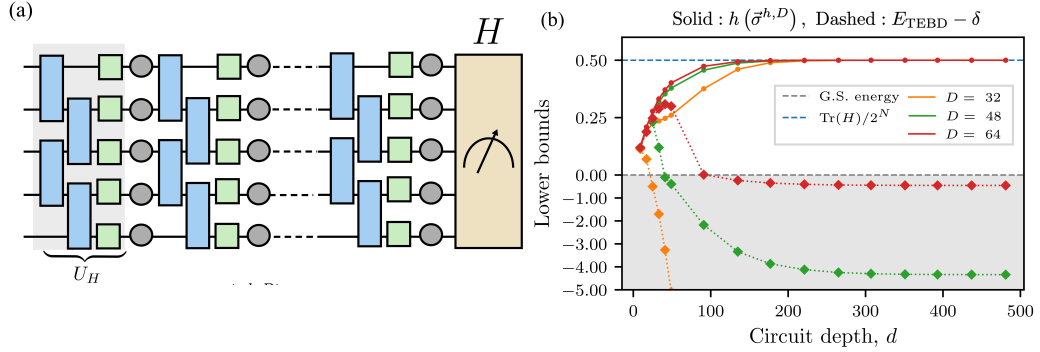


Figure 3.3: (a) Schematic of benchmark circuits considered for 1D spin systems: colored boxes indicate unitaries and grey circles depolarizing noise. Two-qubit unitaries are chosen to be $\exp(-i\theta X \otimes X)$ and single-qubit unitaries are independently Haar random. The Hamiltonian is chosen to be $H = -U_H(\sum_i Z_i)U_H^\dagger$, where U_H is the first layer of unitaries, making H a 4-local commuting Hamiltonian. The first layer of unitaries U_H thus transforms the initial state $|0\rangle^{\otimes N}$ into the ground state of H . The last $(d-1)/2$ layers are chosen to be the inverse of the previous $(d-1)/2$ layers — in the absence of noise, the output of the circuit is the ground state of H . (b) Plot shows trace purity-based dual bound ($h(\bar{\sigma}^{h,D})$ in Eq. 3.8) (solid lines, circular markers) and bound obtained by only considering the TEBD errors ($E_{\text{TEBD}} - \delta$ in Eq. 3.11) (dotted lines, diamond markers) for the ground state (G. S.) energy of the target Hamiltonian, as a function of circuit depth d for a system of $N = 40$ spins, with two-qubit gate parameter $\theta = 0.05$, depolarizing noise rate of $p = 3\%$ and varying MPO ansatz bond dimensions D . Grey dashed line indicates G.S. energy, grey shaded area indicates region of trivial bounds (less than G.S. energy), blue dashed line indicates energy of the completely mixed state $\mathbb{1}/2^N$. The y -axis is scaled by a constant multiplicative factor in the trivial region for visual clarity. The Hamiltonian is shifted and scaled such that its spectrum is in $[0, 1]$.

to the lower bound ℓ^I analyzed in Ref. [34],

$$\ell^I = \underset{\rho: I(\rho) \leq N(1-p)^d}{\text{minimize}} \text{Tr}(H\rho),$$

i.e. where they accounted only for the decreased information content $I(\rho) = N - \text{Tr}[\rho \log_2 \rho]$ of the final state as per Lemma 1. First, we show that there exists a Hamiltonian and a 1D circuit where ℓ_D^{dual} , with $D = O(N)$ [117], scales super-exponentially with the depth of the circuit and thus captures the propagation of errors through the

circuit, while ℓ^I scales at-most exponentially with the circuit depth.

Proposition 3 *There exists a 1D circuit and a N -qubit Hamiltonian H with $\text{Tr}(H) = 0$ and $\|H\| = N$, such that $\ell^I = -N(1-p)^{O(d)}$, while $\ell_D^{\text{dual}} = -N(1-p)^{\Omega(d^2)} + O(\sqrt{N})$ for a choice of $D \leq O(N)$.*

Proof sketch (see appendix D for details): Consider a Clifford circuit chosen at random from the ensemble of entangle-unentangle circuits analyzed in Ref. [106] — it was shown for this ensemble that, for a 1D circuit, on average, the energy of the output state with respect to a 2-local Hamiltonian converges to the energy of the maximally mixed state as $\sim \text{poly}(N) \times (1-p)^{\Omega(d^2)}$. Consider now the Hamiltonian $H = -\sum_{i=1}^N Z_i$ and initial state $|0\rangle^{\otimes N}$. In the Heisenberg picture, each Z_i will be mapped to exactly one Pauli string under the action of Clifford gates [118, 119]. Since a Pauli string is representable as an MPO of bond dimension 1, σ_t obtained from Heisenberg picture evolution will be a sum of N MPOs of bond-dimension 1 and will thus be a MPO of bond-dimension at most N . Thus, from Proposition 1, the purity-based dual exactly matches the energy of the output of the quantum circuit, which will scale as $-N(1-p)^{\Omega(d^2)}$ [106, 120]. As the bound without circuit constraints is agnostic to the unitaries in a circuit, it is also a lower bound on the circuit where all the unitaries are just the identity operation. For this trivial circuit, the energy of the state after d layers of just depolarizing noise scales as $-N(1-p)^d$. Hence, the lower bound without circuit constraints $\ell^I = -N(1-p)^{O(d)}$.

3.3.2 Numerical studies

For non-Clifford circuits, MPO parametrization with bond dimension $\text{poly}(N)$ is no longer expected to fully capture Heisenberg picture evolution. Even so, we numerically demonstrate for a 1D spin system that the circuit dual function Eq. 3.8 can be used to compute circuit-specific bounds that perform better than bounds that only take into account the information content of the output state. We compute the bounds by evaluating the dual function $h(\vec{\sigma})$ at the dual variables obtained from TEBD on the Heisenberg picture as in Eq. 3.9. Fig. 3.4 shows numerical studies of the bounds $h(\vec{\sigma}^{h,D})$ computed in this manner — we consider a 1D spin system of size $N = 40$ and

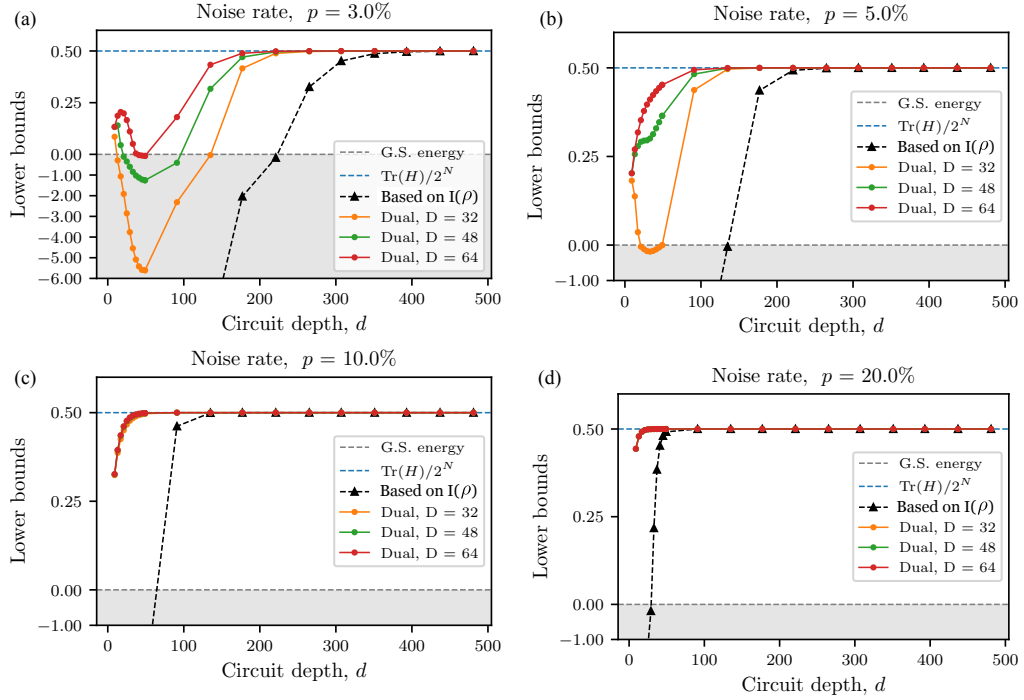


Figure 3.4: Comparison of the trace purity-based dual bound ($h(\bar{\sigma}^{h,D})$ in Eq. 3.8) and the bound based on just the information content of the output state ($\ell_{\lambda_c}^I$ in Eq. 3.13) for 1D many-body spin systems. Both bounds are lower bounds on the ground state (G. S.) energy of the same target Hamiltonian as considered for the results in Fig. 3.3. Plots show the bounds as a function of brick-wall quantum circuit depth d [Fig. 3.3(a)] for a system of $N = 40$ spins, varying MPO ansatz bond dimensions D , with depolarizing noise rates of (a) $p = 3\%$, (b) $p = 5\%$, (c) $p = 10\%$, and (d) $p = 20\%$. Two-qubit unitaries in the brick-wall circuit are chosen to be $\exp(-i\theta X \otimes X)$ with $\theta = 0.1$ and single-qubit unitaries are independently Haar random. Grey dashed line indicates G.S. energy, grey shaded area indicates region of trivial bounds (less than G.S. energy), blue dashed line indicates energy of the completely mixed state $\mathbb{1}/2^N$. The y -axis is scaled by a constant multiplicative factor in the trivial region for visual clarity. The Hamiltonian is shifted and scaled such that its spectrum is in $[0, 1]$.

circuits designed to prepare the ground state of a commuting local Hamiltonian (see figure caption for details). The plots in Fig. 3.4 show the bounds for MPO ansatzes with different bond dimensions D plotted against the circuit depth d for circuits with noise rates $p = 3\%$ [Fig. 3.4(a)], $p = 5\%$ [Fig. 3.4(b)], $p = 10\%$ [Fig. 3.4(c)], and $p = 20\%$ [Fig. 3.4(d)]. However, for the lowest noise rate $p = 3\%$, the circuit dual

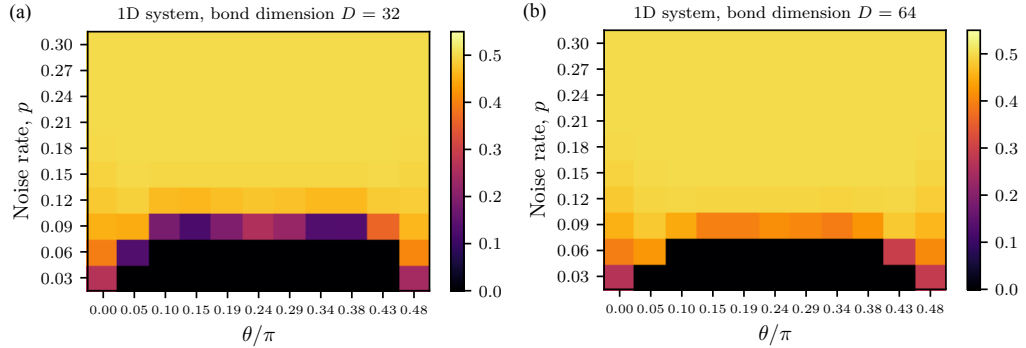


Figure 3.5: Trace purity-based dual bounds ($h(\bar{\sigma}^{h,D})$ in Eq. 3.8) for a 1D system of $N = 32$ spins, the same target Hamiltonian as considered for the results in Fig. 3.3 (see description of Hamiltonian in caption of Fig. 3.3), and brick-wall quantum circuits [Fig. 3.3(a)] where two-qubit unitaries are chosen to be $\exp(-i\theta X \otimes X)$ and single-qubit unitaries are independently Haar random. Plots show dual bounds as a function of noise rate p and circuit parameter θ for circuit depth $d = 25$ and bond dimensions (a) $D = 32$ and (b) $D = 64$. The Hamiltonian is shifted and scaled such that its spectrum is in $[0, 1]$.

bounds at intermediate depths are trivial i.e. lower than the ground state energy of H — this can be attributed to the fact that the intermediate depth regime is the regime where the MPO ansatz is least representative. For shorter depths, the bond dimension of the Heisenberg picture operator would have not grown very much while for very long depths, the action of the depolarizing noise reduces the bond dimension of the Heisenberg picture operator.

Figure 3.4 also compares the trace purity-based dual bound to the information content-based bound. However, since the duality-based bound is exactly computable on a classical computer, to make a fair comparison we need to use a certifiable method for computing the information-content based bound. In particular, using Lagrangian duality, the information content-based bound can be reframed in terms of the Gibbs free energy of the problem Hamiltonian i.e.

$$\begin{aligned}
 \ell^I &= \underset{\rho: I(\rho) \leq N(1-p)^d}{\text{minimize}} \text{Tr}(H\rho) \\
 &= \underset{\lambda \geq 0}{\text{maximize}} \lambda S_d + G(H, \lambda),
 \end{aligned} \tag{3.12}$$

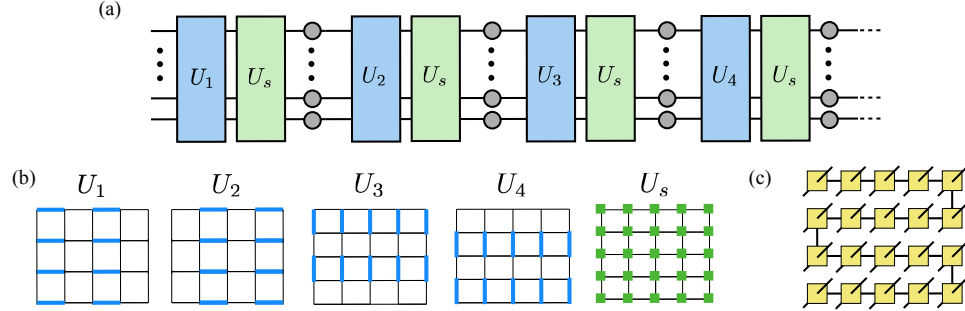


Figure 3.6: (a) Schematic of quantum circuits considered for 2D spin systems on a square lattice: colored boxes indicate unitaries and grey circles depolarizing noise. Each unitary layer consists of two-qubit unitaries $\exp(-i\theta X \otimes X)$ (blue boxes) followed by independently Haar random single-qubit unitaries (green boxes). The first $d/2$ layers serve to increase the entanglement in the state. The remaining layers invert the action of the previous $d/2$ such that, in the absence of noise, the output of the circuit is the ground state of $H = -\sum_{\langle i,j \rangle} Z_i Z_j$ where Z_i is the Pauli- Z operator for the i^{th} spin and $\langle i,j \rangle$ indicates nearest-neighbors. (b) Circuits considered have a brick-wall structure: two-qubit unitary layers cycle between gates on odd horizontal edges (U_1), even horizontal edges (U_2), odd vertical edges (U_3), and even vertical edges (U_4). Single-qubit gates (U_s) are applied on every qubit after every two-qubit gate layer. (c) Structure of the MPO considered for 2D spin systems: yellow squares indicate tensors at each site in the 2D lattice and lines emerging from them indicate tensor indices. Horizontal lines indicate bond indices with dimension D and diagonal lines indicate physical indices.

where $S_d = N - N(1-p)^d$ and $G(H, \lambda) = -\lambda \log \text{Tr} \exp(-H/\lambda)$ is the Gibbs free energy of H at temperature λ . However, since H is generally a many-body Hamiltonian, an accurate evaluation of $G(H, \lambda)$ can only be guaranteed at sufficiently high temperatures [121]. Thus, instead of evaluating the bound ℓ^I in Eq. 3.12, we introduce a lower bound λ_c on the temperature λ and evaluate

$$\ell_{\lambda_c}^I = \underset{\lambda \geq \lambda_c}{\text{maximize}} \lambda S_d + G(H, \lambda), \quad (3.13)$$

For spatially local Hamiltonians, λ_c can be chosen depending on the norms of the local terms in the Hamiltonian, the dimensionality of the lattice, and the interaction range. In our calculations, we make the choice of $\lambda_c = 8e^3$ — this is based on Ref. [121]

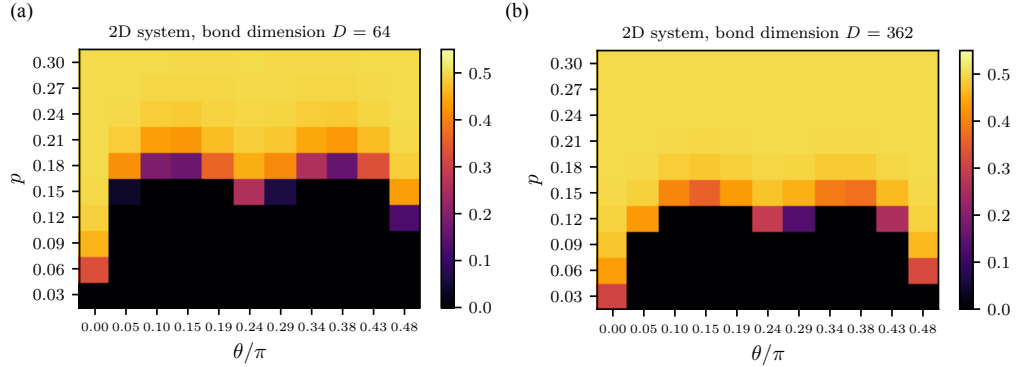


Figure 3.7: Trace purity-based dual bounds ($h(\vec{\sigma}^{h,D})$ in Eq. 3.8) for the ground state energy of the target Hamiltonian H as a function of noise rate p and circuit parameter θ for a system of $N = 36$ spins arranged in a 6×6 lattice, circuit depth $d = 32$ and MPO bond dimensions (a) $D = 64$ and (b) $D = 362$. The Hamiltonian is shifted and scaled such that its spectrum is in $[0, 1]$.

which, to the best of our knowledge, provides the only rigorous algorithm that works for evaluating $G(H, \lambda)$ at temperatures above λ_c .

We see from Fig. 3.4 that the dual provides a tighter lower bound on the output than the bound based on just the information content of the output state. The information content-based bounds shown in Fig. 3.4 are also trivial (i.e. lower than the ground-state energy) for intermediate *and* short depths — this is due to the temperature lower bound that needs to be introduced to ensure computability of the Gibbs free energy. We also observe that the separation between the information content-based and circuit dual bounds increases with the bond dimension D as the MPO ansatz becomes more expressive with increasing bond dimension. In the limit of large circuit depth at non-zero depolarizing noise rates, the state of the circuit approaches the completely mixed state, and we observe that both bounds also approach the energy corresponding to the completely mixed state.

Finally, we demonstrate that the dual bounds are able to capture the extent of entanglement being generated in a circuit. In the brick-wall quantum circuits we consider, the two-qubit gates in the circuit $\exp(-i\theta X \otimes X)$ are parametrized by an angle θ which controls the entanglement being produced — for example, at $\theta = 0, \pi/2$, there is no entanglement at all. Fig. 3.5 shows the bounds as a function of the angular

parameter θ and the noise rate p , for constant bond dimensions D and circuit depths d , for a 1D system of $N = 32$ spins and Fig. 3.7 shows the same for a 2D system of $N = 36$ spins in a 6×6 lattice. For the 2D system, we consider the MPO ansatz to have a ‘snake-like’ bond structure on the 2D lattice [Fig. 3.6] — such a snake-like structure is a numerically convenient approach for performing TEBD for 2D systems. This ansatz is useful for moderate system sizes but due to gates along the vertical edges of the lattice the bond dimension required grows rapidly. For larger system sizes, we expect that a tensor network ansatz that matches the architecture of the circuit [122, 123, 124] would give better bounds. For both the 1D and 2D systems, the target Hamiltonians are shifted and scaled such that the ground state energies are zero and any bounds lower than zero are considered trivial and represented as zero in the plots — the black regions in the plots thus correspond to trivial bounds. We observe that, near $\theta = 0, \pi/2$, where the entanglement is small, the MPO ansatz of constant bond dimension used for the bounds is able to capture it and we obtain non-trivial bounds for small noise rates $p \approx 6\%$. For values of θ away from these limits, the region of triviality is larger but non-trivial dual bounds can still be obtained for higher noise rates.

3.4 Using duality with information content

In the previous sections, we have investigated the impact of noise using the trace purity as a measure of the mixedness in the noisy circuit. The trace purity-based dual function Eq. 3.8 contains terms with Frobenius norms $\sqrt{\text{Tr}(H_t^2)}$ which, in the worst case, could grow exponentially with the system size N . Hence, the trace purity-based dual tends to become trivial in the limit of large system size and intermediate circuit depths. An alternative better conditioned purity measure is the information content based on the Von-Neumann entropy, $I(\rho) = N - S(\rho) = N + \text{Tr}(\rho \log_2(\rho))$. In this section, we formulate a duality-based bound using the information content as a purity measure. However, as we illustrate below, the duality bound here is harder to compute than the one based on trace-purity for general spin model — to still gauge the efficacy of this bound, we numerically study in the simpler but physically

relevant case of Gaussian fermions. While our results are suggestive that using the information-content based bounds could be useful for spin models, the associated dual function is harder to compute classically — we leave it as an open problem to develop classical algorithms to compute informative bounds using this strategy for spin models.

Considering the information content, the free energy defined in Eq. 3.7b becomes the Gibbs free energy with an offset,

$$\begin{aligned} \mathcal{F}_{S,P}(H, \lambda) &= \inf_{\rho \succeq 0, \text{Tr}(\rho)=1} \left(\text{Tr}[H\rho] + \lambda I(\rho) \right), \\ &= N\lambda + \inf_{\rho \succeq 0, \text{Tr}(\rho)=1} \left(\text{Tr}(H\rho) - \lambda S(\rho) \right), \\ &= N\lambda - \lambda \log \text{Tr} \exp(-H/\lambda), \end{aligned} \quad (3.14)$$

which together with Eq. 3.7 yields,

$$\begin{aligned} \tilde{g}(\vec{\sigma}, \vec{\lambda}) &= -\text{Tr}[\rho_0 \mathcal{E}_1^\dagger(\sigma_1)] \\ &\quad + \sum_{t=1}^d \left(-\lambda_t \log \text{Tr} \exp(-H_t/\lambda_t) + \lambda_t(N - I_t) \right), \end{aligned} \quad (3.15)$$

where $I_t = N(1 - p)^t$ is the analytical bound on the information content under depolarizing noise defined in Lemma 1.

To benchmark the performance of the information content-based dual, we consider Gaussian fermionic systems where the dual function Eq. 3.15 can be computed exactly. We study N fermions arranged on a lattice and choose H to be a quadratic Hamiltonian,

$$H = i \sum_{\alpha, \alpha', x, x'} h_{x, x'}^{\alpha, \alpha'} c_x^\alpha c_{x'}^{\alpha'},$$

where c_x^1, c_x^2 are the Majorana operators for the fermion at point x on the lattice, and $h_{x, x'}^{\alpha, \alpha'}$ are real numbers specifying H . We additionally assume the unitaries in the circuit that prepares the ground state of H from an initial vacuum state to be Gaussian unitaries.

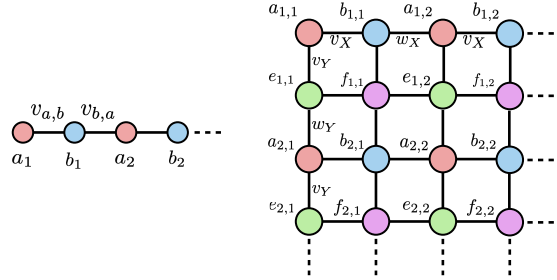


Figure 3.8: Schematic of SSH model quadratic fermionic Hamiltonians with alternating hopping strengths in 1D and 2D.

Since both Gaussian unitaries and the depolarizing channel map a quadratic Hermitian operator to another quadratic Hermitian operator, Proposition 1 indicates that the dual function is maximized for σ_t which themselves are quadratic Hermitian operators. This motivates the following ansatz for σ_t

$$\sigma_t = i \sum_{\substack{\alpha, \alpha', x, x' \\ d(x, x') \leq r}} s_{x, x'; t}^{\alpha, \alpha'} c_x^\alpha c_{x'}^{\alpha'},$$

for real $s_{x, x'; t}^{\alpha, \alpha'}$. In our study, we restrict σ_t to be local operators with interaction range r while maximizing $g(\vec{\sigma}, \vec{\lambda})$ to obtain the lower bound — when $r \sim$ lattice size, we expect to obtain the best possible lower bound but since the ansatz always includes the point $\vec{\sigma} = 0$, we expect from Proposition 2 to obtain a bound better than that predicted by only considering the information content of the output state, even for small r . Choosing σ_t to be quadratic Hermitian operators allows for exact, classically efficient computation of the Gibbs free energy terms in the dual function and, furthermore, even the circuit output can be computed exactly by considering the covariance matrix describing the state — see appendix B for details. We obtain bounds by maximizing $g(\vec{\sigma}, \vec{\lambda})$ through a gradient-based local optimization algorithm (L-BFGS-B), starting from the initial point where σ_t are chosen to be the Heisenberg picture evolution of $-H$, but projected on to the space of quadratic fermionic Hamiltonians with interaction range r after each time step — much like the compression into MPOs of bond dimension D in Eq. 3.9.

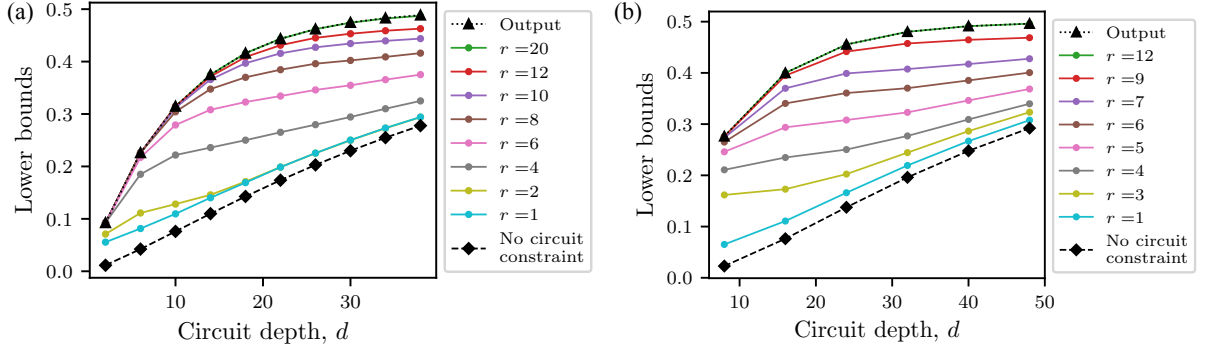


Figure 3.9: Comparison of information content-based dual bounds with and without circuit constraints, and the output energies of noisy Gaussian circuits for systems consisting of (a) $N = 48$ fermions arranged in a 1D lattice, (b) $N = 49$ fermions arranged in a 7×7 2D lattice. Dual bounds are shown for ansatzes with varying interaction range r . The horizontal axis represents the depth d of a Gaussian brick-wall circuit that outputs the ground state of the SSH model. Fermions are independently subject to depolarizing noise with probability $p = 5\%$ after every unitary layer. The Hamiltonians are shifted and scaled such that their spectrum is in $[0, 1]$.

Figure 3.9 shows a numerical study of the bounds that we obtain — we consider systems with ~ 50 fermions arranged both on 1D [Fig. 3.9(a)] and 2D lattices [Fig. 3.9(b)] and experiencing depolarizing noise at a rate of 5%. H is chosen to be a SSH model, nearest neighbor Hamiltonian with alternating hopping strengths [Fig. 3.8]. For the 1D benchmarks, we choose

$$H = \sum_x \left(v_{a,b} a_x^\dagger b_x + v_{b,a} b_x^\dagger a_{x+1} + \text{h.c.} \right), \quad (3.16a)$$

and for 2D benchmarks, we choose

$$H = \sum_{x,y} \left(\sum_{\substack{p,q \in \\ \{(a,b),(e,f)\}}} \left(v_{p,q} p_{x,y}^\dagger q_{x,y} + v_{q,p} q_{x,y}^\dagger p_{x+1,y} + \text{h.c.} \right) \right. \\ \left. + \sum_{\substack{p,q \in \\ \{(a,e),(b,f)\}}} \left(v_{p,q} p_{x,y}^\dagger q_{x,y} + v_{q,p} q_{x,y}^\dagger p_{x,y+1} + \text{h.c.} \right) \right), \quad (3.16b)$$

where we choose $v_{a,b} = v_{ef} = v_x$, $v_{b,a} = v_{f,e} = w_x$, $v_{a,e} = v_{b,f} = v_y$ and $v_{e,a} = v_{f,b} = w_y$. For the numerical studies shown in Fig. 3.9, H is shifted and scaled such that the ground and highest excited state energies are zero and one, respectively. We consider circuits of depth d consisting of two-mode Gaussian unitaries arranged in a brick-wall layout, where the first $d/2$ layers are composed of randomly generated two-mode Gaussian unitaries that serve to increase the entanglement in the state. The remaining layers invert the action of the previous $d/2$ such that, in the absence of noise, the output state is the initial state, which is chosen to be the ground state of H . In Fig. 3.9, for comparison, we also include the exact output of the noisy Gaussian circuit, as well as the bound obtained by neglecting the circuit constraints and only considering the information content of the output state. As expected, we find that on accounting for the circuit constraint, we obtain bounds that are more representative of the output. We also observe that the dual bounds get closer to the output as the dual ansatz's interaction range r increases, since the ansatz becomes more expressive.

3.5 Conclusion

We demonstrated a method to rigorously lower bound the performance of any given quantum circuit subject to a constant rate of depolarizing noise. We achieved this by constructing a Lagrangian dual specific to the circuit, which takes into consideration not only the decreasing purity of the state through the circuit due to noise, but also the details of the gates in the circuit, allowing the study of the effect of entanglement generation in the circuit that can worsen the detrimental effects of noise. We presented numerical studies in spin systems and showed that it is possible to efficiently calculate circuit-specific lower bounds that are tighter than bounds obtained by just considering the information content of the output state. We provided an interpretation of the trace purity-based dual evaluated at dual variables obtained from time-evolving block decimation (TEBD) in the Heisenberg picture in terms of the compression errors. We showed that the dual can be formulated in terms of the information content instead of trace purity — we computed information content-based circuit dual bounds for Gaussian fermionic systems where the Gibbs free energy can be computed exactly.

Chapter 4

Point-coupling Hamiltonian for frequency-independent linear optical devices

We propose a Hamiltonian that can model an arbitrary frequency-independent linear optical device acting on propagating optical modes. The Hamiltonian assumes that the optical modes couple to each other at a single-point in space — we therefore call it the *point-coupling Hamiltonian*. For a given frequency-independent classical scattering matrix implemented by the linear optical device, we provide a recipe to construct a point-coupling Hamiltonian describing the device. We formally integrate the Heisenberg equations of motion for the point-coupling Hamiltonian, and use the resulting solution to calculate its quantum scattering matrix [125, 126, 127]. It is shown that an application of the quantum scattering matrix on an incoming quantum state is equivalent to applying the inverse of the classical scattering matrix on the annihilation operators of the optical modes in the incoming quantum state, thereby reproducing the commonly used procedure for analyzing the quantum physics of linear-optical devices. We also ‘diagonalize’ the point-coupling Hamiltonian to calculate its normal modes — this provides a connection between the Hamiltonian presented and the quantization approach described in Ref. [128]

Finally, in order to demonstrate the utility of the point-coupling Hamiltonian proposed, we use it to rigorously derive and implement a matrix-product-state (MPS) [129, 42] based update to simulate time-delayed feedback systems with linear optical devices providing feedback [39, 40]. Time-delayed feedback systems typically have a low-dimensional quantum system, such as a two-level system, coupling to a well-defined optical mode and the emission from the quantum system is used to re-excite the quantum system via a feedback path. The feedback path can be constructed using a linear-optical device such as a mirror, or using another quantum system. Time-delayed feedback systems possibly provide a platform for generation of highly entangled states for quantum computation [130, 131], quantum simulation [132] as well as implementation of quantum memories using long-lived bound states [133]. MPS based simulations of such systems were proposed in Ref. [39], although the formulation relied on hard boundary conditions e.g. it assumed that the feedback to the quantum system was provided by an ideal mirror. Using the point-coupling Hamiltonian, we outline a method to extend the MPS based simulation of this system to account for the situation wherein the mirror is described by a scattering matrix, and thus enable an analysis of the impact of non-ideality in the mirror on the dynamics of the feedback-system. We expect the point-coupling Hamiltonian proposed to be of utility in analyzing quantum systems with complicated linear optical devices that can only be described by a full scattering matrix, and cannot be well-approximated by hard boundary conditions.

4.1 Point-coupling Hamiltonian

4.1.1 Dynamics in the Heisenberg picture

Consider N propagating optical modes (which can physically be waveguide modes, or collimated optical beams) interacting with each other through a linear-optical device (Fig. 4.1). Note that optical modes that are identical but for the direction of propagation are counted as separate modes. Labelling by $a_n(\omega)$ the annihilation

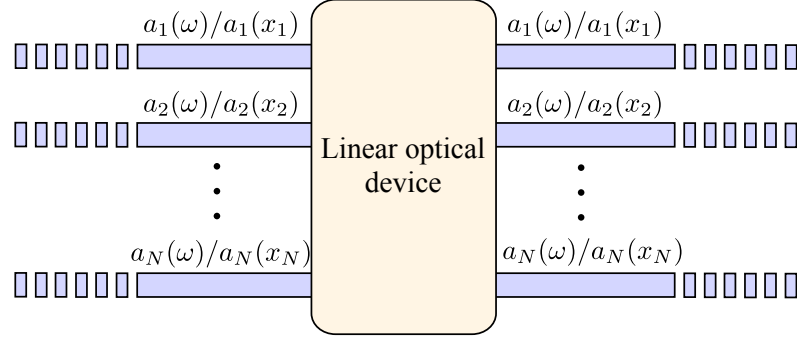


Figure 4.1: Schematic of a linear optical device acting on N optical modes. The frequency-domain and position-domain annihilation operator for the n^{th} optical mode are denoted by $a_n(\omega)$ and $a_n(x_n)$ respectively where x_n is the position of the point under consideration in the coordinate system attached to the n^{th} optical mode (note that we each optical mode to, in general, have its own independent coordinate system with the linear optical device being at $x_n = x_n^0$ in the coordinate system of the n^{th} optical mode.).

operator of the n^{th} optical mode at frequency ω , we propose the following Hamiltonian for describing the dynamics of the system:

$$H = \sum_{n=1}^N \int_{-\infty}^{\infty} \omega a_n^\dagger(\omega) a_n(\omega) d\omega + \sum_{n=1}^N \sum_{m=1}^N V_{n,m} a_n^\dagger(x_n^0) a_m(x_m^0), \quad (4.1)$$

where $a_n(x_n)$ is the position-domain annihilation operator for the n^{th} optical mode at coordinate x_n along its direction of propagation:

$$a_n(x_n) = \int_{-\infty}^{\infty} a_n(\omega) e^{i\omega x_n} \frac{d\omega}{\sqrt{2\pi}}. \quad (4.2)$$

Here the position x_n is expressed in units of time such that the group velocity, assumed to be frequency independent and uniform across all the optical modes, is unity. The coordinate of the linear-optical device along the direction of propagation of the n^{th} optical mode is x_n^0 . Note that we allow for the coordinate x_n for different optical modes to be expressed in different coordinate systems — in general, each optical mode can have its own coordinate system with the x axis of the coordinate system being along its direction of propagation. For e.g. the x axis for a forward propagating mode will

be in a direction opposite to the x axis for a backward propagating mode, or modes waveguides oriented in physically different directions will have differently oriented coordinate systems. We note that $a_n(\omega)$, and consequently $a_n(x_n)$, satisfy the usual bosonic commutation relations: $[a_n(\omega), a_m^\dagger(\omega')] = \delta_{n,m}\delta(\omega - \omega')$, $[a_n(\omega), a_m(\omega')] = 0$, $[a_n(x_n), a_m^\dagger(x'_m)] = \delta_{n,m}\delta(x_n - x'_m)$ and $[a_n(x_n), a_m(x'_m)] = 0$. Moreover, as a consequence of the Hermiticity of H , the coupling coefficients $V_{k,m}$ satisfy $V_{n,m} = V_{m,n}^*$.

The dynamics of this Hamiltonian can be easily analyzed using the Heisenberg's equations of motion, which are given by:

$$i\frac{da_n(\omega; t)}{dt} = \omega a_n(\omega; t) + \sum_{m=1}^N \frac{V_{n,m}}{\sqrt{2\pi}} a_m(x_m^0; t) e^{-i\omega x_n^0} \quad \forall n \in \{1, 2, \dots, N\}. \quad (4.3)$$

As is shown in appendix E, these equations can easily be integrated to relate the position-domain annihilation operators at time $t = t_0 + \tau$ and displaced by a distance $x \in (-\infty, \infty)$ from the linear optical device to the position-domain annihilation operators at time $t = t_0$:

$$\begin{bmatrix} a_1(x_1^0 + x; t_0 + \tau) \\ a_2(x_2^0 + x; t_0 + \tau) \\ \vdots \\ a_N(x_N^0 + x; t_0 + \tau) \end{bmatrix} = \left[\mathbf{I} - i\mathbf{V} \left(\mathbf{I} + \frac{i\mathbf{V}}{2} \right)^{-1} \Theta(0 \leq y \leq \tau) \right] \begin{bmatrix} a_1(x_1^0 + x - \tau; t_0) \\ a_2(x_2^0 + x - \tau; t_0) \\ \vdots \\ a_N(x_N^0 + x - \tau; t_0) \end{bmatrix}, \quad (4.4)$$

where \mathbf{V} is a $N \times N$ Hermitian matrix formed by $V_{m,n}$ as its elements, \mathbf{I} is the identity matrix of size N and $\Theta(x_1 \leq x \leq x_2)$ is defined by:

$$\Theta(x_1 \leq x \leq x_2) = \begin{cases} 1 & \text{if } x \in (x_1, x_2) \\ 0 & \text{if } x \in (-\infty, x_1) \cup (x_2, \infty) \\ \frac{1}{2} & \text{if } x \in \{x_1, x_2\} \end{cases}. \quad (4.5)$$

To intuitively interpret the result in Eq. 4.4, note that if $y < 0$, then the position-domain annihilation operator at $t = t_0 + \tau$ is simply a propagated version of itself at $t = t_0$. This is simply a consequence of the physical points described by $x < 0$ lying before the linear optical device along the propagation direction, and consequently being unaffected by scattering from the linear-optical device. This situation is the same for $x > \tau$, since the scattered light from the linear-optical device has not had sufficient time to propagate to the points in question from the location of the linear optical device (i.e. from $x = 0$). For $0 < x < \tau$, the optical mode annihilation operator at $t = t_0 + \tau$ is a sum of a propagated version of itself and contributions from other optical modes as scattered by the linear optical device, and Eq. 4.4 can be simplified to:

$$\begin{bmatrix} a_1(x_1^0 + x; t_0 + \tau) \\ a_2(x_2^0 + x; t_0 + \tau) \\ \vdots \\ a_N(x_N^0 + x; t_0 + \tau) \end{bmatrix} = \mathbf{S} \begin{bmatrix} a_1(x_1^0 + x - \tau; t_0) \\ a_2(x_2^0 + x - \tau; t_0) \\ \vdots \\ a_N(x_N^0 + x - \tau; t_0) \end{bmatrix}, \quad (4.6)$$

where

$$\mathbf{S} = \mathbf{I} - i\mathbf{V} \left(\mathbf{I} + \frac{i\mathbf{V}}{2} \right)^{-1} = \left(\mathbf{I} - \frac{i\mathbf{V}}{2} \right) \left(\mathbf{I} + \frac{i\mathbf{V}}{2} \right)^{-1}. \quad (4.7)$$

Since \mathbf{S} relates the optical mode annihilation operators before and after scattering from the linear optical-device has occurred, it can be interpreted as the classical scattering matrix corresponding to the linear optical-device. It can readily be verified that a consequence of \mathbf{V} being Hermitian is that the matrix \mathbf{S} is unitary. Moreover, if \mathbf{S} has the diagonalization $\mathbf{S} = \mathbf{U} \text{diag}[e^{i\phi}] \mathbf{U}^\dagger$, it follows from Eq. 4.7 that:

$$\mathbf{V} = -\mathbf{U} \text{diag} \left[2 \tan \left(\frac{\phi}{2} \right) \right] \mathbf{U}^\dagger. \quad (4.8)$$

Therefore, given the classical matrix \mathbf{S} of a linear-optical device, Eq. 4.8 allows us to construct the matrix \mathbf{V} and by extension the point-coupling Hamiltonian that can model the device. As examples, we consider some commonly used linear optical

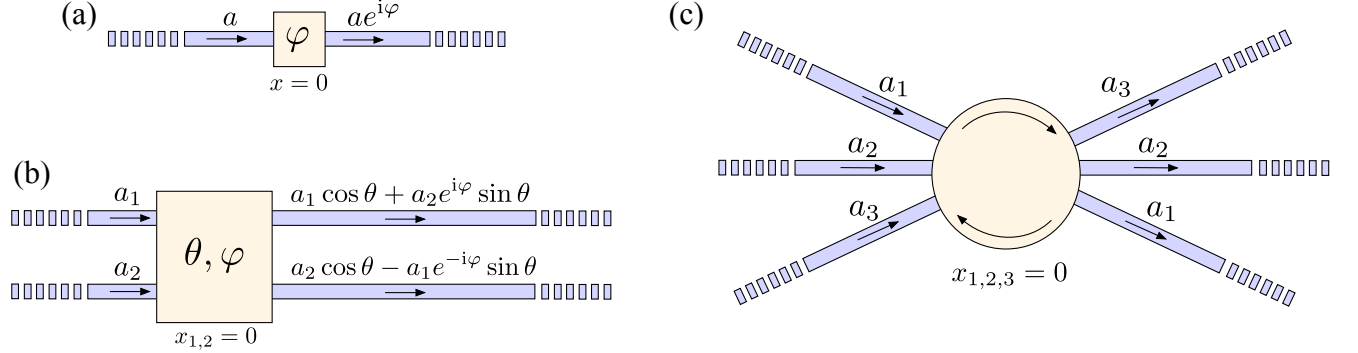


Figure 4.2: Schematic figures showing the action of (a) phase-shifter with imparted phase φ acting on a optical mode denoted by a , (b) beam-splitter with parameters (θ, φ) acting on optical modes denoted by a_1 and a_2 and (c) an optical circulator designed acting on optical modes a_1 , a_2 and a_3 . The relationship between the input and output signals of the linear-optical device are also shown in the diagrams.

devices (Fig. 4.2) and construct the point-coupling Hamiltonians that describe their dynamics:

- (a) *Phase shifter*: The classical scattering matrix \mathbf{S} of the phase-shifter [Fig. 4.2(a)] is a single-element matrix: $\mathbf{S} = [e^{i\varphi}]$. From Eq. 4.8, we obtain $\mathbf{V} = [-2 \tan(\varphi/2)]$. The Hamiltonian for the phase shifter can thus be written as:

$$H_{\text{phase-shifter}} = \int_{-\infty}^{\infty} \omega a^\dagger(\omega) a(\omega) d\omega - 2 \tan\left(\frac{\varphi}{2}\right) a^\dagger(x=0) a(x=0), \quad (4.9)$$

where $a(\omega)$ [$a(x)$] is the frequency-domain (position-domain) annihilation operator for the optical mode that the phase-shifter is acting on.

- (b) *Beam-splitter*: The beam-splitter [Fig. 4.2(b)] is described by the following classical scattering matrix:

$$\mathbf{S} = \begin{bmatrix} \cos \theta & \sin \theta e^{i\varphi} \\ -\sin \theta e^{-i\varphi} & \cos \theta \end{bmatrix}. \quad (4.10)$$

Again, using Eq. 4.8, we obtain

$$\mathbf{V} = \begin{bmatrix} 0 & 2i \tan(\theta/2) e^{i\varphi} \\ -2i \tan(\theta/2) e^{-i\varphi} & 0 \end{bmatrix}, \quad (4.11)$$

from which we can construct the beam splitter Hamiltonian:

$$H_{\text{beam-splitter}} = \sum_{k \in \{1,2\}} \int_{-\infty}^{\infty} \omega a_k^\dagger(\omega) a_k(\omega) d\omega + \left[2i \tan\left(\frac{\theta}{2}\right) e^{i\varphi} a_1^\dagger(x_1=0) a_2(x_2=0) + \text{h.c.} \right], \quad (4.12)$$

where $a_{1,2}(\omega)$ [$a_{1,2}(x_{1,2})$] are the frequency-domain (position-domain) annihilation operators for the optical modes that the beam-splitter is acting on.

- (c) *Optical circulator*: The optical circulator [Fig. 4.2(c)] routes an excitation in optical mode 1 to optical mode 2, optical mode 2 to optical mode 3 and optical mode 3 to optical mode 1. It can thus be described by the following 3×3 classical scattering matrix:

$$\mathbf{S} = \begin{bmatrix} 0 & 1 & 0 \\ 0 & 0 & 1 \\ 1 & 0 & 0 \end{bmatrix}, \quad (4.13)$$

and therefore

$$\mathbf{V} = \begin{bmatrix} 0 & 2i & -2i \\ -2i & 0 & 2i \\ 2i & -2i & 0 \end{bmatrix}, \quad (4.14)$$

from which we can construct the optical circulator Hamiltonian:

$$\begin{aligned}
 H_{\text{circulator}} = & \sum_{k \in \{1,2,3\}} \int_{-\infty}^{\infty} \omega a_k^\dagger(\omega) a_k(\omega) d\omega \\
 & + \left[\sum_{k \in \{1,2,3\}} 2i a_k^\dagger(x_k = 0) a_{k+1}(x_{k+1} = 0) + \text{h.c.} \right], \quad (4.15)
 \end{aligned}$$

where $a_{1,2,3}(\omega)$ [$a_{1,2,3}(x_{1,2,3})$] are the frequency-domain (position-domain) annihilation operators for the optical modes that the optical circulator acts on, and $a_4(\omega)/a_4(x_4)$ is to be interpreted as $a_1(\omega)/a_1(x_1)$.

4.1.2 Quantum scattering matrix of the point-coupling Hamiltonian

While the previous subsection analyzed the point-coupling Hamiltonian in the Heisenberg picture, in this subsection we analyze its dynamics in the Schrodinger picture. In particular, we consider the problem of exciting the linear-optical device with an input state, and attempt to calculate the output state produced by the device.

The key object relating the input state (assumed to be the asymptote [134] to the system at $t \rightarrow -\infty$) of the system to its output state (assumed to be the asymptote [134] to the state of the system at $t \rightarrow \infty$) is the quantum [134]:

$$\mathcal{S} = \lim_{\substack{t_+ \rightarrow \infty \\ t_- \rightarrow -\infty}} e^{iH_0 t_+} e^{-iH(t_+ - t_-)} e^{-iH_0 t_-}, \quad (4.16)$$

where H_0 is the Hamiltonian of the optical modes without accounting for the linear-optical device:

$$H_0 = \sum_{k=1}^N \int_{-\infty}^{\infty} \omega a_k^\dagger(\omega) a_k(\omega) d\omega. \quad (4.17)$$

Consider now the computation of the following K photon matrix element of the scattering matrix ($\mathbf{x} \equiv \{x_1, x_2 \dots x_K\}$, $\mathbf{x}' \equiv \{x'_1, x'_2 \dots x'_K\}$, $\boldsymbol{\mu} = \{\mu_1, \mu_2 \dots \mu_K\}$ and

$\boldsymbol{\mu}' = \{\mu'_1, \mu'_2 \dots \mu'_K\}$:

$$\mathcal{S}(\mathbf{x}, \boldsymbol{\mu}; \mathbf{x}', \boldsymbol{\mu}') = \langle \text{vac} | \left[\prod_{i=1}^K a_{\mu_i}(x_i) \right] \mathcal{S} \left[\prod_{i=1}^K a_{\mu'_i}^\dagger(x'_i) \right] | \text{vac} \rangle. \quad (4.18)$$

Note that the relations $\exp(-iH_0t)a_k(x_k)\exp(iH_0t) = a_k(x_k + t)$ and $\exp(iHt)a_k(x_k)\exp(-iHt) = a_k(x_k; t)$ together with $H_0|\text{vac}\rangle = H|\text{vac}\rangle = 0$ immediately imply the following relationship between the scattering matrix element in Eq. 4.18 and the Heisenberg picture optical mode position-domain annihilation operators:

$$\mathcal{S}(\mathbf{x}, \boldsymbol{\mu}; \mathbf{x}', \boldsymbol{\mu}') = \lim_{\substack{t_+ \rightarrow \infty \\ t_- \rightarrow -\infty}} \langle \text{vac} | \left[\prod_{i=1}^K a_{\mu_i}(x_i + t_+; t_+) \right] \left[\prod_{i=1}^K a_{\mu'_i}^\dagger(x'_i + t_-; t_-) \right] | \text{vac} \rangle. \quad (4.19)$$

Using Eq. 4.4, and in the limit of $t_+ \rightarrow \infty$ and $t_- \rightarrow -\infty$, it follows that :

$$a_{\mu_i}(x_i + t_+; t_+) = \sum_{\nu_i=1}^N S_{\mu_i, \nu_i} a_{\nu_i}(x_i - x_{\mu_i}^0 + x_{\nu_i}^0 + t_-; t_-), \quad (4.20)$$

where $S_{i,j}$ are the elements of the classical scattering matrix \mathbf{S} . With this, the following explicit expression for $\mathcal{S}(\mathbf{x}, \boldsymbol{\mu}; \mathbf{x}', \boldsymbol{\mu}')$ as given by Eq. 4.19 can be obtained:

$$\mathcal{S}(\mathbf{x}, \boldsymbol{\mu}; \mathbf{x}', \boldsymbol{\mu}') = \sum_{\mathcal{P}_K} \prod_{l=1}^K S_{\mu_l, \mathcal{P}_K \mu'_l} \delta((x_l - x_{\mu_l}^0) - (\mathcal{P}_K x'_l - x_{\mathcal{P}_K \mu'_l}^0)), \quad (4.21)$$

where \mathcal{P}_K is a K element permutation. It can immediately be noticed that the quantum scattering matrix elements are completely determined in terms of the classical scattering matrix elements $S_{i,j}$. From Eq. 4.21, we can also evaluate the frequency domain scattering matrix elements $S(\boldsymbol{\omega}, \boldsymbol{\mu}; \boldsymbol{\omega}', \boldsymbol{\mu}')$ ($\boldsymbol{\omega} = \{\omega_1, \omega_2 \dots \omega_K\}$, $\boldsymbol{\omega}' =$

$\{\omega'_1, \omega'_2 \dots \omega'_K\}$, $\boldsymbol{\mu} = \{\mu_1, \mu_2 \dots \mu_K\}$ and $\boldsymbol{\mu}' = \{\mu'_1, \mu'_2 \dots \mu'_K\}$):

$$\mathcal{S}(\boldsymbol{\omega}, \boldsymbol{\mu}; \boldsymbol{\omega}', \boldsymbol{\mu}') = \int_{\mathbb{R}^K} \int_{\mathbb{R}^K} S(\mathbf{x}, \boldsymbol{\mu}; \mathbf{x}', \boldsymbol{\mu}') \left[\prod_{l=1}^K \frac{e^{i(\omega'_l x'_l - \omega_l x_l)}}{2\pi} \right] d^K \mathbf{x} d^K \mathbf{x}' \quad (4.22)$$

$$= \sum_{\mathcal{P}_K} \prod_{l=1}^K S_{\mathcal{P}_K \mu_l, \mu'_l} e^{-i\omega_l (x_{\mathcal{P}_K \mu_l}^0 - x_{\mu'_l}^0)} \delta(\mathcal{P}_K \omega_l - \omega'_l). \quad (4.23)$$

Note that the frequency domain scattering matrix doesn't have any connected parts [126] i.e. scattering of a K photon wave-packet from the linear optical device conserves the individual input frequencies. This is a direct consequence of the 'linearity' of the optical device. To gain more insight into the form of the scattering matrix in Eqs. 4.21 and 4.22, consider the calculation of the output state corresponding to a K -photon input state $|\psi_{\text{in}}\rangle$:

$$|\psi_{\text{in}}\rangle = \sum_{\boldsymbol{\mu}} \int_{\mathbb{R}^K} \psi_{\text{in}}(\boldsymbol{\omega}, \boldsymbol{\mu}) \left[\prod_{l=1}^K a_{\mu_l}^\dagger(\omega_l) \right] |\text{vac}\rangle d^K \boldsymbol{\omega}, \quad (4.24)$$

where the amplitude $\psi_{\text{in}}(\boldsymbol{\omega}, \boldsymbol{\mu})$ can be chosen, without any loss of generality, to be symmetric with respect to a simultaneous permutation of the indices $\boldsymbol{\mu}$ and $\boldsymbol{\omega}$: $\psi_{\text{in}}(\boldsymbol{\omega}, \boldsymbol{\mu}) = \psi_{\text{in}}(\mathcal{P}_K \boldsymbol{\omega}, \mathcal{P}_K \boldsymbol{\mu}) \forall K$ -element permutations \mathcal{P}_K . The output state is then given by:

$$|\psi_{\text{out}}\rangle = \sum_{\boldsymbol{\mu}} \int_{\mathbb{R}^K} \psi_{\text{out}}(\boldsymbol{\omega}, \boldsymbol{\mu}) \left[\prod_{l=1}^K a_{\mu_l}^\dagger(\omega_l) \right] |\text{vac}\rangle d^K \boldsymbol{\omega}, \quad (4.25)$$

where $\psi_{\text{out}}(\boldsymbol{\omega}, \boldsymbol{\mu})$ is given by:

$$\psi_{\text{out}}(\boldsymbol{\omega}, \boldsymbol{\mu}) = \frac{1}{N!} \sum_{\boldsymbol{\mu}'} \int_{\mathbb{R}^K} S(\boldsymbol{\omega}, \boldsymbol{\mu}; \boldsymbol{\omega}', \boldsymbol{\mu}') \psi_{\text{in}}(\boldsymbol{\omega}', \boldsymbol{\mu}') d^K \boldsymbol{\omega}'. \quad (4.26)$$

Assuming that the coordinate systems of the optical modes are chosen such that

$x_k^0 = 0 \forall k \in \{1, 2 \dots N\}$, from Eqs. 4.22 and 4.26 we obtain:

$$\psi_{\text{out}}(\boldsymbol{\omega}, \boldsymbol{\mu}) = \frac{1}{N!} \sum_{\boldsymbol{\mu}'} \sum_{\mathcal{P}_K} \left[\prod_{l=1}^K S_{\mu_l, \mathcal{P}_K \mu'_l} \right] \psi_{\text{in}}(\boldsymbol{\omega}, \mathcal{P}_K \boldsymbol{\mu}'). \quad (4.27)$$

Therefore,

$$|\psi_{\text{out}}\rangle = \sum_{\boldsymbol{\mu}} \int_{\mathbb{R}^K} \psi_{\text{in}}(\boldsymbol{\omega}, \boldsymbol{\mu}) \left[\prod_{l=1}^K \tilde{a}_{\mu_l}^\dagger(\omega_l) \right] |\text{vac}\rangle d^K \boldsymbol{\omega}, \quad (4.28)$$

where $\tilde{a}_i(\omega) = \sum_{j=1}^N S_{j,i}^* a_j(\omega)$. The application of the quantum scattering matrix of a linear optical device to an input state is equivalent to replacing the annihilation operators in the input state with \mathbf{S}^\dagger times the annihilation operators. This is the usual procedure used to analyze the impact of a linear optical element on an input state [135], and our analysis derives it from a Hamiltonian based description of the linear optical element and thus lends rigor to this procedure.

4.1.3 Normal modes of the point-coupling Hamiltonian

In this subsection, we diagonalize the point-coupling Hamiltonian and explicitly calculate the normal modes of the linear-optical device. Given that the frequency-domain annihilation operator of the n^{th} normal mode is $b_n(\omega)$, it should satisfy the following commutation relations:

$$[b_n(\omega), H] = \omega b_n(\omega), \quad (4.29a)$$

$$[b_n(\omega), b_m^\dagger(\omega')] = \delta_{n,m} \delta(\omega - \omega'), \quad (4.29b)$$

where H is the point-coupling Hamiltonian. Eq. 4.29a is a consequence of the Hamiltonian H being expressible as a sum of independent continua of harmonic oscillators in the normal mode basis:

$$H = \sum_{n=1}^N \int_{-\infty}^{\infty} \omega b_n^\dagger(\omega) b_n(\omega) d\omega, \quad (4.30)$$

and Eq. 4.29b is a result of the different normal modes being physically independent modes. As is shown in appendix F, using Eqs. 4.29a and 4.29b, the normal mode annihilation operators $b_n(\omega)$ can be chosen to be:

$$b_n(\omega) = \int_{-\infty}^{x_n^0} e^{-i\omega(x-x_n^0)} a_n(x) \frac{dx_n}{\sqrt{2\pi}} + \sum_{m=1}^N S_{m,n}^* \int_{x_m^0}^{\infty} e^{-i\omega(x-x_m^0)} a_m(x) \frac{dx_m}{\sqrt{2\pi}}, \quad (4.31)$$

where $S_{n,m}$ are the elements of the classical scattering matrix. To obtain a physical interpretation of this result, consider creating a photon in the normal mode described by $b_n(\omega)$ and calculating its projection on the modes described by $a_m(x_m)$ — this projection is given by the expectation $\langle \text{vac} | a_m(x_m) b_n^\dagger(\omega) | \text{vac} \rangle$ which can be readily evaluated using Eq. 4.31:

$$\langle \text{vac} | a_m(x_m) b_n^\dagger(\omega) | \text{vac} \rangle = \begin{cases} e^{i\omega(x_m-x_m^0)} \delta_{m,n} & \text{if } x_m < x_m^0 \\ e^{i\omega(x_m-x_m^0)} S_{m,n} & \text{if } x_m > x_m^0 \end{cases}. \quad (4.32)$$

This is exactly the same field profile that would be obtained on classically exciting the linear optical device through the n^{th} input port at frequency ω , and calculating the fields scattered in all the output ports — the n^{th} normal mode is simply the continuum of quantum harmonic oscillators associated with this field profile.

Finally, Eq. 4.31 can be inverted to relate the annihilation operators $a_n(x)$ to the normal mode annihilation operators $b_n(\omega)$ (refer to appendix F for details):

$$a_n(x_n) = \int_{-\infty}^{\infty} \frac{d\omega}{\sqrt{2\pi}} e^{i\omega(x_n-x_n^0)} \begin{cases} b_n(\omega) & \text{if } x_n > x_n^0 \\ \sum_{m=1}^N S_{n,m} b_m(\omega) & \text{if } x_n < x_n^0 \end{cases}, \quad (4.33)$$

where, again, we see that the modes described by $a_n(x)$ are identical to the normal modes at points before the linear-optical device (i.e. $x_n < x_n^0$ in Eq. 4.33) and their linear combination at points after the linear-optical device. Eqs. 4.31 and 4.33 thus provides a connection between the point-coupling Hamiltonian for linear-optical device and a direct quantization of the normal modes of the device [128].

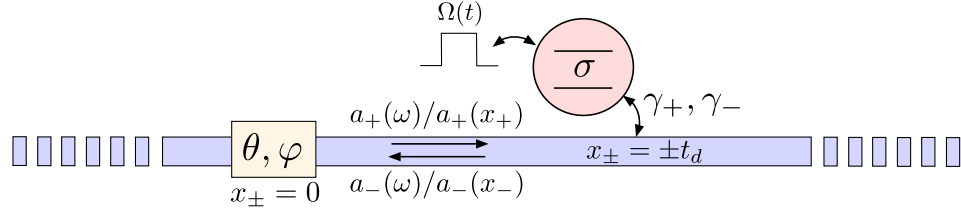


Figure 4.3: Schematic figure of the time-delayed feedback system. A two-level system with de-excitation operator σ couples to a waveguide which supports both forward propagating and backward propagating waveguide modes with frequency-domain (position-domain) annihilation operators $a_+(\omega)$ and $a_-(\omega)$ ($a_+(x_+)$ and $a_-(x_-)$) respectively. A mirror, modelled as a beam-splitter on the forward and backward propagating waveguide mode with parameters (θ, φ) , is located as $x_{\pm} = 0$ and the two-level system couples to both the waveguide modes at a distance t_d from the mirror. The decay rates of the two-level system into the forward and backward propagating waveguide modes are denoted by γ_+ and γ_- respectively. Finally, we also consider the dynamics of this system when the two-level system is driven by an external laser pulse — $\Omega(t)$ denotes the complex amplitude of the laser pulse that drives the two-level system.

4.2 Matrix-product-state based simulations of time-delayed feedback systems

In this section, we use the point-coupling Hamiltonian proposed in the section 4.1 to develop an MPS update for a two-level system coupled to a waveguide with a partially transmitting mirror. Using the formulated MPS update, we study the impact of the less than unity reflectivity of the mirror on the dynamics of the time-delayed feedback system.

The system under consideration is a two-level system with a time-delayed feedback shown in Fig. 4.3. The Hamiltonian for this system can be expressed as a sum of a two-level system Hamiltonian, waveguide Hamiltonian and the mirror Hamiltonian (which is modeled as a point interaction between the forward and backward propagating modes):

$$H(t) = H_{\text{TLS}}(t) + H_{\text{wg}} + H_{\text{mirror}} + H_{\text{wg-TLS}}, \quad (4.34)$$

where $H_{\text{TLS}}(t)$ is the Hamiltonian of the two-level system including a coherent drive, H_{wg} is the Hamiltonian describing the forward and backward propagating waveguide modes, H_{mirror} is the Hamiltonian of the mirror providing feedback to the two-level system and $H_{\text{wg-TLS}}$ is the interaction Hamiltonian between the two-level system and the two waveguide modes:

$$H_{\text{TLS}}(t) = \omega_e \sigma^\dagger \sigma + \Omega(t) (\sigma e^{i\omega_0 t} + \sigma^\dagger e^{-i\omega_0 t}), \quad (4.35a)$$

$$H_{\text{wg}} = \sum_{k \in \{+, -\}} \int_{-\infty}^{\infty} \omega a_k^\dagger(\omega) a_k(\omega) d\omega, \quad (4.35b)$$

$$H_{\text{mirror}} = 2i \tan\left(\frac{\theta}{2}\right) [e^{i\varphi} a_+(x_+ = 0) a_-^\dagger(x_- = 0) - e^{-i\varphi} a_-(x_- = 0) a_+^\dagger(x_+ = 0)], \quad (4.35c)$$

$$H_{\text{wg-TLS}} = [\sqrt{\gamma_+} \sigma^\dagger a_+(x_+ = t_d) + \sqrt{\gamma_-} \sigma^\dagger a_-(x_- = -t_d) + \text{h.c.}]. \quad (4.35d)$$

Here σ is the de-excitation operator for a two-level system with resonant frequency ω_e , $a_+(\omega)$ and $a_-(\omega)$ are the frequency-domain annihilation operators for the forward and backward propagating waveguide modes respectively and $a_+(x_+)$ and $a_-(x_-)$ are the position-domain annihilation operators for the forward and backward propagating waveguide modes respectively. Note that the x -axis for the coordinate systems for the forward and backward propagating waveguide modes are chosen to be in their direction of propagation with the same origin. A mirror, modeled with a beam splitter Hamiltonian between the forward and backward propagating waveguide modes with parameters (θ, φ) , is located at $x_\pm = 0$. The two-level system interacts with the waveguide (with a decay rate γ_+ into the forward propagating waveguide mode and γ_- into the backward propagating waveguide mode) at a distance of t_d from the mirror — this corresponds to the point with coordinates $x_+ = t_d$ and $x_- = -t_d$ in the coordinate systems of the forward and backward propagating waveguide modes. Furthermore, the two-level system is driven with a laser pulse at frequency ω_0 and pulse-shape $\Omega(t)$.

We first go into a frame rotating as per the Hamiltonian $H_0 = \omega_0 \sigma^\dagger \sigma + H_{\text{wg}} + H_{\text{mirror}}$.

In this frame, the state of the system evolves as per the Hamiltonian $\tilde{H}(t)$:

$$\tilde{H}(t) = \delta_e \sigma^\dagger \sigma + \Omega(t) \sigma_x + (\sqrt{\gamma_+} \sigma^\dagger a_+(x_+ = t_d; t) e^{i\omega_0 t} + \sqrt{\gamma_-} \sigma^\dagger a_-(x_- = -t_d; t) e^{i\omega_0 t} + \text{h.c.}), \quad (4.36)$$

where $\delta_e = \omega_e - \omega_0$ and $a_\pm(x_\pm = \pm t_d; t)$ are the Heisenberg picture operators corresponding to $a_\pm(x_\pm = \pm t_d)$ with respect to H_0 at time t , subject to the initial condition $a_\pm(x_\pm = \pm t_d; t = 0) = a_\pm(x_\pm = \pm t_d)$. From Eq. 4.4 and for $t > 0$, we obtain:

$$a_+(x_+ = t_d; t) = e^{-i\omega_0(t-t_d)} \begin{cases} A_+(t) & \text{if } t < t_d \\ A_+(t) \cos \theta + e^{i\varphi} A_-(t - 2t_d) \sin \theta & \text{if } t > t_d \end{cases}, \quad (4.37a)$$

$$a_-(x_- = -t_d; t) = e^{-i\omega_0(t+t_d)} A_-(t), \quad (4.37b)$$

where we have defined the operators $A_\pm(t)$ via:

$$A_\pm(t) = \int_{-\infty}^{\infty} a_\pm(\omega) e^{-i(\omega - \omega_0)(t \mp t_d)} \frac{d\omega}{\sqrt{2\pi}}. \quad (4.38)$$

An MPS update for the state of the system in the rotating frame with respect to H_0 can now be framed using the procedure outlined in Ref. [39] — the first step is to discretize the waveguide Hilbert space. Using a discretization step Δt , we can define the waveguide bin operators $A_\pm[k]$ in terms of the operators $A_\pm(t)$ via:

$$A_\pm[k] = \int_{k\Delta t}^{(k+1)\Delta t} A_\pm(t) \frac{dt}{\sqrt{\Delta t}}, \quad (4.39)$$

which satisfy the commutation relations $[A_+[i], A_+^\dagger[j]] = \delta_{i,j}$ and $[A_-[i], A_-^\dagger[j]] = \delta_{i,j}$. The state of the entire system, including the waveguide and the two-level system, can be represented by a matrix-product state with the two-level system corresponding to the first site in the matrix product state, and the subsequent sites corresponding to the waveguide bins. The Hilbert space of the k^{th} waveguide bin is spanned by the tensor product of the Hilbert spaces of the harmonic oscillators whose annihilation operators are $A_+[k]$ and $A_-[k]$. To compute the the state at $t = k\Delta t$ from the state at

$t = (k+1)\Delta t$, we act on the matrix product state with the unitary operator $U[k+1, k]$ defined by:

$$U[k+1, k] = e^{-iH[k+1, k]}, \quad (4.40)$$

where

$$\begin{aligned} H[k+1, k] &= \int_{k\Delta t}^{(k+1)\Delta t} \tilde{H}(t) dt \\ &= \delta_e \Delta t \sigma^\dagger \sigma + \Omega_k \sigma_x + \begin{cases} \sigma^\dagger (\sqrt{\gamma_+ \Delta t} e^{i\omega_0 t_d} A_+[k] + \sqrt{\gamma_- \Delta t} e^{-i\omega_0 t_d} A_-[k]) + \text{h.c.} & \text{if } k \leq n_d \\ \sigma^\dagger (\sqrt{\gamma_+ \Delta t} e^{i\omega_0 t_d} (A_+[k] \cos \theta + e^{i\varphi} A_-[k - 2n_d] \sin \theta) \\ \quad + \sqrt{\gamma_- \Delta t} e^{-i\omega_0 t_d} A_-[k]) + \text{h.c.} & \text{if } k > n_d \end{cases}, \end{aligned} \quad (4.41)$$

where $n_d = \lfloor t_d / \Delta t \rfloor$ and $\Omega_k = \Omega(k\Delta t)\Delta t$. The application of $U[k+1, k]$ on the matrix product state at time step k requires the implementation of a long-range gate, since it acts on the site corresponding to the two-level system, the k^{th} waveguide bin and the $(k - 2n_d)^{\text{th}}$ waveguide bin. Following the approach introduced in Ref. [39], we implement this long range gate using a sequence of swap operations [136] followed by a short-range gate corresponding to $U[k+1, k]$ [137]. The update is implemented using the tensor network state python library `tncontract` along with `qutip` [138].

We first validate our MPS update implementation against the implementation introduced in Ref. [39] for an ideal mirror (i.e. $\theta = \pi/2$). Fig. 4.4 shows a comparison between the two implementation for two distinct settings — Fig. 4.4(a) in which the emitter is initially prepared in its excited state and allowed to decay into the waveguide without any external driving, and Fig. 4.4(b) in which the emitter is initially in its ground state and then driven by an exponentially decaying pulse ($\Omega(t) = \Omega_0 e^{-\alpha t}$). We simulate both of these settings for different mirror phase φ — as is known in such feedback systems with ideal mirrors, a properly chosen mirror phase can result in the emitter not decaying completely into the waveguide mode, rather exciting the *bound state* that exists between the emitter and the waveguide mode. We observe such incomplete decay for $\varphi = 0$, and a complete decay of the emitter into the waveguide

mode for other mirror phases. Moreover, the MPS update implementation presented in this section agrees perfectly with the MPS update implementation introduced in Ref. [39]. This perfect agreement can be analytically explained by considering the normal modes of the point-coupling Hamiltonian describing the mirror (as described in section 4.1.3). Using Eq. 4.31 for a perfect mirror ($\theta = \pi/2$), the two normal modes $b_{L,R}(\omega)$ can be expressed in terms of $a_{\pm}(x)$ via:

$$b_L(\omega) = \int_{-\infty}^0 a_+(x_+) e^{-i\omega x_+} \frac{dx_+}{\sqrt{2\pi}} - e^{i\varphi} \int_0^{\infty} a_-(x_-) e^{-i\omega x_-} \frac{dx_-}{\sqrt{2\pi}}, \quad (4.42a)$$

$$b_R(\omega) = \int_{-\infty}^0 a_-(x_-) e^{-i\omega x_-} \frac{dx_-}{\sqrt{2\pi}} + e^{-i\varphi} \int_0^{\infty} a_+(x_+) e^{-i\omega x_+} \frac{dx_+}{\sqrt{2\pi}}. \quad (4.42b)$$

Clearly, $b_L^\dagger(\omega)$ only creates excitations to the left of the mirror (which do not interact with the two-level system) while $b_R^\dagger(\omega)$ only creates excitations to the right of the mirror (which interact with the two-level system). Indeed, using Eq. 4.33, it can easily be seen that the interaction Hamiltonian between the waveguide and the two-level system ($H_{\text{wg-TLS}}$ defined in Eq. 4.35d) can be entirely expressed in terms of $b_R(\omega)$:

$$H_{\text{wg-TLS}} = \int_{-\infty}^{\infty} \left[(\sqrt{\gamma_+} \sigma^\dagger e^{i(\omega t_d + \varphi)} + \sqrt{\gamma_-} \sigma^\dagger e^{-i\omega t_d}) b_R(\omega) + \text{h.c.} \right] \frac{d\omega}{\sqrt{2\pi}}, \quad (4.43)$$

which is identical to the interaction Hamiltonian used in Ref. [39].

Next, we study the impact of the non-ideality (i.e. the mirror reflection being less than 1) in the mirror on the dynamics of the feedback system. Changing the mirror reflection is equivalent to changing the parameter θ describing the mirror. Fig. 4.5 shows the impact of θ on the dynamics of the feedback system. Again, we simulate two different settings — Fig. 4.5(a) in which the emitter is initially prepared in its excited state and allowed to decay into the waveguide without any external driving, and Fig. 4.5(b) in which the emitter is initially in its ground state and then driven by an exponentially decaying pulse ($\Omega(t) = \Omega_0 e^{-\alpha t}$). We note that unlike the case of an ideal mirror, having a less than unity reflectivity implies that there is no bound

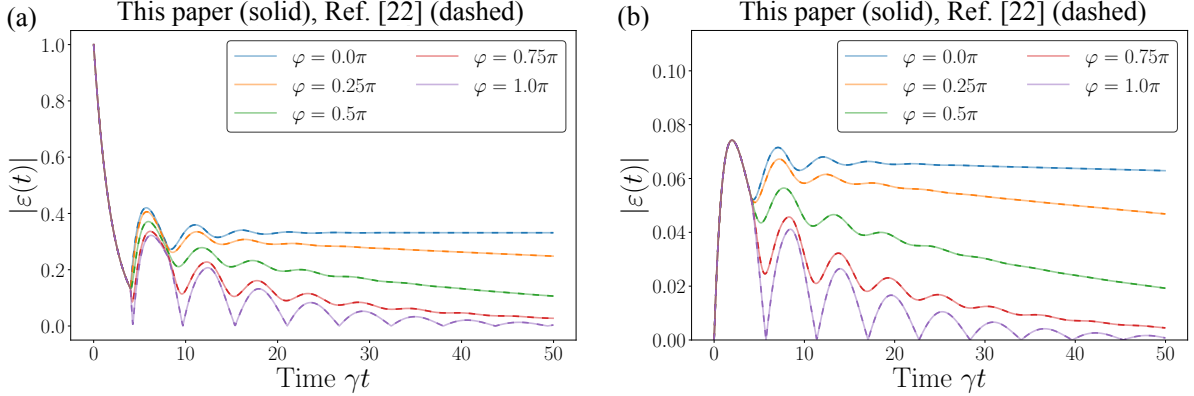


Figure 4.4: Validation of our MPS update implementation against the implementation introduced in Ref. [39] for an ideal mirror (i.e. $\theta = \pi/2$) for two simulation settings: (a) Simulation of an undriven two-level system ($\Omega(t) = 0$) which is initially in its excited state for different mirror phases φ and (b) simulation of a two-level system initially in its ground state and driven by an exponentially decaying pulse ($\Omega(t) = \Omega_0 e^{-\alpha t}$ for $t > 0$) for different mirror phases φ . $|\varepsilon(t)|$ is the probability amplitude of the two-level system being in the excited state computed using $|\varepsilon(t)|^2 = \langle \sigma^\dagger \sigma \rangle$. It is assumed that $\gamma_+ = \gamma_- = \gamma/2$, $\delta_e = \omega_e - \omega_0 = 0$, $\omega_0 t_d = \pi$, $\gamma t_d = 2$ and $\alpha = 2\gamma$. For the discretization into an MPS, we use $\gamma \Delta t = 0.05$, and truncate the dimensionality of the Hilbert space of each waveguide bin to 2 for both forward and backward propagating modes. A threshold of 0.01 is used in all the Schmidt decompositions performed while applying the swap gates and the short-range gates. Refer to appendix G for convergence studies of the MPS simulations.

state that the emitter can decay into. Consequently, the emitter always decays to the ground state — however, as is seen in Fig. 4.5, the decay rate can be controlled by controlling the reflectivity of the mirror. While this seems reminiscent of the Purcell effect, we note that even with a less than unity reflectivity, the emitter does not decay exponentially into its ground state — this is a consequence of the non-Markovian nature of the feedback system.

Finally, we point out that an alternative to using the point-coupling Hamiltonian for analyzing the feedback system considered in this section is to directly formulate the Hamiltonian using the normal modes of the mirror-waveguide system. Such a formulation would also be able to capture the impact of the mirror reflectivity on the dynamics of the two-level system if it was accounted for in the construction of the

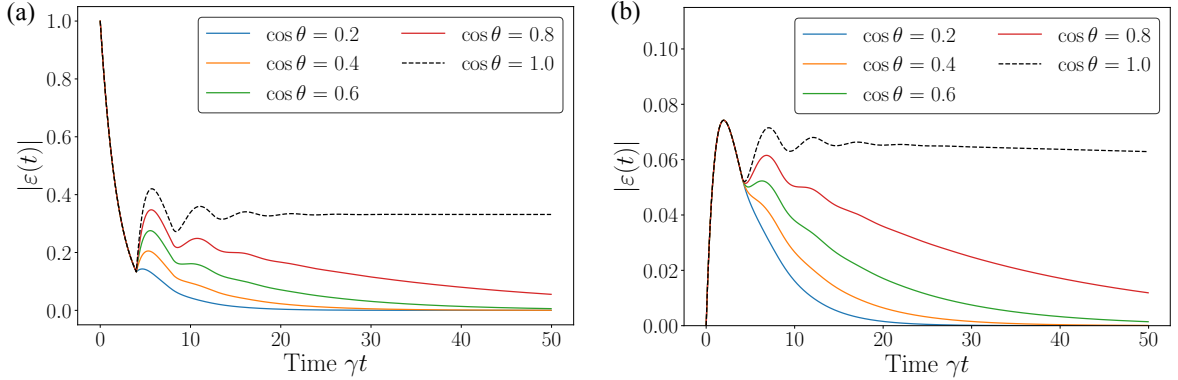


Figure 4.5: Impact of mirror reflectivity on the dynamics of the time-delayed feedback system for two simulation settings: (a) Simulation of an undriven two-level system ($\Omega(t) = 0$) which is initially in its excited state for different mirror reflectivities $\cos \theta$ and (b) simulation of a two-level system initially in its ground state and driven by an exponentially decaying pulse ($\Omega(t) = \Omega_0 e^{-\alpha t}$ for $t > 0$) for different mirror reflectivities $\cos \theta$. $|\varepsilon(t)|$ is the probability amplitude of the two-level system being in the excited state computed using $|\varepsilon(t)|^2 = \langle \sigma^\dagger \sigma \rangle$. It is assumed that $\gamma_+ = \gamma_- = \gamma/2$, $\delta_e = \omega_e - \omega_0 = 0$, $\omega_0 t_d = \pi$, $\gamma t_d = 2$, $\varphi = 0$ and $\alpha = 2\gamma$. For the discretization into an MPS, we use $\gamma \Delta t = 0.05$, and truncate the dimensionality of the Hilbert space of each waveguide bin to 2 for both forward and backward propagating modes. A threshold of 0.01 is used in all the Schmidt decompositions performed while applying the swap gates and the short-range gates. Refer to appendix G for convergence studies of the MPS simulations.

normal modes. The point-coupling Hamiltonian provides an alternative, and equivalent (as shown in section 4.1.3), approach for modelling linear-optical devices. Apart from the didactic importance of this result, we expect it to be of utility in understanding complicated feedback systems with multiple linear optical devices providing feedback.

4.3 Conclusion

In summary, we have solved the problem of calculating the Hamiltonian for a frequency-independent linear-optical device from its classical scattering matrix. It is shown that an application of the quantum scattering matrix corresponding to the proposed

Hamiltonian on an input state is equivalent to applying the inverse of the classical scattering matrix of the linear-optical device on the annihilation operators in the input state. We also diagonalize the point-coupling Hamiltonian and provide a connection between the point-coupling Hamiltonian and the quantization of normal modes of the linear-optical device [128]. Finally, we demonstrate the practical utility of the proposed Hamiltonian by using it to rigorously formulate an MPS-based update for a time-delayed feedback system wherein the linear-optical device providing feedback is described by a full scattering matrix as opposed to a hard boundary condition.

Chapter 5

Conclusions and outlook

In this thesis, I have presented optimization and tensor network simulation based computational solutions to surmount or understand certain obstacles on the path to realizing quantum computation at scale.

First, I presented a strategy to inverse design the temporal shape of the driving field of a quantum emitter ensemble-based microwave-to-optical single-photon transducer to compensate for the effects of inhomogeneous broadening and improve efficiency, serving to enable quantum communication between superconducting quantum computers over optical fibre networks. This design strategy is applicable to different physical platforms including color centers or rare-earth ions in solid-state hosts. For future work, the optimization-based design technique can be extended to ensembles that are orders of magnitude larger by frequency-binning the randomly distributed transition frequencies [139]. In some physical systems the transition frequencies of the emitters can be modulated (for e.g., via Stark effect in V_{Si} centers in SiC). Previous research [140] has shown that direct modulation of the transition frequencies can also be used to compensate for inhomogeneous broadening in a cavity-QED setting. It is expected that optimization-based design for transducers can also be applied with the direct modulation as the degree of freedom instead of the driving field.

Second, I described a numerical method, based on Lagrangian duality, to efficiently compute rigorous lower bounds on the performance of any given quantum circuit subject to depolarizing noise. The computed bounds are dependent on the architecture

of the specified circuit, and provide a way of determining the possibility of a quantum computational advantage. This method opens the door to promising avenues of future research. Larger-scale tensor-network numerics can allow the study of higher dimensional circuits, with a number of qubits reaching state-of-the-art experiments. Moreover, extensions of the method to continuous-time would better capture experimental systems, and even allow the application of this method to understanding the performance of quantum adiabatic algorithms [24]. Finally, the Lagrangian dual formulation of lower bounds, apart from being a numerical tool, could also shed rigorous theoretical insights in understanding resilience of quantum circuit architectures to noise.

Finally, I described a method to analytically calculate the Hamiltonian given the classical scattering matrix for an arbitrary frequency-independent linear optical device that couples optical modes at a single spatial location. I presented that such a Hamiltonian model can be used to generalize tensor network-based simulations of time-delayed feedback quantum optical systems to include arbitrary linear optical devices. Thus, this method opens up the way to simulate more exotic feedback systems in the future, possibly with use in realizing quantum computation, simulation and memories.

Appendix A

Maximising transduction efficiency through a homogeneous ensemble

For a homogeneous ensemble, as there are only two bright states $\{S_{+,1}^\dagger|G\rangle, S_{-,1}^\dagger|G\rangle\}$ that couple to the waveguides, the ensemble can be equivalently considered to be a single emitter system with the coupling rates to the waveguides enhanced by N . The effective Hamiltonian of the equivalent single-emitter system is,

$$H_{\text{eq}} = \left(\delta_\mu - \frac{i(\Gamma + N\gamma)}{2} \right) S_{\mu,1}^\dagger S_{\mu,1} + \left(\delta_{\text{opt}} - \frac{i(\Gamma + N\gamma)}{2} \right) S_{\text{opt},1}^\dagger S_{\text{opt},1} + \Omega(S_{\mu,1}^\dagger S_{\text{opt},1} + \text{H. c.}). \quad (\text{A.1})$$

The transduction spectrum $\tau(\omega)$ through this system is given by [20],

$$\tau(\omega) = \sum_{s \in \{+, -\}} \frac{\langle G | L_{\text{opt}} S_{s,1}^\dagger | G \rangle \langle G | S_{s,1} L_\mu^\dagger | G \rangle}{\omega - E_{s,1}} \quad (\text{A.2})$$

where $E_{\pm,1}$ are the eigenvalues of H_{eq} . Assuming $\delta_\mu = \delta_{\text{opt}} = 0$, Eq. A.2 leads to,

$$|\tau(\omega)| = \frac{N\gamma\Omega}{|(\omega - E_{+,1})(\omega - E_{-,1})|} \quad (\text{A.3})$$

where $E_{\pm,i} = \left(-\frac{i(\Gamma+N\gamma)}{2} \pm \Omega\right)$. For $|\Omega| \leq (N\gamma + \Gamma)/2$, $|\tau(\omega)|$ peaks at $\omega = 0$, with

$$|\tau(0)| = \frac{N\gamma\Omega}{\Omega^2 + \left(\frac{N\gamma+\Gamma}{2}\right)^2}. \quad (\text{A.4})$$

Hence, $|\tau(0)|$ is maximised when $\Omega = (N\gamma + \Gamma)/2$ and in that case, $|\tau(0)| = \frac{N\gamma}{\Gamma+N\gamma}$. We point out that when $|\Omega| \gg (N\gamma + \Gamma)/2$, the transduction spectrum has two peaks at $\approx \pm\Omega$, with $|\tau(\pm\Omega)| = \frac{N\gamma}{\Gamma+N\gamma}$. As high drive strengths can be experimentally undesirable, we use the constant drive of least strength that maximises the transduction efficiency, i.e., $\Omega = (N\gamma + \Gamma)/2$, as the benchmark against which the optimized drives are judged.

Appendix B

Hybridization of eigenstates of a homogeneous ensemble with the introduction of inhomogeneity

Consider the following separation of the effective Hamiltonian of an inhomogeneous ensemble into a Hamiltonian representing a homogeneous ensemble (H_0) and a perturbation term representing the inhomogeneity (V),

$$H_{\text{eff}} = H_0 + \lambda V \tag{B.1}$$

$$H_0 = \sum_i \left[-\frac{i\Gamma}{2} \sigma_\mu^{i\dagger} \sigma_\mu^i - \frac{i\Gamma}{2} \sigma_{\text{opt}}^{i\dagger} \sigma_{\text{opt}}^i \right] + \sum_i \Omega (\sigma_\mu^{i\dagger} \sigma_{\text{opt}}^i + \text{H. c.}) - \frac{i}{2} L_\mu^\dagger L_\mu - \frac{i}{2} L_{\text{opt}}^\dagger L_{\text{opt}} \tag{B.2}$$

$$V = \sum_i \left[\delta_\mu^i \sigma_\mu^{i\dagger} \sigma_\mu^i + \delta_{\text{opt}}^i \sigma_{\text{opt}}^{i\dagger} \sigma_{\text{opt}}^i \right]. \tag{B.3}$$

Defining, $|E_{\pm,i}\rangle = S_{\pm,i}^\dagger |G\rangle$, the eigenstates and eigenvalues of H_0 are,

$$H_0|E_{\pm,1}\rangle = \left(-\frac{i(\Gamma + N\gamma)}{2} \pm \Omega \right) |E_{\pm,1}\rangle \quad (\text{B.4})$$

$$H_0|E_{\pm,i}\rangle = \left(-\frac{i\Gamma}{2} \pm \Omega \right) |E_{\pm,i}\rangle, \quad i \neq 1 \quad (\text{B.5})$$

$$(\text{B.6})$$

With the introduction of the perturbation, the first order correction to the eigenstate $|E_{+,1}\rangle$ is,

$$|E_{+,1}\rangle \rightarrow |E_{+,1}\rangle + \lambda \sum_{\substack{i \neq 1, \\ s \in \{+, -\}}} |E_{s,i}\rangle \frac{\langle E_{s,i}|V|E_{+,1}\rangle}{E_{s,i} - E_{+,1}} + \lambda |E_{-,1}\rangle \frac{\langle E_{-,1}|V|E_{+,1}\rangle}{E_{-,1} - E_{+,1}}. \quad (\text{B.7})$$

The second term in Eq. B.7 evaluates to zero and,

$$V|E_{+,1}\rangle = \frac{(\delta_\mu^1 + \delta_{\text{opt}}^1)}{2} |E_{+,1}\rangle + \frac{(\delta_\mu^1 - \delta_{\text{opt}}^1)}{2} |E_{-,1}\rangle. \quad (\text{B.8})$$

Thus, the perturbation changes the eigenstate as,

$$|E_{+,1}\rangle \rightarrow |E_{+,1}\rangle - \frac{\lambda(\delta_\mu^1 - \delta_{\text{opt}}^1)}{4\Omega} |E_{-,1}\rangle. \quad (\text{B.9})$$

This indicates that the relevant frequency scale to compare the inhomogeneous broadening to is the drive strength Ω , which explains the variation of the superradiance metric with cooperativity in the unoptimized case in Fig. 4a. The unoptimized drive strength is chosen to be $\Omega(t) = (N\gamma + \Gamma)/2$ and as cooperativity is reduced by increasing Γ , the unoptimized drive strength increases, whereas the inhomogeneous broadening remains constant. Consequently, the hybridisation of the eigenstates away from that of a homogeneous ensemble decreases and the superradiance metric is higher on average.

Appendix C

Free fermion formulation

In this section, we describe our approach to numerical studies of Gaussian fermionic systems. We describe the fermionic system model and how the energy of the state at the output of the noisy circuit and the information content-based dual function (3.15) can be efficiently calculated by utilizing covariance matrices and quadratic Hamiltonian transformations.

C.0.1 Model

We consider N fermions arranged in a lattice and define for each lattice site x the Majorana operators c_x^1, c_x^2 as satisfying the following anti-commutation relations,

$$\begin{aligned} \{c_x^1, c_{x'}^1\} &= \{c_x^2, c_{x'}^2\} = \delta_{xx'} \\ \{c_x^1, c_{x'}^2\} &= 0, \quad \forall x, x' \in \text{lattice}. \end{aligned} \tag{C.1}$$

We choose the target Hamiltonian H to be quadratic,

$$H = i \sum_{\alpha, \alpha', x, x'} h_{x, x'}^{\alpha, \alpha'} c_x^\alpha c_{x'}^{\alpha'}.$$

Defining the operator valued vector,

$$\vec{c} = \left(c_1^1, c_2^1, \dots, c_N^1, c_1^2, c_2^2, \dots, c_N^2 \right)^T, \quad (\text{C.2})$$

the target Hamiltonian can be written as $H = i\vec{c}^T h \vec{c}$ where the matrix h specifying the Hamiltonian H is real and anti-symmetric. The ground state energy of the target Hamiltonian can be computed by diagonalization of its compact representation h [141].

C.0.2 Calculation of the noisy circuit output

The output energy, with respect to the quadratic target Hamiltonian H , can be computed from the covariance matrix of the state at the end of the circuit. We define the covariance matrix of a state ρ as,

$$\gamma_{x,x'}^{\alpha,\alpha'} = i\text{Tr}(\rho[c_x^\alpha, c_{x'}^{\alpha'}]), \quad (\text{C.3})$$

where $[\cdot, \cdot]$ denotes the commutator. The energy of a state ρ with respect to the target Hamiltonian H is then [141],

$$\text{Tr}(\rho H) = -\frac{\text{Tr}(h\gamma)}{2}. \quad (\text{C.4})$$

The covariance matrix of the state after each instance of Gaussian unitary or noise in the circuit can be calculated by evolving the covariance matrix γ_0 of the vacuum (γ_0 can be analytically calculated [141]) using the following transformations,

1. *Unitary:* Any Gaussian unitary can be expressed as $U = \exp(-iH_U)$, where $H_U = i\vec{c}^T h_U \vec{c}$ is the generating quadratic Hamiltonian, and it transforms the covariance matrix of the state as [141],

$$\gamma \rightarrow e^{2h_U} \gamma e^{-2h_U}. \quad (\text{C.5})$$

2. *Noise:* Depolarizing noise with probability p acting on the fermion at lattice

site x transforms the covariance matrix in the following manner [141, 142],

$$\gamma \rightarrow p\tilde{\gamma} + (1-p)\gamma, \quad (\text{C.6})$$

where the matrix $\tilde{\gamma}$ is obtained from the input covariance matrix γ by zeroing out the rows and columns corresponding to the fermion at site x , i.e.,

$$\tilde{\gamma}_{x',x''}^{\alpha,\alpha'} = \begin{cases} 0, & \text{if } x' = x \text{ or } x'' = x \\ \gamma_{x',x''}^{\alpha,\alpha'}, & \text{else.} \end{cases} \quad (\text{C.7})$$

C.0.3 Calculation of the dual function

We choose the dual variables $\sigma_1, \sigma_2, \dots, \sigma_d$ to be quadratic Hamiltonians, i.e. we consider the following ansatz,

$$\sigma_t = i \sum_{\substack{\alpha,\alpha',x,x' \\ d(x,x') \leq r}} s_{x,x';t}^{\alpha,\alpha'} c_x^\alpha c_{x'}^{\alpha'} = i\vec{c}^T s_t \vec{c}, \quad t \in \{1, \dots, d\},$$

where $d(x, x')$ is a distance measure between two lattice sites and the coefficients $s_{x,x';t}^{\alpha,\alpha'}$ are real and can be arranged into an anti-symmetric matrix s_t . σ_t are thus local Hamiltonians with interaction range r .

In order to evaluate the circuit dual function (3.15), we calculate the effect of the circuit channels on the dual variables first, i.e. $\mathcal{E}_t^\dagger(\sigma_t)$. Each such channel is the composition of a Gaussian unitary channel and the depolarizing channel and both the unitary and noise channels map quadratic operators to quadratic operators. Hence, the channel's action can be expressed as a transformation of the compact Majorana representation s_t of the dual variable σ_t using the following transformation rules,

1. *Unitary:* Any Gaussian unitary can be expressed as $U = \exp(-iH_U)$, where $H_U = i\vec{c}^T h_U \vec{c}$ is the generating quadratic Hamiltonian. Conjugation of the dual variable $\sigma_t = i\vec{c}^T s_t \vec{c}$ by U transforms it into another quadratic operator

$\tilde{\sigma}_t = U\sigma_t U^\dagger = i\vec{c}^T \tilde{s}_t \vec{c}$, with the transformed Majorana representation \tilde{s}_t ,

$$\tilde{s}_t = e^{2h_U} s_t e^{-2h_U}. \quad (\text{C.8})$$

This transformation can be derived by expanding the conjugation using the Baker-Campbell-Hausdorff formula $e^B A e^{-B} = A + [B, A] + \frac{1}{2!}[B, [B, A]] + \frac{1}{3!}[B, [B, [B, A]]] + \dots$, and using the commutation relation,

$$\begin{aligned} [c_{x_1}^{\alpha_1} c_{x_2}^{\alpha_2}, c_{x_3}^{\alpha_3} c_{x_4}^{\alpha_4}] &= -c_{x_1}^{\alpha_1} c_{x_3}^{\alpha_3} \delta_{\alpha_2, \alpha_4} \delta_{x_2, x_4} + c_{x_1}^{\alpha_1} c_{x_4}^{\alpha_4} \delta_{\alpha_2, \alpha_3} \delta_{x_2, x_3} \\ &\quad - c_{x_3}^{\alpha_3} c_{x_2}^{\alpha_2} \delta_{\alpha_1, \alpha_4} \delta_{x_1, x_4} + c_{x_4}^{\alpha_4} c_{x_2}^{\alpha_2} \delta_{\alpha_1, \alpha_3} \delta_{x_1, x_3}. \end{aligned} \quad (\text{C.9})$$

2. *Noise*: The noise channel \mathcal{N}_x corresponding to depolarizing noise on the fermion at site x with probability p transforms the dual variable σ_t as,

$$\mathcal{N}_x(\sigma_t) = (1-p)\sigma_t + p\text{Tr}_x(\sigma_t) \otimes \frac{\mathbb{1}}{2}, \quad (\text{C.10})$$

where $\text{Tr}_x(\cdot)$ denotes partial trace over fermion at site x . Expanding out the partial trace term using linearity,

$$\begin{aligned} \text{Tr}_x(\sigma_t) \otimes \frac{\mathbb{1}}{2} &= \sum_{\alpha', \alpha'', x', x''} i s_{x', x''; t}^{\alpha', \alpha''} \text{Tr}_x(c_{x'}^{\alpha'} c_{x''}^{\alpha''}) \otimes \frac{\mathbb{1}}{2}, \\ &= \sum_{\alpha', \alpha'', x', x''} i s_{x', x''; t}^{\alpha', \alpha''} (1 - \delta_{x, x'}) (1 - \delta_{x, x''}) c_{x'}^{\alpha'} c_{x''}^{\alpha''}, \end{aligned} \quad (\text{C.11})$$

where we obtain the second line by using $\text{Tr}(c_{x'}^{\alpha'}) = 0$ and $s_{x', x''; t}^{\alpha', \alpha'} = 0 \forall (x', \alpha')$. Thus, the noise channel transforms the dual variable into another quadratic operator $\tilde{\sigma}_t = i\vec{c}^T \tilde{s}_t \vec{c}$ with the transformed Majorana representation,

$$\tilde{s}_t = p s_t + (1-p) z_t, \quad (\text{C.12})$$

where, using (C.11), the matrix z_t is obtained from s_t by zeroing out the rows

and columns corresponding to the fermion at site x , i.e.,

$$z_{x',x'';t}^{\alpha',\alpha''} = \begin{cases} 0, & \text{if } x' = x \text{ or } x'' = x \\ s_{x',x'';t}^{\alpha',\alpha''}, & \text{else.} \end{cases} \quad (\text{C.13})$$

To calculate the dual function (3.15), we need to calculate the Gibbs free energy of $H_t = \sigma_t - \mathcal{E}_{t+1}^\dagger(\sigma_{t+1})$ where H_t is a quadratic operator itself because, as mentioned earlier, the channel $\mathcal{E}_{t+1}^\dagger$ maps quadratic operators to quadratic operators. Therefore, $H_t = i\vec{c}^T h_t \vec{c}$ where the Majorana representation h_t can be obtained using the transformations described above. We calculate the free energy by diagonalizing H_t . This can be achieved by diagonalizing h_t — as h_t is anti-symmetric, it is possible [141] to find an orthogonal transformation O such that,

$$O^T h_t O = \bigoplus_{\alpha,x} \begin{pmatrix} 0 & \epsilon_{x;t} \\ -\epsilon_{x;t} & 0 \end{pmatrix}$$

We define the operator valued vector $\vec{c} = O^T \vec{c} = (\tilde{c}_1^1, \tilde{c}_2^1, \dots, \tilde{c}_N^1, \tilde{c}_1^2, \tilde{c}_2^2, \dots, \tilde{c}_N^2)^T$ and, due to the orthogonality of O , the operators \tilde{c}_x^α satisfy the Majorana anti-commutation relations (C.1). Using the newly defined Majorana operators, H_t can be written in a diagonal form as,

$$H_t = i \sum_x \epsilon_{x;t} (\tilde{c}_x^1 \tilde{c}_x^2 - \tilde{c}_x^2 \tilde{c}_x^1).$$

Using the diagonal form, the Gibbs free energy for H_t is,

$$\begin{aligned} \mathcal{F}(H_t, \lambda_t) &= \log \text{Tr} \exp \left(-\frac{i}{\lambda_t} \sum_x \epsilon_{x;t} (\tilde{c}_x^1 \tilde{c}_x^2 - \tilde{c}_x^2 \tilde{c}_x^1) \right) \\ &= \log \prod_x \text{Tr} \exp \left(-\frac{i\epsilon_{x;t}}{\lambda_t} (\tilde{c}_x^1 \tilde{c}_x^2 - \tilde{c}_x^2 \tilde{c}_x^1) \right). \end{aligned}$$

The operator exponentials above can be represented in the Fock space basis of the

fermion at site x ,

$$\exp\left(-\frac{i\epsilon_{x;t}}{\lambda_t}(\tilde{c}_x^1\tilde{c}_x^2 - \tilde{c}_x^2\tilde{c}_x^1)\right) = \begin{pmatrix} e^{\epsilon_{x;t}/\lambda_t} & 0 \\ 0 & e^{-\epsilon_{x;t}/\lambda_t} \end{pmatrix}$$

The free energy then simplifies to,

$$\mathcal{F}(H_t, \lambda_t) = \sum_x \log(e^{\epsilon_{x;t}/\lambda_t} + e^{-\epsilon_{x;t}/\lambda_t}),$$

and therefore it can be calculated just from the diagonalization of the $2N \times 2N$ dimensional matrix h_t .

Appendix D

Existence of quantum circuit and Hamiltonian where dual bound scales super-exponentially with circuit depth

We first recall the main result of Ref. [106] which analyzed error propagation in a family of random quantum circuits. Specifically, they considered brick-wall quantum circuits of depth d (assumed to be even) with unitaries $U_1, U_2 \dots U_d$, where

$$U_{d/2+1} = U_{d/2}^\dagger, U_{d/2+2} = U_{d/2-1}^\dagger, U_{d/2+3} = U_{d/2-2}^\dagger \dots U_d = U_1^\dagger.$$

The unitaries $U_1, U_2 \dots U_{d/2}$ are chosen randomly depending on the circuit architecture. We will specifically consider the 1D case, where $U_1, U_3, U_5 \dots$ are formed by applying random 2-qubit gates between qubits $(1, 2), (3, 4)(5, 6) \dots$ and $U_2, U_4, U_6 \dots$ are formed by applying random 2-qubit gates between qubits $(2, 3), (4, 5), (6, 7) \dots$. All the two qubit gates are chosen independently at random from an ensemble that forms a 2-design. Furthermore, we consider the noisy setting where depolarizing noise with probability p is applied to each qubit after every unitary layer. Ref. [106] establishes the following result characterizing the average energy of the output state

for a 2-local Hamiltonian. While the result of Ref. [106] holds for arbitrary two-local Hamiltonians, we will only consider the Hamiltonian $H = -\sum_{i=1}^N Z_i$.

Lemma D.0.1 (Ref. [106]) *The expectation value E of the Hamiltonian $H = -\sum_{i=1}^N Z_i$ with respect to the the output state of a circuit chosen randomly from the ensemble described above satisfies,*

$$\text{Prob} \left(\left| E + N(1-p)^{\Omega(d^2)} \right| \leq \alpha_0 \sqrt{N} \right) \geq 1 - 2e^{-2\alpha_0^2/2d^2}.$$

Proof: Consider the Hamiltonian $H = -\sum_{i=1}^N Z_i$, and choose the two qubit gates to be a Haar-random Clifford gate — since Haar-random Clifford gates form a 2-design [143], we can use lemma A.1. H satisfies $\text{Tr}(H) = 0$ and has operator norm $\|H\| = N$. We evaluate the dual function at the dual variables obtained by Heisenberg picture evolution of $-H$,

$$\sigma_d = -H, \sigma_t = -\mathcal{E}_{t+1}^\dagger \mathcal{E}_{t+2}^\dagger \dots \mathcal{E}_d^\dagger(H).$$

Note that for Clifford circuits, Z_i will be mapped to a single Pauli string [119], which is expressible as an MPO with bond dimension 1, and consequently σ_t will have a bond-dimension of at-most N . Since the Heisenberg picture evolution can be captured exactly with a MPO ansatz of bond dimension $O(N)$, the dual bound ℓ_D^{dual} with $D \leq O(N)$ is exactly equal to the energy E of the output of the noisy quantum circuit. Now, from lemma A.1, it follows that there must exist at least one 1D circuit such that

$$\ell_D^{\text{dual}} = -N(1-p)^{\Omega(d^2)} + O(\sqrt{N}),$$

with $D \leq O(N)$.

We now consider the lower bound ℓ^I obtained by only considering the information content of the state at the output of the circuit and neglecting the circuit constraints:

$$\ell^I = \underset{\rho: I(\rho) \leq N(1-p)^d}{\text{minimize}} \text{Tr}(H\rho).$$

A negative upper bound on ℓ^I which converges to $\text{Tr}(H/2^N) = 0$ exponentially with

d can be obtained by computing $\text{Tr}(H\rho)$ at

$$\rho = \left(p_d |0\rangle\langle 0| + (1 - p_d) \frac{I}{2} \right)^{\otimes N} \text{ where } p_d = (1 - p)^d.$$

Note that this ρ satisfies $I(\rho) = N(1 - p)^d$, and consequently $\text{Tr}(H\rho)$ is an upper bound on ℓ^I . For $H = \sum_{i=1}^N Z_i$, we then obtain $\text{Tr}(H\rho) = -N(1 - p)^d$ which implies $\ell^I \leq -N(1 - p)^{O(d)}$. \square

Appendix E

Solving Heisenberg equations of motion for point coupling Hamiltonian

The Heisenberg equation of motion (Eq. 4.3) can be easily integrated from t_0 to $t_0 + \tau$ (where $\tau > 0$) to obtain:

$$a_n(\omega; t_0 + \tau) = a_n(\omega; t_0) \exp(-i\omega\tau) - i \sum_{m=1}^N V_{n,m} e^{-i\omega x_n^0} \int_{t_0}^{t_0+\tau} a_m(x_m^0; t') e^{-i\omega(t_0+\tau-t')} \frac{dt'}{\sqrt{2\pi}} \quad (\text{E.1})$$

Therefore, it follows from Eq. 4.2 that $a_n(x_n; t_0 + \tau)$ is given by:

$$\begin{aligned} a_n(x_n; t_0 + \tau) &= a_n(x_n - \tau; t_0) - i \sum_{m=1}^N V_{n,m} \int_{t_0}^{t_0+\tau} a_m(x_m^0; t') \delta(x_n - x_n^0 - t_0 - \tau + t') dt' \\ &= a_n(x_n - \tau; t_0) - i \left[\sum_{m=1}^N V_{n,m} a_m(x_m^0; t_0 + \tau - (x_n - x_n^0)) \right] \Theta(x_n^0 \leq x_n \leq x_n^0 + \tau) \end{aligned} \quad (\text{E.2})$$

where the function $\Theta(x_1 \leq x \leq x_2)$ is defined in Eq. 4.5. Imposing Eq. E.2 at $x_n = x_n^0 \forall n \in \{1, 2 \dots N\}$, we obtain:

$$a_n(x_n^0; t_0 + \tau) = a_n(x_n^0 - \tau; t_0) - \frac{i}{2} \sum_{m=1}^N V_{n,m} a_m(x_m^0; t_0 + \tau) \forall n \in \{1, 2 \dots N\} \quad (\text{E.3})$$

from which we can obtain $a_n(x_n^0; t)$ in terms of operators at $t = t_0$:

$$\begin{bmatrix} a_1(x_1^0; t_0 + \tau) \\ a_2(x_2^0; t_0 + \tau) \\ \vdots \\ a_N(x_N^0; t_0 + \tau) \end{bmatrix} = \left(\mathbf{I} + \frac{i\mathbf{V}}{2} \right)^{-1} \begin{bmatrix} a_1(x_1^0 - \tau; t_0) \\ a_2(x_2^0 - \tau; t_0) \\ \vdots \\ a_N(x_N^0 - \tau; t_0) \end{bmatrix} \quad (\text{E.4})$$

where \mathbf{V} is a $N \times N$ Hermitian matrix formed by $V_{m,n}$ as its elements and \mathbf{I} is the identity matrix of size N . Substituting Eq. E.4 into Eq. E.2 together with the substitution $x_n = x_n^0 + y$, we obtain Eq. 4.4

Appendix F

Calculating normal modes of the point coupling Hamiltonian

Since the normal mode annihilation operator $b_n(\omega)$ is expressible as a linear combination of the annihilation operators $a_n(x_n)$, we assume the following ansatz for $b_n(\omega)$:

$$b_n(\omega) = \sum_{m=1}^N \int_{-\infty}^{\infty} \mathcal{F}_{n,m}(\omega, x) a_m(x + x_m^0) \frac{dx}{\sqrt{2\pi}}, \quad (\text{F.1})$$

where $\mathcal{F}_{n,m}(\omega, x)$ is a function that is to be determined. Using Eq. 4.29a, we obtain the following differential equation for $\mathcal{F}_{n,m}(\omega, x)$:

$$i \frac{\partial \mathcal{F}(\omega, x)}{\partial x} + \delta(x) \mathcal{F}(\omega, 0) \mathbf{V} = \omega \mathcal{F}(\omega, x). \quad (\text{F.2})$$

Here $\mathcal{F}(\omega, x)$ is a $N \times N$ complex matrix with the functions $\mathcal{F}_{n,m}(\omega, x)$ as its elements. The solution for Eq. F.2 is of the form:

$$\mathcal{F}(\omega, x) = \begin{cases} \mathcal{F}_+(\omega) e^{-i\omega x} & x > 0 \\ \mathcal{F}_-(\omega) e^{-i\omega x} & x < 0 \end{cases}. \quad (\text{F.3})$$

To evaluate the matrices $\mathcal{F}_+(\omega)$ and $\mathcal{F}_-(\omega)$, we use the boundary condition obtained on integrating Eq. F.2 across a small interval around $x = 0$:

$$-i[\mathcal{F}(\omega, x = 0^+) - \mathcal{F}(\omega, x = 0^-)] + \frac{1}{2}[\mathcal{F}(\omega, x = 0^+) + \mathcal{F}(\omega, x = 0^-)]\mathbf{V} = 0, \quad (\text{F.4})$$

from which it immediately follows that $\mathcal{F}_+(\omega) = \mathcal{F}_-(\omega)\mathbf{S}^\dagger$, where \mathbf{S} is the classical scattering matrix of the linear-optical device. Moreover, using Eq. F.2 along with Eq. 4.29b, we obtain $\mathcal{F}_+^\dagger(\omega)\mathcal{F}_-(\omega) = \mathbf{I}$ – any choice for $\mathcal{F}(\omega)$ is valid as long as it satisfies this constraint. Choosing $\mathcal{F}_-(\omega) = \mathbf{I}$ and $\mathcal{F}_+(\omega) = \mathbf{S}^\dagger$, we obtain Eq. 4.31.

To derive Eq. 4.33, we assume the following anstaz for $a_n(x_n)$ in terms of $b_n(\omega)$:

$$a_n(x + x_n^0) = \int_{-\infty}^{\infty} \sum_{n,m} \mathcal{G}_{n,m}(x, \omega) b_m(\omega) \frac{d\omega}{\sqrt{2\pi}}, \quad (\text{F.5})$$

where $\mathcal{G}_{n,m}(x, \omega)$ is a function that is to be determined. Note that $\mathcal{G}_{n,m}(x, \omega) = \sqrt{2\pi}[a_n(x + x_n^0), b_m^\dagger(\omega)]$ and therefore from Eq. F.1 it follows that $\mathcal{G}_{n,m}(x, \omega) = \mathcal{F}_{m,n}^*(\omega, x)$. We thus immediately obtain:

$$\mathcal{G}_{n,m}(x, \omega) = \begin{cases} \delta_{n,m} e^{i\omega(x-x_n^0)} & \text{if } x < x_n^0 \\ \mathbf{S}_{n,m} e^{i\omega(x-x_n^0)} & \text{if } x > x_n^0 \end{cases}. \quad (\text{F.6})$$

Substituting this into Eq. F.5, we immediately obtain Eq. 4.33.

Appendix G

Convergence of matrix-product-state simulations

Simulating time-delayed feedback with MPS, as described in section 4.2, requires discretizing the waveguide modes which are described as continuas of harmonic oscillators into waveguide bins (Eq. 4.39). This introduces a simulation parameter δt which controls the coarseness of this discretization. Moreover, application of a unitary impacting multiple bins in the MPS requires us to perform Schmidt decompositions on the state, and neglect Schmidt vectors with coefficients smaller than a specified tolerance. For the MPS-based simulation to be accurate, it is necessary to ensure that it has converged with respect to these two parameters. In this appendix, we present convergence studies with respect to these parameters to show that the choice of Δt ($= 0.05/\gamma$) and tolerance (0.01) assumed in section 4.2 indeed results in accurate simulations.

For the convergence study, we study the problem of an emitter decaying into the waveguide with a time-delayed feedback provided by the mirror and calculate the probability amplitude $|\varepsilon(t)|$ of the two-level system being in its excited state at time t calculated using $|\varepsilon(t)|^2 = \langle \sigma^\dagger \sigma \rangle$. We also assume that the mirror is perfect with phase $\varphi = 0$ (which, as can be seen from Fig. 4.4(a) results in the two-level system

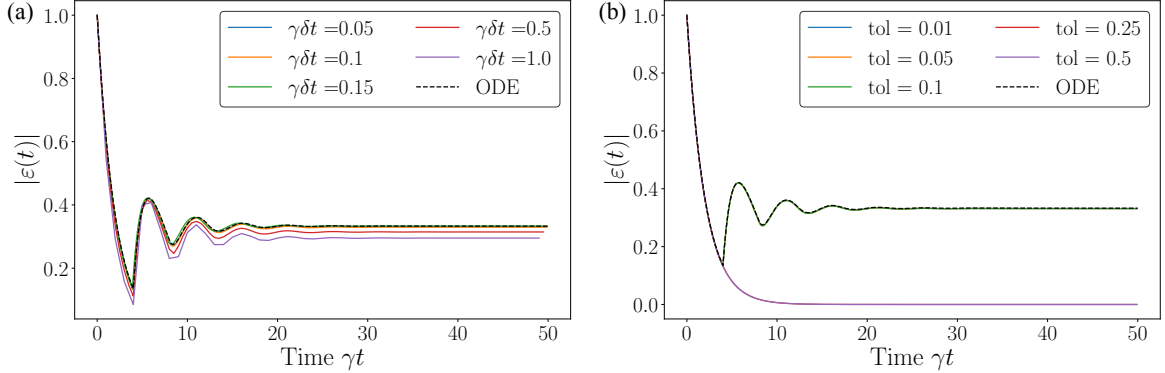


Figure G.1: Convergence studies on the MPS simulations for the time-delayed feedback system introduced in section 4.2. The undriven two-level system ($\Omega(t) = 0$) is initially in its excited state and is allowed to decay into the forward and backward propagating waveguide modes with an ideal mirror ($\theta = \pi/2, \varphi = 0$) providing feedback. $|\varepsilon(t)$ simulated using MPS update for (a) different discretization time-steps Δt and (b) different tolerances that govern the number of Schmidt vectors retained after every Schmidt decomposition on the MPS. The dotted black line shows $|\varepsilon(t)|$ obtained on solving the ODE (Eq. G.1) with a very small time-step ($\gamma\Delta t = 0.001$). $|\varepsilon(t)|$ is the probability amplitude of the two-level system being in the excited state computed using $|\varepsilon(t)|^2 = \langle \sigma^\dagger \sigma \rangle$. In the simulations shown in (a) the Schmidt tolerance is assumed to be 0.01 and in the simulations shown in (b) $\gamma\Delta t = 0.05$. It is also assumed that $\gamma_+ = \gamma_- = \gamma/2$, $\delta_e = \omega_e - \omega_0 = 0$, $\omega_0 t_d = \pi$ and $\gamma t_d = 2$.

not completely decaying into the ground state). In this case, the time-dependence of the complex amplitude of the excited state $\varepsilon(t)$ is given by the following ordinary differential equation (ODE) [144]:

$$\frac{d\varepsilon(t)}{dt} = -\frac{\gamma}{2}\varepsilon(t) - \frac{\gamma}{2}e^{i(2\omega_0 t_d + \varphi)}\varepsilon(t - 2t_d), \quad (\text{G.1})$$

where $\gamma = \gamma_+ + \gamma_-$ is the total decay rate of the two-level system into the forward and backward propagating waveguide modes and this equation is solved subject to the initial condition $\varepsilon(0) = 1$. $\varepsilon(t)$ obtained on solving this ODE thus provides a benchmark simulation that the MPS simulation can be compared against to gauge its convergence.

Fig. G.1 shows the results of the convergence studies. The dependence of $|\varepsilon(t)|$ obtained from the MPS update on the discretization time-step Δt is shown in Fig. G.1(a) — it can be seen that choosing $\Delta t < 0.15/\gamma$ is sufficient to ensure that the MPS simulation has converged and agrees with the ODE simulation. A similar study performed with respect to the tolerance used in the Schmidt decomposition is shown in Fig. G.1(b) from which it can be seen that a tolerance smaller than 0.1 is sufficient to ensure that the MPS simulation has converged and agrees with the ODE simulation.

Bibliography

- [1] Benioff, P. (1980) The computer as a physical system: A microscopic quantum mechanical Hamiltonian model of computers as represented by Turing machines. *J Stat Phys* **22**, 563–591.
- [2] Feynman, R. P. (1982) Simulating physics with computers. *Int J Theor Phys* **21**, 467–488.
- [3] Bennett, C. H & Brassard, G. (1984) Quantum cryptography: Public key distribution and coin tossing. *Theoretical Computer Science* **560**, 7–11.
- [4] Aharonov, D & Ben-Or, M. (2008) Fault-Tolerant Quantum Computation with Constant Error Rate. *SIAM J. Comput.* **38**, 1207–1282.
- [5] Gottesman, D. (2014) Fault-Tolerant quantum computation with constant overhead. *QIC* **14**, 1339–1371.
- [6] da Silva, M. P, Ryan-Anderson, C, Bello-Rivas, J. M, Chernoguzov, A, Dreiling, J. M, Foltz, C, Frachon, F, Gaebler, J. P, Gatterman, T. M, Grans-Samuelsson, L, Hayes, D, Hewitt, N, Johansen, J, Lucchetti, D, Mills, M, Moses, S. A, Neyenhuis, B, Paz, A, Pino, J, Siegfried, P, Strabley, J, Sundaram, A, Tom, D, Wernli, S. J, Zanner, M, Stutz, R. P, & Svore, K. M. (2024) Demonstration of logical qubits and repeated error correction with better-than-physical error rates.
- [7] Bluvstein, D, Evered, S. J, Geim, A. A, Li, S. H, Zhou, H, Manovitz, T, Ebadi, S, Cain, M, Kalinowski, M, Hangleiter, D, Bonilla Ataides, J. P, Maskara, N,

- Cong, I, Gao, X, Sales Rodriguez, P, Karolyshyn, T, Semeghini, G, Gullans, M. J, Greiner, M, Vuletić, V, & Lukin, M. D. (2024) Logical quantum processor based on reconfigurable atom arrays. *Nature* **626**, 58–65.
- [8] Bravyi, S, Cross, A. W, Gambetta, J. M, Maslov, D, Rall, P, & Yoder, T. J. (2024) High-threshold and low-overhead fault-tolerant quantum memory. *Nature* **627**, 778–782.
- [9] Arute, F, Arya, K, Babbush, R, Bacon, D, Bardin, J. C, Barends, R, Biswas, R, Boixo, S, Brandao, F. G. S. L, Buell, D. A, Burkett, B, Chen, Y, Chen, Z, Chiaro, B, Collins, R, Courtney, W, Dunsworth, A, Farhi, E, Foxen, B, Fowler, A, Gidney, C, Giustina, M, Graff, R, Guerin, K, Habegger, S, Harrigan, M. P, Hartmann, M. J, Ho, A, Hoffmann, M, Huang, T, Humble, T. S, Isakov, S. V, Jeffrey, E, Jiang, Z, Kafri, D, Kechedzhi, K, Kelly, J, Klimov, P. V, Knysh, S, Korotkov, A, Kostritsa, F, Landhuis, D, Lindmark, M, Lucero, E, Lyakh, D, Mandrà, S, McClean, J. R, McEwen, M, Megrant, A, Mi, X, Michielsen, K, Mohseni, M, Mutus, J, Naaman, O, Neeley, M, Neill, C, Niu, M. Y, Ostby, E, Petukhov, A, Platt, J. C, Quintana, C, Rieffel, E. G, Roushan, P, Rubin, N. C, Sank, D, Satzinger, K. J, Smelyanskiy, V, Sung, K. J, Trevithick, M. D, Vainsencher, A, Villalonga, B, White, T, Yao, Z. J, Yeh, P, Zalcman, A, Neven, H, & Martinis, J. M. (2019) Quantum supremacy using a programmable superconducting processor. *Nature* **574**, 505–510.
- [10] Kimble, H. J. (2008) The quantum internet. *Nature* **453**, 1023–1030.
- [11] Dory, C, Vercruyse, D, Yang, K. Y, Sapra, N. V, Rugar, A. E, Sun, S, Lukin, D. M, Piggott, A. Y, Zhang, J. L, Radulaski, M, Lagoudakis, K. G, Su, L, & Vučković, J. (2019) Inverse-designed diamond photonics. *Nature Communications* **10**, 3309.
- [12] Lukin, D. M, Dory, C, Guidry, M. A, Yang, K. Y, Mishra, S. D, Trivedi, R, Radulaski, M, Sun, S, Vercruyse, D, Ahn, G. H, & Vučković, J. (2020) 4H-silicon-carbide-on-insulator for integrated quantum and nonlinear photonics. *Nature Photonics* **14**, 330–334.

- [13] Zhu, X, Saito, S, Kemp, A, Kakuyanagi, K, Karimoto, S.-i, Nakano, H, Munro, W. J, Tokura, Y, Everitt, M. S, Nemoto, K, Kasu, M, Mizuochi, N, & Semba, K. (2011) Coherent coupling of a superconducting flux qubit to an electron spin ensemble in diamond. *Nature* **478**, 221–224.
- [14] Dold, G, Zollitsch, C. W, O’Sullivan, J, Welinski, S, Ferrier, A, Goldner, P, de Graaf, S, Lindström, T, & Morton, J. J. (2019) High-Cooperativity Coupling of a Rare-Earth Spin Ensemble to a Superconducting Resonator Using Yttrium Orthosilicate as a Substrate. *Physical Review Applied* **11**, 054082.
- [15] Trivedi, R, Radulaski, M, Fischer, K. A, Fan, S, & Vučković, J. (2019) Photon Blockade in Weakly Driven Cavity Quantum Electrodynamics Systems with Many Emitters. *Physical Review Letters* **122**, 243602.
- [16] González-Tudela, A, Paulisch, V, Chang, D. E, Kimble, H. J, & Cirac, J. I. (2015) Deterministic Generation of Arbitrary Photonic States Assisted by Dissipation. *Physical Review Letters* **115**, 163603.
- [17] Evans, R. E, Sipahigil, A, Sukachev, D. D, Zibrov, A. S, & Lukin, M. D. (2016) Narrow-Linewidth Homogeneous Optical Emitters in Diamond Nanostructures via Silicon Ion Implantation. *Physical Review Applied* **5**, 044010.
- [18] Dibos, A. M, Raha, M, Phenicie, C. M, & Thompson, J. D. (2018) Atomic Source of Single Photons in the Telecom Band. *Physical Review Letters* **120**, 243601.
- [19] Koch, C. P. (2016) Controlling open quantum systems: Tools, achievements, and limitations. *Journal of Physics: Condensed Matter* **28**, 213001.
- [20] Trivedi, R, Fischer, K, Xu, S, Fan, S, & Vuckovic, J. (2018) Few-photon scattering and emission from low-dimensional quantum systems. *Physical Review B* **98**, 144112.
- [21] Amico, L, Fazio, R, Osterloh, A, & Vedral, V. (2008) Entanglement in many-body systems. *Reviews of modern physics* **80**, 517.

- [22] Gharibian, S, Huang, Y, Landau, Z, Shin, S. W, et al. (2015) Quantum hamiltonian complexity. *Foundations and Trends® in Theoretical Computer Science* **10**, 159–282.
- [23] Verstraete, F, Wolf, M. M, & Ignacio Cirac, J. (2009) Quantum computation and quantum-state engineering driven by dissipation. *Nature Phys* **5**, 633–636.
- [24] Albash, T & Lidar, D. A. (2018) Adiabatic quantum computation. *Rev. Mod. Phys.* **90**, 015002.
- [25] Motta, M, Sun, C, Tan, A. T. K, O’Rourke, M. J, Ye, E, Minnich, A. J, Brandão, F. G. S. L, & Chan, G. K.-L. (2020) Determining eigenstates and thermal states on a quantum computer using quantum imaginary time evolution. *Nat. Phys.* **16**, 205–210.
- [26] Cerezo, M, Arrasmith, A, Babbush, R, Benjamin, S. C, Endo, S, Fujii, K, McClean, J. R, Mitarai, K, Yuan, X, Cincio, L, & Coles, P. J. (2021) Variational quantum algorithms. *Nat Rev Phys* **3**, 625–644.
- [27] Farhi, E, Goldstone, J, & Gutmann, S. (2014) A Quantum Approximate Optimization Algorithm.
- [28] Wecker, D, Hastings, M. B, & Troyer, M. (2015) Progress towards practical quantum variational algorithms. *Phys. Rev. A* **92**, 042303.
- [29] Bharti, K, Cervera-Lierta, A, Kyaw, T. H, Haug, T, Alperin-Lea, S, Anand, A, Degroote, M, Heimonen, H, Kottmann, J. S, Menke, T, Mok, W.-K, Sim, S, Kwek, L.-C, & Aspuru-Guzik, A. (2022) Noisy intermediate-scale quantum algorithms. *Rev. Mod. Phys.* **94**, 015004.
- [30] Goemans, M. X & Williamson, D. P. (1995) Improved approximation algorithms for maximum cut and satisfiability problems using semidefinite programming. *J. ACM* **42**, 1115–1145.
- [31] Anjos, M. F et al. (2004) On semidefinite programming relaxations for the satisfiability problem. *Math. Methods Oper. Res.* **60**, 349–367.

- [32] Oliveira, R & Terhal, B. M. (2005) The complexity of quantum spin systems on a two-dimensional square lattice. *arXiv preprint quant-ph/0504050*.
- [33] Aharonov, D, Ben-Or, M, Impagliazzo, R, & Nisan, N. (1996) Limitations of Noisy Reversible Computation.
- [34] Stilck França, D & García-Patrón, R. (2021) Limitations of optimization algorithms on noisy quantum devices. *Nat. Phys.* **17**, 1221–1227.
- [35] De Palma, G, Marvian, M, Rouzé, C, & França, D. S. (2023) Limitations of variational quantum algorithms: a quantum optimal transport approach. *PRX Quantum* **4**, 010309.
- [36] Blais, A, Gambetta, J, Wallraff, A, Schuster, D. I, Girvin, S. M, Devoret, M. H, & Schoelkopf, R. J. (2007) Quantum-information processing with circuit quantum electrodynamics. *Phys. Rev. A* **75**, 032329.
- [37] Imamoglu, A, Awschalom, D. D, Burkard, G, DiVincenzo, D. P, Loss, D, Sherwin, M, & Small, A. (1999) Quantum Information Processing Using Quantum Dot Spins and Cavity QED. *Phys. Rev. Lett.* **83**, 4204–4207.
- [38] Duan, L.-M, Lukin, M. D, Cirac, J. I, & Zoller, P. (2001) Long-distance quantum communication with atomic ensembles and linear optics. *Nature* **414**, 413–418.
- [39] Pichler, H & Zoller, P. (2016) Photonic Circuits with Time Delays and Quantum Feedback. *Phys. Rev. Lett.* **116**, 093601.
- [40] Grimsmo, A. L. (2015) Time-Delayed Quantum Feedback Control. *Phys. Rev. Lett.* **115**, 060402.
- [41] Schollwöck, U. (2011) The density-matrix renormalization group in the age of matrix product states. *Annals of physics* **326**, 96–192.
- [42] Orus, R. (2014) A Practical Introduction to Tensor Networks: Matrix Product States and Projected Entangled Pair States. *Annals of Physics* **349**, 117–158.

- [43] Magnard, P, Storz, S, Kurpiers, P, Schär, J, Marxer, F, Lütolf, J, Besse, J.-C, Gabureac, M, Reuer, K, Akin, A, Royer, B, Blais, A, & Wallraff, A. (2020) Microwave Quantum Link between Superconducting Circuits Housed in Spatially Separated Cryogenic Systems. *arXiv:2008.01642 [quant-ph]*.
- [44] Lambert, N. J, Rueda, A, Sedlmeir, F, & Schwefel, H. G. L. (2020) Coherent Conversion Between Microwave and Optical Photons—An Overview of Physical Implementations. *Advanced Quantum Technologies* **3**, 1900077.
- [45] Lauk, N, Sinclair, N, Barzanjeh, S, Covey, J. P, Saffman, M, Spiropulu, M, & Simon, C. (2020) Perspectives on quantum transduction. *Quantum Science and Technology* **5**, 020501.
- [46] McKenna, T. P, Witmer, J. D, Patel, R. N, Jiang, W, Laer, R. V, Arrangoiz-Arriola, P, Wollack, E. A, Herrmann, J. F, & Safavi-Naeini, A. H. (2020) Cryogenic microwave-to-optical conversion using a triply resonant lithium-niobate-on-sapphire transducer. *Optica, OPTICA* **7**, 1737–1745.
- [47] Holzgrafe, J, Sinclair, N, Zhu, D, Shams-Ansari, A, Colangelo, M, Hu, Y, Zhang, M, Berggren, K. K, & Lončar, M. (2020) Cavity electro-optics in thin-film lithium niobate for efficient microwave-to-optical transduction. *arXiv:2005.00939 [physics, physics:quant-ph]*.
- [48] Soltani, M, Zhang, M, Ryan, C, Ribeill, G. J, Wang, C, & Loncar, M. (2017) Efficient quantum microwave-to-optical conversion using electro-optic nanophotonic coupled resonators. *Physical Review A* **96**, 043808.
- [49] Tsang, M. (2010) Cavity quantum electro-optics. *Physical Review A* **81**, 063837.
- [50] Rueda, A, Hease, W, Barzanjeh, S, & Fink, J. M. (2019) Electro-optic entanglement source for microwave to telecom quantum state transfer. *npj Quantum Information* **5**, 1–11.
- [51] Rueda, A, Sedlmeir, F, Collodo, M. C, Vogl, U, Stiller, B, Schunk, G, Strekalov, D. V, Marquardt, C, Fink, J. M, Painter, O, Leuchs, G, & Schwefel, H. G. L.

- (2016) Efficient microwave to optical photon conversion: An electro-optical realization. *Optica* **3**, 597–604.
- [52] Hisatomi, R, Osada, A, Tabuchi, Y, Ishikawa, T, Noguchi, A, Yamazaki, R, Usami, K, & Nakamura, Y. (2016) Bidirectional conversion between microwave and light via ferromagnetic magnons. *Physical Review B* **93**, 174427.
- [53] Everts, J. R, Berrington, M. C, Ahlefeldt, R. L, & Longdell, J. J. (2019) Microwave to optical photon conversion via fully concentrated rare-earth-ion crystals. *Physical Review A* **99**, 063830.
- [54] Everts, J, King, G. G. G, Lambert, N, Kocsis, S, Rogge, S, & Longdell, J. J. (2020) Ultrastrong coupling between a microwave resonator and antiferromagnetic resonances of rare earth ion spins. *Physical Review B* **101**, 214414. Comment: 5 pages, 5 figures.
- [55] Zhong, C, Wang, Z, Zou, C, Zhang, M, Han, X, Fu, W, Xu, M, Shankar, S, Devoret, M. H, Tang, H. X, & Jiang, L. (2020) Proposal for Heralded Generation and Detection of Entangled Microwave–Optical-Photon Pairs. *Physical Review Letters* **124**, 010511.
- [56] Wu, M, Zeuthen, E, Balram, K. C, & Srinivasan, K. (2020) Microwave-to-Optical Transduction Using a Mechanical Supermode for Coupling Piezoelectric and Optomechanical Resonators. *Physical Review Applied* **13**, 014027.
- [57] Lau, H.-K & Clerk, A. A. (2020) Ground state cooling and high-fidelity quantum transduction via parametrically-driven bad-cavity optomechanics. *Physical Review Letters* **124**, 103602. Comment: Close to accepted version.
- [58] Jiang, W, Sarabalis, C. J, Dahmani, Y. D, Patel, R. N, Mayor, F. M, McKenna, T. P, Van Laer, R, & Safavi-Naeini, A. H. (2020) Efficient bidirectional piezo-optomechanical transduction between microwave and optical frequency. *Nat Commun* **11**, 1166.

- [59] Forsch, M, Stockill, R, Wallucks, A, Marinković, I, Gärtner, C, Norte, R. A, van Otten, F, Fiore, A, Srinivasan, K, & Gröblacher, S. (2020) Microwave-to-optics conversion using a mechanical oscillator in its quantum ground state. *Nature Physics* **16**, 69–74.
- [60] Arnold, G, Wulf, M, Barzanjeh, S, Redchenko, E. S, Rueda, A, Hease, W. J, Hassani, F, & Fink, J. M. (2020) Converting microwave and telecom photons with a silicon photonic nanomechanical interface. *Nature Communications* **11**, 4460.
- [61] Bağcı, T, Simonsen, A, Schmid, S, Villanueva, L. G, Zeuthen, E, Appel, J, Taylor, J. M, Sørensen, A, Usami, K, Schliesser, A, & Polzik, E. S. (2014) Optical detection of radio waves through a nanomechanical transducer. *Nature* **507**, 81–85.
- [62] Andrews, R. W, Peterson, R. W, Purdy, T. P, Cicak, K, Simmonds, R. W, Regal, C. A, & Lehnert, K. W. (2014) Bidirectional and efficient conversion between microwave and optical light. *Nature Physics* **10**, 321–326.
- [63] Wang, Y.-D & Clerk, A. A. (2012) Using Interference for High Fidelity Quantum State Transfer in Optomechanics. *Physical Review Letters* **108**, 153603.
- [64] Tian, L. (2012) Adiabatic State Conversion and Pulse Transmission in Optomechanical Systems. *Physical Review Letters* **108**, 153604.
- [65] Hill, J. T, Safavi-Naeini, A. H, Chan, J, & Painter, O. (2012) Coherent optical wavelength conversion via cavity optomechanics. *Nature Communications* **3**, 1196.
- [66] Barzanjeh, S, Abdi, M, Milburn, G. J, Tombesi, P, & Vitali, D. (2012) Reversible Optical-to-Microwave Quantum Interface. *Physical Review Letters* **109**, 130503.
- [67] Safavi-Naeini, A. H & Painter, O. (2011) Proposal for an optomechanical traveling wave phonon–photon translator. *New Journal of Physics* **13**, 013017.

- [68] Tian, L & Wang, H. (2010) Optical wavelength conversion of quantum states with optomechanics. *Physical Review A* **82**, 053806.
- [69] Stannigel, K, Rabl, P, Sørensen, A. S, Zoller, P, & Lukin, M. D. (2010) Optomechanical Transducers for Long-Distance Quantum Communication. *Physical Review Letters* **105**, 220501.
- [70] Bartholomew, J. G, Rochman, J, Xie, T, Kindem, J. M, Ruskuc, A, Craiciu, I, Lei, M, & Faraon, A. (2020) On-chip coherent microwave-to-optical transduction mediated by ytterbium in YVO₄. *Nature Communications* **11**, 3266.
- [71] Barnett, P. S & Longdell, J. J. (2020) Theory of Microwave-Optical Conversion Using Rare-Earth Ion Dopants. *arXiv:2008.10834 [quant-ph]*. Comment: 10 pages, 7 figures.
- [72] Welinski, S, Woodburn, P. J. T, Lauk, N, Cone, R. L, Simon, C, Goldner, P, & Thiel, C. W. (2019) Electron Spin Coherence in Optically Excited States of Rare-Earth Ions for Microwave to Optical Quantum Transducers. *Physical Review Letters* **122**, 247401.
- [73] Vogt, T, Gross, C, Han, J, Pal, S. B, Lam, M, Kiffner, M, & Li, W. (2019) Efficient microwave-to-optical conversion using Rydberg atoms. *Physical Review A* **99**, 023832.
- [74] Petrosyan, D, Mølmer, K, Fortágh, J, & Saffman, M. (2019) Microwave to optical conversion with atoms on a superconducting chip. *New Journal of Physics* **21**, 073033.
- [75] Fernandez-Gonzalvo, X, Horvath, S. P, Chen, Y.-H, & Longdell, J. J. (2019) Cavity-enhanced Raman heterodyne spectroscopy in Er³⁺: Y₂SiO₅ for microwave to optical signal conversion. *Physical Review A* **100**, 033807.
- [76] Covey, J. P, Sipahigil, A, & Saffman, M. (2019) Microwave-to-optical conversion via four-wave mixing in a cold ytterbium ensemble. *Physical Review A* **100**, 012307.

- [77] Han, J, Vogt, T, Gross, C, Jaksch, D, Kiffner, M, & Li, W. (2018) Coherent Microwave-to-Optical Conversion via Six-Wave Mixing in Rydberg Atoms. *Physical Review Letters* **120**, 093201.
- [78] Gard, B. T, Jacobs, K, McDermott, R, & Saffman, M. (2017) Microwave-to-optical frequency conversion using a cesium atom coupled to a superconducting resonator. *Physical Review A* **96**, 013833.
- [79] Kiffner, M, Feizpour, A, Kaczmarek, K. T, Jaksch, D, & Nunn, J. (2016) Two-way interconversion of millimeter-wave and optical fields in Rydberg gases. *New Journal of Physics* **18**, 093030.
- [80] Fernandez-Gonzalvo, X, Chen, Y.-H, Yin, C, Rogge, S, & Longdell, J. J. (2015) Coherent frequency up-conversion of microwaves to the optical telecommunications band in an Er:YSO crystal. *Physical Review A* **92**, 062313.
- [81] Williamson, L. A, Chen, Y.-H, & Longdell, J. J. (2014) Magneto-Optic Modulator with Unit Quantum Efficiency. *Physical Review Letters* **113**, 203601.
- [82] O'Brien, C, Lauk, N, Blum, S, Morigi, G, & Fleischhauer, M. (2014) Interfacing Superconducting Qubits and Telecom Photons via a Rare-Earth-Doped Crystal. *Physical Review Letters* **113**, 063603.
- [83] Hafezi, M, Kim, Z, Rolston, S. L, Orozco, L. A, Lev, B. L, & Taylor, J. M. (2012) Atomic interface between microwave and optical photons. *Physical Review A* **85**, 020302.
- [84] Verdú, J, Zoubi, H, Koller, C, Majer, J, Ritsch, H, & Schmiedmayer, J. (2009) Strong Magnetic Coupling of an Ultracold Gas to a Superconducting Waveguide Cavity. *Physical Review Letters* **103**, 043603.
- [85] Imamoğlu, A. (2009) Cavity QED Based on Collective Magnetic Dipole Coupling: Spin Ensembles as Hybrid Two-Level Systems. *Physical Review Letters* **102**, 083602.

- [86] Wan, N. H, Lu, T.-J, Chen, K. C, Walsh, M. P, Trusheim, M. E, De Santis, L, Bersin, E. A, Harris, I. B, Mouradian, S. L, Christen, I. R, Bielejec, E. S, & Englund, D. (2020) Large-scale integration of artificial atoms in hybrid photonic circuits. *Nature* **583**, 226–231.
- [87] Dicke, R. H. (1954) Coherence in Spontaneous Radiation Processes. *Physical Review* **93**, 99–110.
- [88] Gross, M & Haroche, S. (1982) Superradiance: An essay on the theory of collective spontaneous emission. *Physics Reports* **93**, 301–396.
- [89] Paulisch, V, Perarnau-Llobet, M, González-Tudela, A, & Cirac, J. I. (2019) Quantum metrology with one-dimensional superradiant photonic states. *Physical Review A* **99**, 043807.
- [90] Zhong, T, Kindem, J. M, Bartholomew, J. G, Rochman, J, Craiciu, I, Verma, V, Nam, S. W, Marsili, F, Shaw, M. D, Beyer, A. D, & Faraon, A. (2018) Optically Addressing Single Rare-Earth Ions in a Nanophotonic Cavity. *Physical Review Letters* **121**, 183603.
- [91] Gorshkov, A. V, Calarco, T, Lukin, M. D, & Sørensen, A. S. (2008) Photon storage in Λ -type optically dense atomic media. IV. Optimal control using gradient ascent. *Physical Review A* **77**, 043806.
- [92] Schmidt, W. H. (2006) *Numerical Methods for Optimal Control Problems with ODE or Integral Equations*, Lecture Notes in Computer Science eds. Lirkov, I, Margenov, S, & Waśniewski, J. (Springer, Berlin, Heidelberg), pp. 255–262.
- [93] Swillam, M. A, Bakr, M. H, & Li, X. (2007) Accurate sensitivity analysis of photonic devices that exploit the finite-difference time-domain central adjoint variable method. *Applied Optics* **46**, 1492–1499.
- [94] Trivedi, R, White, A, Fan, S, & Vučković, J. (2020) Analytic and geometric properties of scattering from periodically modulated quantum-optical systems. *Physical Review A* **102**, 033707.

- [95] Brecht, B, Reddy, D. V, Silberhorn, C, & Raymer, M. G. (2015) Photon Temporal Modes: A Complete Framework for Quantum Information Science. *Physical Review X* **5**, 041017.
- [96] Courant, R & Hilbert, D. (1989) in *Methods of Mathematical Physics*. (John Wiley & Sons, Ltd), pp. 48–111.
- [97] Boyd, S & Vandenberghe, L. (2004) *Convex Optimization*. (Cambridge University Press, Cambridge).
- [98] Trivedi, R, Angeris, G, Su, L, Boyd, S, Fan, S, & Vučković, J. (2020) Bounds for Scattering from Absorptionless Electromagnetic Structures. *Physical Review Applied* **14**, 014025.
- [99] Ge, Y, Tura, J, & Cirac, J. I. (2019) Faster ground state preparation and high-precision ground energy estimation with fewer qubits. *Journal of Mathematical Physics* **60**, 022202.
- [100] Ge, Y, Molnár, A, & Cirac, J. I. (2016) Rapid Adiabatic Preparation of Injective Projected Entangled Pair States and Gibbs States. *Phys. Rev. Lett.* **116**, 080503.
- [101] Zhou, Y, Stoudenmire, E. M, & Waintal, X. (2020) What Limits the Simulation of Quantum Computers? *Phys. Rev. X* **10**, 041038.
- [102] Pan, F & Zhang, P. (2022) Simulation of Quantum Circuits Using the Big-Batch Tensor Network Method. *Phys. Rev. Lett.* **128**, 030501.
- [103] Rakovszky, T, von Keyserlingk, C. W, & Pollmann, F. (2022) Dissipation-assisted operator evolution method for capturing hydrodynamic transport. *Phys. Rev. B* **105**, 075131.
- [104] Aharonov, D, Gao, X, Landau, Z, Liu, Y, & Vazirani, U. (2023) *A Polynomial-Time Classical Algorithm for Noisy Random Circuit Sampling*, STOC 2023. (Association for Computing Machinery, New York, NY, USA), pp. 945–957.

- [105] Trivedi, R & Cirac, J. I. (2022) Transitions in Computational Complexity of Continuous-Time Local Open Quantum Dynamics. *Phys. Rev. Lett.* **129**, 260405.
- [106] González-García, G, Trivedi, R, & Cirac, J. I. (2022) Error Propagation in NISQ Devices for Solving Classical Optimization Problems. *PRX Quantum* **3**, 040326.
- [107] Deshpande, A, Niroula, P, Shtanko, O, Gorshkov, A. V, Fefferman, B, & Gul-lans, M. J. (2022) Tight Bounds on the Convergence of Noisy Random Circuits to the Uniform Distribution. *PRX Quantum* **3**, 040329.
- [108] Müller-Lennert, M, Dupuis, F, Szehr, O, Fehr, S, & Tomamichel, M. (2013) On quantum rényi entropies: A new generalization and some properties. *Journal of Mathematical Physics* **54**, 122203.
- [109] Boyd, S & Vandenberghe, L. (2004) *Convex Optimization* (Cambridge University Press).
- [110] Trivedi, R, Angeris, G, Su, L, Boyd, S, Fan, S, & Vučković, J. (2020) Bounds for Scattering from Absorptionless Electromagnetic Structures. *Phys. Rev. Appl.* **14**, 014025.
- [111] Slater, M. (2014) in *Traces and Emergence of Nonlinear Programming*, eds. Giorgi, G & Kjeldsen, T. H. (Springer Basel, Basel), pp. 293–306.
- [112] Vidal, G. (2004) Efficient Simulation of One-Dimensional Quantum Many-Body Systems. *Phys. Rev. Lett.* **93**, 040502.
- [113] Verstraete, F, García-Ripoll, J. J, & Cirac, J. I. (2004) Matrix Product Density Operators: Simulation of Finite-Temperature and Dissipative Systems. *Phys. Rev. Lett.* **93**, 207204.
- [114] Daley, A. J, Kollath, C, Schollwöck, U, & Vidal, G. (2004) Time-dependent density-matrix renormalization-group using adaptive effective Hilbert spaces. *J. Stat. Mech.* **2004**, P04005.

- [115] White, S. R & Feiguin, A. E. (2004) Real-Time Evolution Using the Density Matrix Renormalization Group. *Phys. Rev. Lett.* **93**, 076401.
- [116] Vidal, G. (2003) Efficient Classical Simulation of Slightly Entangled Quantum Computations. *Phys. Rev. Lett.* **91**, 147902.
- [117] (2024). Given a finite-dimensional Hilbert space \mathcal{H} , we use $\mathcal{D}_1(\mathcal{H})$ to denote the set of all density matrices on \mathcal{H} , and $\mathcal{M}(\mathcal{H})$ to denote the set of Hermitian linear operators on \mathcal{H} . We use the computer-science big-O notation for function asymptotics. In particular, given two functions $f, g : [0, \infty) \rightarrow [0, \infty)$, $f = O(g)$ if, for some $c > 0$, $f(x) \leq cg(x)$ as $x \rightarrow \infty$ and $f = \Omega(g)$ if, for some $c > 0$, $f(x) \geq cg(x)$ as $x \rightarrow \infty$.
- [118] Gottesman, D. (1998) The Heisenberg Representation of Quantum Computers.
- [119] Aaronson, S & Gottesman, D. (2004) Improved Simulation of Stabilizer Circuits. *Phys. Rev. A* **70**, 052328.
- [120] Quek, Y, França, D. S, Khatri, S, Meyer, J. J, & Eisert, J. (2023) Exponentially tighter bounds on limitations of quantum error mitigation.
- [121] Kuwahara, T, Kato, K, & Brandão, F. G. S. L. (2020) Clustering of Conditional Mutual Information for Quantum Gibbs States above a Threshold Temperature. *Phys. Rev. Lett.* **124**, 220601.
- [122] Pan, F, Zhou, P, Li, S, & Zhang, P. (2020) Contracting Arbitrary Tensor Networks: General Approximate Algorithm and Applications in Graphical Models and Quantum Circuit Simulations. *Phys. Rev. Lett.* **125**, 060503.
- [123] Markov, I. L & Shi, Y. (2008) Simulating Quantum Computation by Contracting Tensor Networks. *SIAM J. Comput.* **38**, 963–981.
- [124] Lubasch, M, Cirac, J. I, & Bañuls, M.-C. (2014) Algorithms for finite projected entangled pair states. *Phys. Rev. B* **90**, 064425.

- [125] Fan, S, Kocabaş, Ş. E, & Shen, J.-T. (2010) Input-output formalism for few-photon transport in one-dimensional nanophotonic waveguides coupled to a qubit. *Phys. Rev. A* **82**, 063821.
- [126] Xu, S & Fan, S. (2015) Input-output formalism for few-photon transport: A systematic treatment beyond two photons. *Phys. Rev. A* **91**, 043845.
- [127] Trivedi, R, Fischer, K, Xu, S, Fan, S, & Vuckovic, J. (2018) Few-photon scattering and emission from low-dimensional quantum systems. *Phys. Rev. B* **98**, 144112.
- [128] Dalton, B. J, Barnett, S. M, & Knight, P. L. (1999) Quasi mode theory of the beam splitter—a quantum scattering theory approach. *Journal of Modern Optics* **46**, 1559–1577.
- [129] Schollwöck, U. (2011) The density-matrix renormalization group in the age of matrix product states. *Annals of Physics* **326**, 96–192.
- [130] Pichler, H, Choi, S, Zoller, P, & Lukin, M. D. (2017) Universal photonic quantum computation via time-delayed feedback. *Proceedings of the National Academy of Sciences* **114**, 11362–11367.
- [131] Lubasch, M, Valido, A. A, Renema, J. J, Kolthammer, W. S, Jaksch, D, Kim, M. S, Walmsley, I, & García-Patrón, R. (2018) Tensor network states in time-bin quantum optics. *Phys. Rev. A* **97**, 062304.
- [132] Dhand, I, Engelkemeier, M, Sansoni, L, Barkhofen, S, Silberhorn, C, & Plenio, M. B. (2018) Proposal for Quantum Simulation via All-Optically-Generated Tensor Network States. *Phys. Rev. Lett.* **120**, 130501.
- [133] Calajó, G, Fang, Y.-L. L, Baranger, H. U, & Ciccarello, F. (2019) Exciting a Bound State in the Continuum through Multiphoton Scattering Plus Delayed Quantum Feedback. *Phys. Rev. Lett.* **122**, 073601.
- [134] Taylor, J. R. (2012) *Scattering Theory: The Quantum Theory of Nonrelativistic Collisions*. (Courier Corporation).

- [135] Kok, P, Munro, W. J, Nemoto, K, Ralph, T. C, Dowling, J. P, & Milburn, G. J. (2007) Linear optical quantum computing with photonic qubits. *Rev. Mod. Phys.* **79**, 135–174.
- [136] Shi, Y.-Y, Duan, L.-M, & Vidal, G. (2006) Classical simulation of quantum many-body systems with a tree tensor network. *Phys. Rev. A* **74**, 022320.
- [137] Vidal, G. (2003) Efficient Classical Simulation of Slightly Entangled Quantum Computations. *Phys. Rev. Lett.* **91**, 147902.
- [138] Johansson, J. R, Nathon, P. D, & Nori, F. (2013) QuTiP 2: A Python framework for the dynamics of open quantum systems. *Computer Physics Communications* **184**, 1234–1240.
- [139] Debnath, K, Zhang, Y, & Mølmer, K. (2019) Collective dynamics of inhomogeneously broadened emitters coupled to an optical cavity with narrow linewidth. *Physical Review A* **100**, 053821.
- [140] Lukin, D. M, White, A. D, Trivedi, R, Guidry, M. A, Morioka, N, Babin, C, Soykal, Ö. O, Ul-Hassan, J, Son, N. T, Ohshima, T, Vasireddy, P. K, Nasr, M. H, Sun, S, MacLean, J.-P. W, Dory, C, Nanni, E. A, Wrachtrup, J, Kaiser, F, & Vučković, J. (2020) Spectrally reconfigurable quantum emitters enabled by optimized fast modulation. *npj Quantum Information* **6**, 1–9.
- [141] Surace, J & Tagliacozzo, L. (2022) Fermionic Gaussian states: An introduction to numerical approaches. *SciPost Phys. Lect. Notes* p. 54.
- [142] Schuch, N & Bauer, B. (2019) Matrix product state algorithms for Gaussian fermionic states. *Phys. Rev. B* **100**, 245121.
- [143] Dankert, C, Cleve, R, Emerson, J, & Livine, E. (2009) Exact and approximate unitary 2-designs and their application to fidelity estimation. *Phys. Rev. A* **80**, 012304.
- [144] Tufarelli, T, Ciccarello, F, & Kim, M. S. (2013) Dynamics of spontaneous emission in a single-end photonic waveguide. *Phys. Rev. A* **87**, 013820.